Carrier Diffusion in Organic-inorganic Perovskites

A thesis submitted for the degree
Doctor of Philosophy
By

Chunhua Zhou

Centre for Translational Atom-Materials
Faculty of Science, Engineering and Technology
Swinburne University of Technology
Melbourne, Australia

Supervisor Prof. Baohua Jia

Co-Supervisor Dr. Xiaoming Wen, Dr. Weijian Chen

2021-02

Declaration

I, Chunhua Zhou, declare that this thesis entitled:

"Carrier Diffusion in Organic-inorganic Perovskites"

is my own work and has not been submitted previously, in whole or in part, in respect of any other academic award.

Chunhua Zhou

Chunhua Zhou

Centre for Translational Atomaterials

Faculty of Science, Engineering and Technology

Swinburne University of Technology

Melbourne, Australia

February 2021

Abstract

Hybrid organic–inorganic halide perovskites have obtained world-wide attention due to their high performance for photovoltaic and optoelectronic applications. The excellent performance of perovskite devices is determined by their outstanding photoelectric properties. However, many unresolved questions remain on the carrier diffusion in special structured perovskites, including determining in-plane carrier diffusion in two-dimensional (2D) perovskite nanoplatelets, the details of carrier diffusion in gradient bandgap perovskites and the on-chip application of such perovskites.

Here, the fundamental carrier dynamics of perovskites is deeply investigated, and the major achievements can be summarized as follows: (1) A novel method is developed for determining in-plane diffusion length in 2D layered perovskites. The diffusion length was obtained for an exfoliated nanoplatelet (NP) from a 2D layered perovskite single crystal. This method can be applied to other 2D and three-dimensional (3D) thin flakes, which is useful for the development and optimization of semiconductor materials and their devices. (2) The carrier diffusion behaviors and halide segregation phenomenon are investigated in gradient bandgap perovskites. In such structures, photogenerated carriers can effectively transport and emit in the low bandgap region, while irreversible and stable phases are formed by the halide segregation. The investigation will greatly benefit their future optoelectronic applications. (3) Using femtosecond laser direct writing technique, the luminescence color of such gradient bandgap perovskites is spatially modulated. This straightforward technique allows the possibility to develop a range of optoelectronic devices, such as micro-encryption, multicolor display and light-emitting devices.

Acknowledgement

My Ph.D. journey started in February 2017 at Swinburne University of Technology. It has been three and a half years till now. I am grateful for the following kind persons, without their help, the completion of this thesis would not have been possible.

My deep gratitude goes first to my Principal supervisor, Dr. Xiaoming Wen, who expertly guided me through my whole Ph.D. study. It is a great privilege and honor to do research under his guidance. His unwavering enthusiasm for physics kept me constantly engaged with my research.

I would like to express my sincere gratitude to my co-supervisor, Prof. Baohua Jia, for letting me fulfill my dreams of being a student here and providing invaluable guidance throughout my study and research. Her dynamism, vision and motivation have deeply inspired me.

My appreciation also extends to my co-supervisors, Dr. Weijian Chen and Dr. Han Lin, for their directive consultations and technical support. My sincere thank also goes to Dr. Zhixing Gan and Dr. Fei Zheng, who have shared the effort and knowledge to make my research a reality.

My special thanks go to our collaborators Prof. Qiaoliang Bao, Dr. Qingdong Ou from Monash University and Prof. Shuang Yang from Shandong University, who provide me the high-quality perovskite samples continually. They also provided valuable advices and relevant data of samples.

I would like to thank my classmates and colleagues. Many thanks to the fellow classmates, for the works we have done together and all the fun we have had in the last few years. Many thanks to the colleagues and technicians, who are always there for help. Many thanks to them, too many to name them all, they made my Ph.D. life so colorful.

I also thank the China Scholarship Council (CSC) for their financial support during my PhD study.

Above ground, I am extremely grateful to my family, whose value to me only grows with age. Finally, I would like to give the most special thanks to my husband, Zhiyu Wang, who is my best friend, closest advisor, and the love of my life.

Chunhua Zhou
Melbourne, Australia
12th, September 2020

Table of Contents

Glossary of Terms

PCE	power conversion efficiency
LED	light-emitting diode
PD	photodetector
2D	two-dimensional
3D	three-dimensional
NP	nanoplatelet
EDS	energy dispersive spectroscopy
PL	photoluminescence
fs-DLW	femtosecond direct laser writing
MA	methylammonium, CH_3NH_3
FA	formamidinium, $HC(NH_2)_2$
PEA	phenethylammonium
BA	butylammonium, $CH_3(CH_2)_3NH_3$
PLQY	photoluminescence quantum yield
SEM	scanning electron microscopy
CB	conduction band

SRH	Shockley−Read−Hall
TRPL	time-resolved photoluminescence
D	diffusion coefficient
L	diffusion length
TA	transient absorption
TRTS	time-resolved terahertz absorption spectroscopy
CCD	charged-coupled device
TCSPC	time-correlated single photon counting
TA	transient absorption
SPAD	single photon avalanche diode
FLIM	fluorescence lifetime imaging
RPPs	Ruddlesden-Popper perovskites
MQW	multi-quantum-well
TEM	transmission electron microscopic
ERV	edge recombination velocity
CVD	chemical vapor deposition
LO	longitudinal optical
fs	femtosecond
CIE	Commission Internationale de L'Eclairage

List of Figures

List of Tables

Chapter 1

Introduction

1.1 Background

Perovskite was composed of $CaTiO_3$ in the history of minerals. It was first discovered by a Prussian mineralogist in 1839 and named after the Russian mineralogist Count Lev A. Perovskit.[1] Pure perovskite is clear, with a refractive index of approximately 2.38. The crystal structure is orthorhombic, so the name perovskite was given to a family of compounds with a general formula ABX_3. Later, perovskite compounds are more commonly known as metal oxides, and found use in various ferroelectric, piezoelectric, dielectric, and pyroelectric applications.

The first perovskite solar cell was reported in 2009, with power conversion efficiency (PCE) of 3.8%.[2] Since then, numerous investigations have been conducted in this field. The PCE of perovskite solar cells increased to 25.2% in a short period of time, which is comparable to commercial thin-film solar cells such as silicon and telluride. (https://www.nrel.gov/pv/assets/pdfs/best-research-cell-efficiencies.20200406.pdf) Moreover, the solution-based synthesis process of perovskites is simple and of low-cost. Thus, perovskite solar cell is regarded as the most promising photovoltaic technology for the next generation of solar cells.

In addition, organic-inorganic perovskite materials have found position in photonic and optoelectronic applications such as light-emitting diodes (LEDs), X-ray detectors, lasers, photodetectors (PDs) and so on. For example, green LEDs based on perovskites reached a current efficiency of 62.4 cd A^{-1} and external quantum efficiency of 14.36%, which were comparable to the state-of-the-art organic LEDs.[3]

A clear understanding of the fundamental photo-physics underlying perovskite materials is essential for the further expansion of their applications and improvement of their device performance. Both theoretical and experimental investigations have been carried out in recent years, and some rare properties of perovskite materials are well accepted to contribute to the superior performance and high efficiency of perovskite applications. The important factors are the following: (1) a high optical absorption coefficient (10^5 cm^{-1}) that allows the use of a thin film, (2) a long carrier diffusion length and suppressed recombinations (defect tolerance), and (3) a well-balanced charge carrier transport. In photovoltaic applications, the defect-tolerant nature of halide perovskites is especially important, as it leads to the generation of high voltage.[4]

However, the basic understanding of carrier transport characteristics is still limited, as complex photophysical properties are shown in various organic-inorganic perovskite materials. For example, two-dimensional (2D) perovskites are quantum-confined materials, in which carriers are located and diffused within ordered structures that are separated by long cationic lattices. In comparison to their three-dimensional (3D) counterparts, the carrier diffusion length and coefficient are drastically reduced in the direction of depth, while the in-plane direction diffusion of excitons are not limited.[5] Careful consideration and optimization of these parameters are always needed, as they are critical for the applications of 2D perovskites. A few methods have been reported for determination of the diffusion length to date,[6-7] such as space-charge limited current[8] and PL quenching[9]. However, these techniques need a large-scale or a high PL-efficiency of perovskite samples. The diffusion length detection of thin 2D perovskite flakes with low luminescence is still a challenge.

Perovskite solar cells with efficient energy funneling can achieve higher PCE and improved stability.[10] Photogenerated carriers can transport from high-bandgap region to low-bandgap region effectively in these perovskites, which can achieve long carrier diffusion length and high PL efficiency.[11] With the ability of continuous tuning of the bandgap, the mixed organic–inorganic hybrid lead halide perovskites are of high potential for bandgap engineering. For example, halide compositional gradient

$CH_3NH_3PbBr_xI_{3-x}$ perovskite nanowires were successfully fabricated by a solid-to-solid halide exchange reaction.[11] By facilitating the transportation of charge carriers over a few micrometers and accumulated carriers in the low-bandgap iodide-rich region, the gradient-halide perovskite implies the applications in photon energy delivery and nanoscale optoelectronics.

Although numerous efforts have been made on the bandgap engineering of mixed-halide perovskites, some questions remain unclear to date. First, whether the downward funneling of carriers is through photon recycle or carrier diffusion is unknown. Second, PL shift in mixed-halide perovskites has been intensively observed and described as phase segregation, while the mechanisms is still under debate. For gradient bandgap mixed-halide perovskite, the detailed physical process of phase segregation has not been discussed before.

Moreover, with the tunable bandgap and high PL efficiency, the gradient-bandgap perovskites are of great importance for on-chip light-emitting applications, such as multicolor displays, band-tunable PDs and nano-lasers.[12] To pattern spatially resolved multicolor on perovskites, the direct fabrication of precise micro-patterns is essential on such single perovskite nanoplatelet (NP) with various halide compositions. However, the currently available techniques are multistep methods based on nanofabrication and additional anion exchange treatment. There are opportunities to develop complementary processing techniques for patterning on perovskites to achieve device integration and functionalization.

1.2 Preview of the thesis

The research work presented in this thesis explores experimentally the charge carrier dynamics of perovskite materials, including the diffusion length detection in 2D perovskite thin NPs, the bandgap engineering, and on-chip applications of gradient-bandgap halide perovskite NPs.

This thesis is organized as follows. The updated optical properties as well as applications of perovskite materials are reviewed in Chapter 2. First, the crystalline structure of perovskites is introduced as it determined the properties of the materials. The 2D perovskites and mixed-halide perovskites are then reviewed as superior optical properties and applications are shown in these perovskites. Third, the detailed perovskite applications in solar cells, optoelectronic and on-chip devices are introduced.

To provide a comprehensive understanding of perovskite materials, their charge carrier recombination and diffusion processes are summarized in Chapter 3. After the basic theory, some unsolved problems are discussed in this chapter. For the 2D perovskite thin flakes, the method to determine the carrier diffusion length is quite challenging. For the gradient-halide perovskites, the dynamics of carriers funneling process, as well as the phase segregation phenomenon should make clear. The relevant spectroscopic and nanofabrication techniques used in this thesis are also introduced in this chapter.

A novel technique for determination of in-plane diffusion coefficient/ length in 2D thin perovskite flakes is demonstrated in Chapter 4. Utilizing this technique, both the diffusion coefficient (53.6 cm^2/s) and the diffusion length (1.82 μm) are determined in a thin NP exfoliated from a 2D perovskite single crystal. The method is then applied to a 3D thin perovskite NP. The precision and suitability of the method is further explored, and it is appropriate for 2D and 3D thin films and low-luminescent samples.

The bandgap engineering of gradient-bandgap perovskites is studied in Chapter 5. A mixed-halide perovskite NP with gradual halide composition along the depth is fabricated firstly. The gradient-bandgap structure is confirmed by the energy dispersive spectroscopy (EDS) and photoluminescence (PL) results. When the perovskite NP is detected by the EDS with different e-beam energies, larger iodide peak was shown in larger e-beam energy experiments as the penetration depth is deeper. Under laser illumination, PL spectra with longer wavelength emission was detected in thicker NPs. These results illustrate the effective carrier funneling from bromide-rich region to iodide-rich region in such gradient-bandgap perovskite NPs. The phase segregation phenomenon is observed, indicating stable and irreversible phases are formed under continuous laser excitation.

Combined with the straightforward one-step femtosecond direct laser writing (fs-DLW) fabrication technique, the spatial modulation of fluorescence color in gradient-bandgap perovskite NPs is presented in Chapter 6. Under a controlled fs-laser pulse, the designed amount of perovskites is evaporated and removed accompanied with halide ions exchange, results in micro-scale multicolor emission. The ion-movement during this process is studied. Moreover, arbitrary designed patterns can be achieved in these NPs, implying the potential applications in multicolor displays, micro-encryption, and light-emitting devices.

The thesis ends with a conclusion chapter (Chapter 7), which summarizes the research outcomes presented in the previous chapters and the outlooks towards future work in this field.

Chapter 2

Perovskite Structures and Applications

Perovskite solar cells are regarded as the most promising photovoltaic technologies for the next generation of solar cells. Tremendous progress has been made in less than one decade. At the same time, organic-inorganic hybrid perovskites are also confirmed with a great potential for highly efficient optoelectronic applications such as LEDs, nanolasers and photodetectors.

The success of halide perovskites in photovoltaic and optical-electronic devices has triggered huge research interests, crossing from the fundamental knowledge to the applications. The intrinsic physical and electronic properties of the perovskite have been widely investigated. This chapter focuses on the intrinsic crystalline structures and optoelectronic properties of perovskites as well as their various applications.

2.1 Organic-inorganic perovskite structures

2.1.1 Crystalline structure and compositions of perovskites

The general formula of a typical halide perovskite is ABX_3, where the A site is a monovalent cation (e.g., methylammonium, $CH_3NH_3^+$ or MA^+), B site is a bivalent cation (e.g., Pb^{2+}, Sn^{2+}) and X site is a halide (I^-, Br^-, Cl^-). The crystal structure is illustrated in Figure 2.1,[13] there are eight octahedra of lead halide with a cation at the center. The octahedra can be tilted or rotated by the replacement of different halide ions, which directly adjusts the bandgap of this material.[13] The size of cation A is the key aspect for the formation of a close-packed perovskite structure. It is required to fit into the space between the four adjacent octahedral, which are connected through corner-sharing.[14] For organic-inorganic perovskite, the A site is usually occupied by MA^+ or FA^+ (formamidinium, $HC(NH_2)_2^+$).

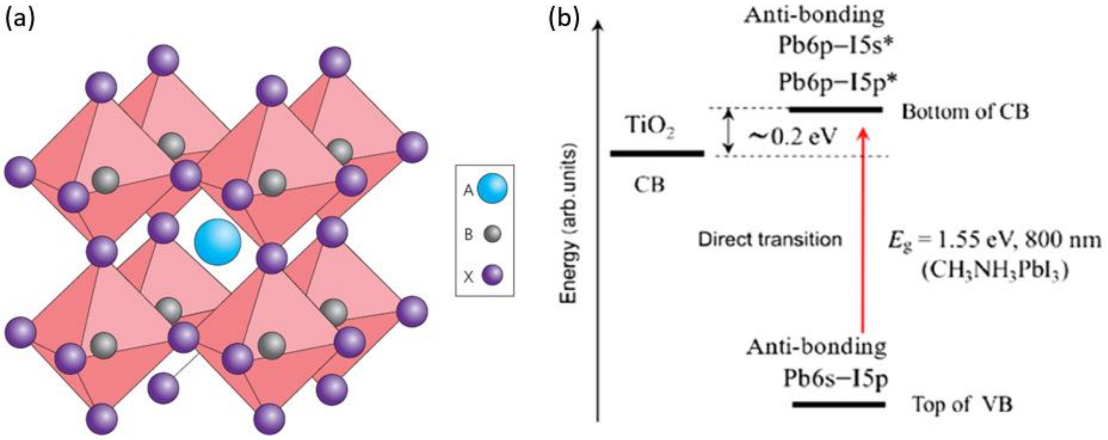

Figure 2.1 (a) Crystal structure of a typical cubic ABX_3 perovskite.[13] (b) Bounding diagram of $MAPbI_3$ perovskite.[4]

Figure 2.1(b) shows the band-gap structure and energy levels of $MAPbI_3$ single crystals based on the DFT calculations by Koutselas et al. and Brivio et al. These calculations revealed the bandgap energy is determined by the $[PbI_4]^{6-}$ network. The organic part was not shown in the diagram as it has little influence on the bonding energy. The VB maxima consists of Pb 6s-I 5p orbitals (lone pair), while the CB minima comprises a mixture of Pb 6p–I 5s and Pb 6p–I 5p orbitals. This high symmetry and electronic structure thus contribute to the direct bandgap and high absorption coefficient of perovskites. Moreover, these unique bounding coupling, as well as ionic characteristics of perovskite, have a great influence on their defect properties. The lead vacancies lie between the I p atomic orbital and VB maxima, and the halide vacancies are formed between the Pb p and CB minima. As these defects are shallow defects, carriers can easily detrapped, leading to longer lifetimes and carrier diffusion lengths.

One fascinating property of ABX_3 hybrid perovskites is their structural versatility to incorporate different kinds of anions/cations, which results in a change in the physical and chemical properties of the materials, including crystal structure parameters, bandgaps, carrier behaviors, defect properties, phase stabilities, and moisture and/ or thermal resistance.[15-17] For example, $MAPbI_3$ is a classical perovskite material for solar cells, which has a high PCE performance.[18] With a slightly larger ionic size, the FA cation based $FAPbI_3$ perovskite exhibits improved charge transport properties.[19]

2.1.2 Two-dimensional perovskite materials

2D perovskites have been considered as emerging materials of significant potential for optoelectronic applications. By inserting long organic spacer cations into the ABX_3 frameworks, 2D perovskites are formed upon crystallization of 3D ABX_3 perovskites. Compared to their 3D counterparts, 2D perovskites are more stable to humidity and ambient atmosphere, which offer new opportunities to design optoelectronic devices.

The Ruddlesden–Popper perovskites are the most widely investigated 2D perovskites. Far more tunability and flexibility are offered by these materials, making the physical properties able to be controlled.[20] The name of Ruddlesden–Popper perovskites originated from their similarity in crystal with inorganic Ruddlesden–Popper perovskites such as Sr_3TiO_7.[21] These perovskites are achieved by slicing 3D perovskite structure into layers of different n-values. The generic chemical formula of 2D perovskites is $(RA)_2(A)_{n-1}BX_{3n+1}$, where RA is the long-chain spacer between different layers. A, B, X are cations and anions from the 3D perovskite framework. In most cases, the long-chain RA cation is a primary amine such as phenethylammonium (PEA) or butylammonium (BA), while the short-chain A cation is the organic cation such as MA, FA or inorganic cation such as Cs. The value n represents the numbers of layers, as shown in Figure 2.2. When n=1, the BX_4^- structure is sandwiched between two RNH_3 organic layers. With an increased n number, continuous layers with defined integral number are sandwiched. When n equals to ∞, the perovskite has a near pure 3D structure.[22] By controlling the n-values, the optoelectronic properties can be managed to get appropriate characteristics for each application. The control of the number n would lead to different quantum confinement effects in 2D perovskite. Stokes shift in absorption and PL, significant enhancement in photoluminescence quantum yield (PLQY), larger exciton binding energy, and higher stability are induced by the quantum confinement, leading to various applications of 2D perovskites.[23]

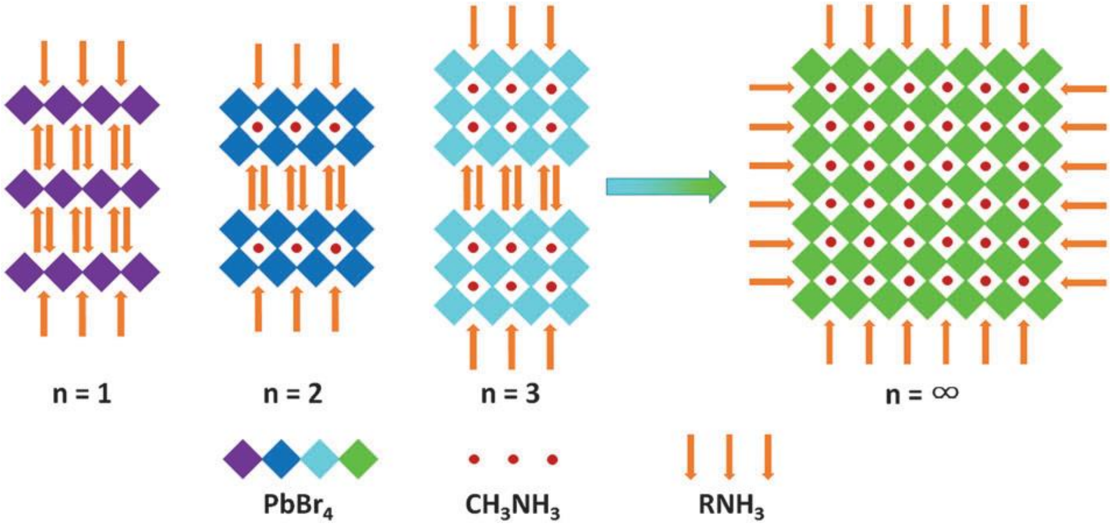

Figure 2.2 The schematic layered structures of perovskites from 2D to 3D, i.e. $(RA)_2(CH_3NH_3)_{n-1}Pb_nBr_{3n+1}$, n = 1, 2, 3. . . ∞.[22]

2.1.3 Mixed-halide perovskite materials

The flexibility of the ABX_3 structure allows for a degree of ionic mixing on the crystal lattice sites, these mixed perovskite materials can be used to tune the structural properties of the perovskite.[24] Despite the excellent properties such as long carrier diffusion lengths[25], high optical absorption coefficients[26] and high defect tolerance that are ideal for highly efficient photovoltaic devices, pure perovskite materials suffer from structural instability or non-ideal bandgaps for perovskite applications. By mixing up the individual sites (A, B or X) or multiple sites, mixed perovskites have proven a feasible solution for improved stability and better optoelectronic properties.

The A-site mixed perovskite materials are normally based on the mix of MA, FA, Cs, and Rb cations. For instance, mixing FA^+ with MA^+ would result in perovskite with improved stability and optoelectronic properties.[26-27] Another distinct benefit attribute of mixed-cation perovskite materials is the ability to continuously tune the bandgap. For example, the gradual replacement of the MA cation in $MAPbI_3$ by the larger cation

FA through the film was shown to be able to tune the bandgap between 1.57 and 1.48 eV, exhibiting superior optoelectronic properties and better thermal stability than that of $MAPbI_3$[28].

For mixed halide perovskite, as the halide ion exchange reaction undergoes easily, the substituted halide component offers the finest tuning of the optical properties.[29] By altering the composition of the halide ions on the X-sites of the crystal structure, the corresponding bandgaps of $FAPb(I_xBr_{1-x})_3$ perovskite can be continuously tuned over the range of 1.48 to 2.23 eV,[30] while for $MAPbX_3$ (X = Cl, Br, I) perovskite nanocrystals, the bandgap range is 1.6 to 2.3 eV.[31] The normalized photoluminescence spectra of these mixed-halide perovskites are shown in Figure 2.3.

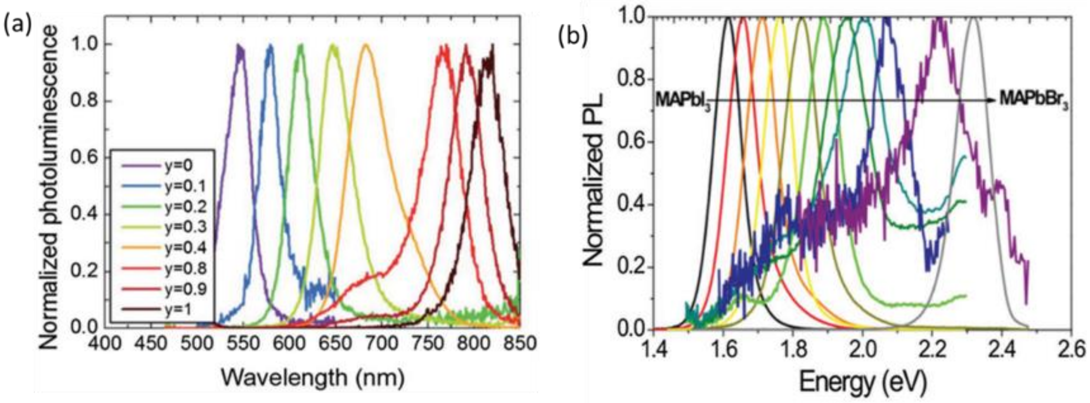

Figure. 2.3 Normalized photoluminescence spectra of the (a) $FAPbI_yBr_{3-y}$ and (b) $MAPb(Br_xI_{1-x})_3$ thin films.[30-31]

2.2 Recent progress in perovskite applications

2.2.1 Solar Cells

The global increasing consumption of energy, together with the decreasing supply of fossil fuels have driven the development of energy from renewable sources.[32] As the most abundant energy resource, harnessing solar power would yield a never-ending energy supply. Photovoltaic solar cells are thus the most promising avenue for directly convert the energy of sunlight into electricity based on the photovoltaic effect and for this reason they have been regarded as a very promising energy generation source.[33]

However, for photovoltaic energy to become competitive with fossil fuels and to capture a significant share of the electricity market nowadays, it is always difficult to convert solar energy in an efficient and cost-effective way. A number of different types of solar cell technologies have been explored, including silicon solar cells and advanced photovoltaic technologies like quantum dots solar cells, organic solar cells and dye-sensitized solar cells.[34]

Among these technologies, perovskites have attracted significant attention in the field of photovoltaics recent years for highly efficient solar cell devices due to their high PCE as well as the low-cost solution-based manufacturing method. Figure 2.4 (a) shows a typical solar cell based on organic-inorganic halide perovskite. The PCE of the solar cells have already exceeded 25% since the first reports of perovskite solar cells in 2009 (shown in Figure 2.4 (b)).[4] Miyasaka and co-workers were the first to report photovoltaic results for perovskite solar cells. By replacing bromine with iodine, they were able to fabricate a $MAPbI_3$ based cell, realizing PCE of 3.8% and high photovoltages close to 1.0 V.[2] After the development of more than ten years, halide perovskites are already competitive with commercial thin-film cells like silicon cells. Currently, the highest PCE of perovskite solar cells (25.2%) is achieved by KRICT (South Korea). They used nickel oxide (NiO_x) as a highly efficient hole conductor layer, which is deposited over a large area. NiO_x is an inexpensive material and it has ability to withstand high temperatures up to 70 °C. The layers were deposited by rotatory coating method.[35] The high PCE recent years have demonstrated that these low-cost perovskite materials are promising for commercial viability and applications.

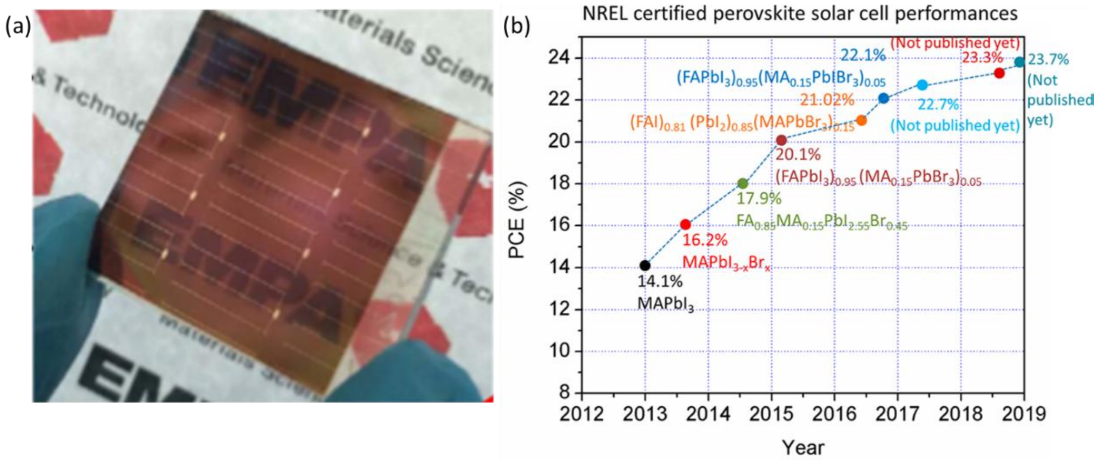

Figure 2.4 (a) A photograph of $MAPbI_3$ based perovskite solar cell device.[36] (b) Perovskite solar cell performances certified by NREL.[4]

2.2.2 Optical applications

In addition to solar cells, organic-inorganic perovskites are expected to be promising materials for next generation lighting and display, and other photonic applications. Many interesting results have been observed recently, and the progresses in optoelectronic devices and optical applications, such as LEDs and PDs.

A LED is an electronic component that is essentially a two-lead semiconductor light source. According to the Shockley-Queisser limit, efficient solar cell materials are also promising candidate for good light emitters such as LEDs.[37] The LED is a p-n junction diode that emits light upon activation by a voltage applied to the leads, which makes electrons recombine with holes within the device, releasing energy in the form of photons.[38] This effect is called electroluminescence, and the color of the light is determined by the energy band gap of the chosen semiconductor.

Organic-inorganic halide perovskites with good charge mobilities and high PLQEs in visible and near-infrared range thus were also investigated in high performance LED applications.[39] Layered 2D organic–inorganic perovskites were first used as perovskite LEDs in 1990s. 3D halide perovskites-based LEDs were also demonstrated recently. Figure 2.5 (a) shows a greenlight-emitting diode based on $MAPbBr_3$ nanoparticles.[40] Moreover, by adjusting the ratio of different halides in mixed $MAPbX_3$ (X = halide) perovskites, the emission spectra of the products can be tuned from blue to red (Figure 2.5 (b)).[40]

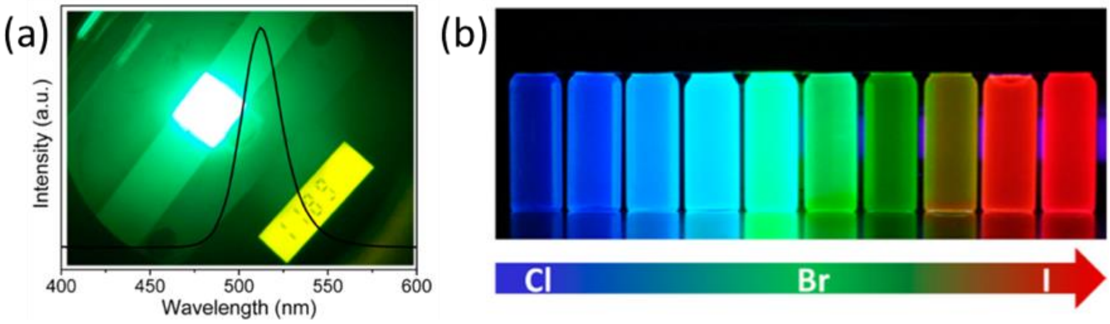

Figure 2.5 (a) Electroluminescence spectra of $MAPbBr_3$ LED at a peak wavelength of 512 nm, and the image of the resulting device operating at a luminance.[40] (b) Digital image of perovskite colloidal solutions in toluene under UV lamp with light emission from 438 to 660 nm.[40]

Photodetectors are important in optical communication, chemical sensing, environmental monitoring, and many other industrial applications due to their ability to detect light (visible or infrared) and to convert the light into electrical signals. Due to their unique optoelectronic properties such as broad and tunable light absorption, superior charge transport and efficient free electron-hole generation, organic-inorganic halide perovskites have also shown great potential in the photo detectors.[41] In 2014, Hu et al. reported the first perovskite photodetector. This photodetector was designed on $MAPbI_3$ thin films, with high sensitivity, high speed and broad photoresponse range.[42] Compared with other inorganic semiconductors normally used for photo detectors such as Si and GaN, perovskites are more promising materials due to their low cost and high quantum efficiency. Another example was a high-performance photodetector demonstrated by Liu et al.[43] As shown in Figure 2.6, the 2D $MAPbI_3$-based phototransistor devices were fabricated on a SiO_2/Si substrate, the current can be enhanced significantly by shining 405 nm and 532 nm lasers in their PDs, showing photo responsivities of 22 and 12 AW^{-1} with a voltage bias of 1 V respectively.[44] The organic-inorganic perovskites are promising for further practical applications in PDs as they are highly sensitive in detecting broad wavelengths of light, from UV to visible light, as well as the near infrared light.

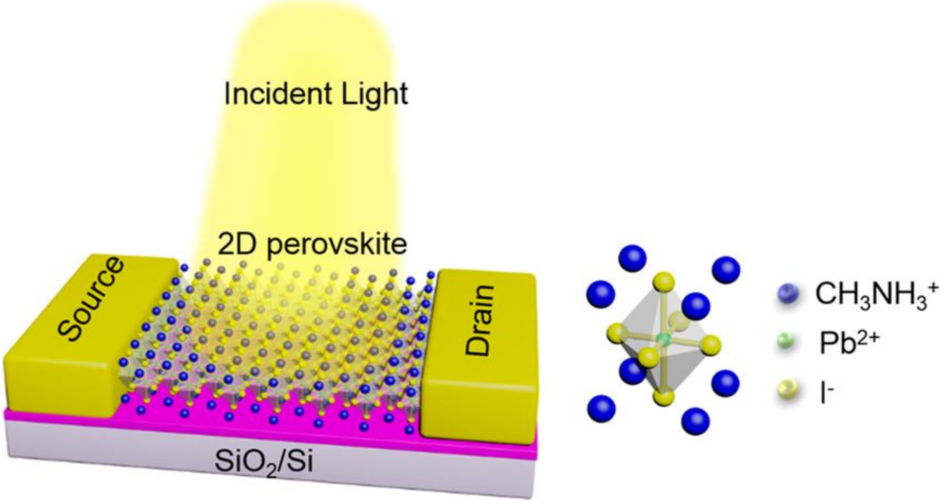

Figure 2.6 Schematic image of a transistor device based on 2D perovskite.[44]

2.2.3 On-chip optical applications

In addition to the above-mentioned exciting applications, hybrid perovskites can achieve further improvements by combining with nano structures. With the developments of nanofabrication techniques, there are unprecedented possibilities for on-chip optical applications of perovskites.

For example, the introduction of optical microcavities into PD devices is considered as an approach to improve detection performance.[45] With the field enhancement at the selected wavelength by microcavities, and perfect light absorption by perovskite materials, the detection performance can be significantly improved.

Various perovskite nano-lasers have been demonstrated as well, including microdisk laser, distributed feedback laser and photonic crystals laser. These nano-lasers are achieved in perovskite nanowires, microplates, quantum dots and single crystals. For instance, Zhu et al. illustrates a wavelength-tunable lasing from single-crystal lead halide perovskite nanowires with very low lasing thresholds (220 $nJ\cdot cm^{-2}$) and high quality factors ($Q \sim 3600$).[46] The emission spectrum and optical image of an $MAPbBr_3$ NW is illustrated in Figure 2.7 (a). Shunemann et al. proposed a distributed feedback laser based on a photonic crystal nanostructure with long-term operational stability and low threshold.[47] The excellent intrinsic optical properties, the smooth facets of the perovskite grains, as well as the advancements in device engineering, have replicated their potential into nano-laser devices. The scanning electron microscopy (SEM) of a $MAPbBr_3$ perovskite for distributed feedback laser is shown in Figure 2.7 (b).

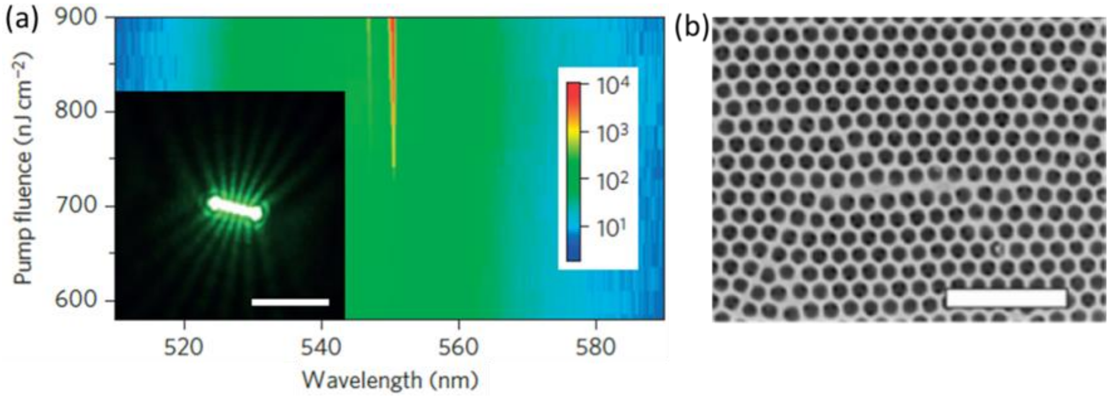

Figure 2.7 (a) 2D pseudo-colour plot of nanowire emission spectrum as a function of pump fluences for a 7.5 μm $MAPbBr_3$ nanowire. The insert is the emission image of the nanowire above the lasing threshold.[46] (b) Cross-sectional SEM of a $MAPbBr_3$ perovskite for distributed feedback laser. The scale bar is 2 μm.[47]

Chapter 3

Carrier Recombination and Diffusion Process in Perovskites

This chapter focuses on the basic theories of charge carrier dynamics in perovskites, including both carrier recombination and diffusion processes. Based on these theories, some research questions are listed in this chapter, which will be solved at the following chapters. The techniques used in this thesis are also introduced in this chapter. Generally, a cascade of physical effects occurs over different timescales in perovskite materials under a short laser pump pulse excitation. First, hot carrier cooling occurs usually within few picoseconds for conventional semiconductors but could be slowed down in perovskites due to phonon bottleneck effect.[48] After this process, carrier recombination occurs by several pathways: defect trapping, electron-hole recombination directly and Auger recombination. Carrier diffusion and photon absorption also happens during this timescale, making the carrier dynamics more complicated. The process is shown in Figure 3.1.[49]

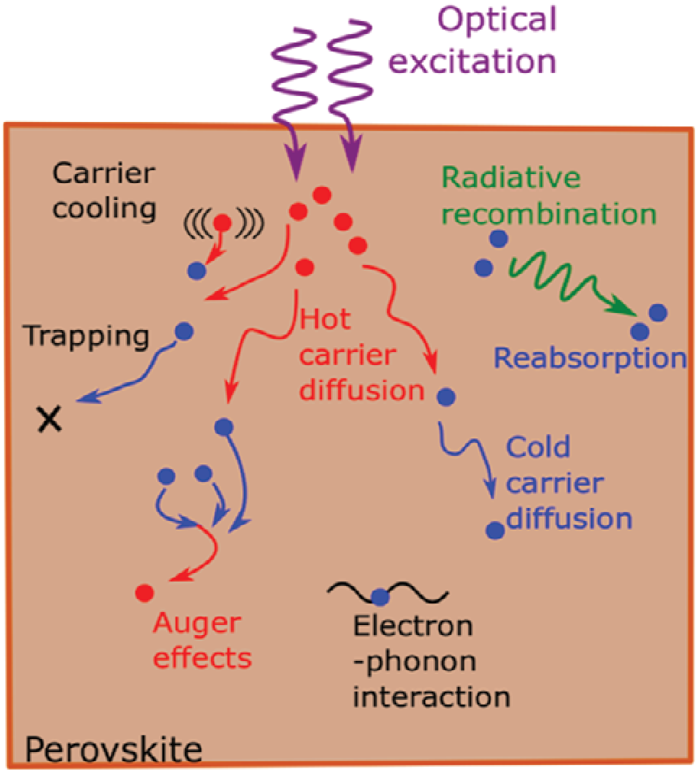

Figure 3.1 Schematic highlighting key charge carrier processes following photoexcitation of the perovskite.[49]

3.1 The carrier recombination properties of perovskites

3.1.1 Carrier recombination process in 3D perovskites

Upon photoexcitation, carriers can be pumped to a high energy state in the conduction band (CB) that is determined by the photon energy of the laser. These excited carriers quickly form Fermi–Dirac statistics that can be described by the carrier temperature. Hot carriers are the carriers with extra dynamic energy, which is represented by a higher temperature than the lattice. Within a few picoseconds, the hot carriers can rapidly relax to the edge of the CB though electron-phonon scattering.[50] The hot carrier cooling process is ultrafast, which occurs prior to the carrier recombination. Before laser excitation, the perovskite lattice is under the thermal equilibrium state. The high-energy photons are absorbed extremely fast and forms coherent carriers after laser excitation.[51] Then, the excited carriers will dephase and redistribute, and result in the formation of Fermi-Dirac statistics, which is called the carrier thermalization process. Following the optical phonon scattering and acoustic phonon scattering, the hot carriers relax to the edge of the CB in few to tens of picoseconds. Lastly, the acoustic phonon emission will decay and lose energy within hundreds of picoseconds.

After the hot carrier cooling event, photo-carriers at the band edge undergo a recombination process over the tens of picoseconds to microsecond timescales. The recombination occurs via several pathways, including defect trapping, carrier radiative recombination and Augur recombination. Photon recycling, diffusion and reabsorption undergo at the same time, impacts the whole recombination process.

To understand these competing processes, the kinetics of the evolution of carrier density are investigated by the rate equation:[52]

$$\frac{dn}{dt} = G \cdot \delta(\mathrm{t}) - k_1 n - k_2 n^2 - k_3 n^3 + D\nabla^2 \qquad (3\text{-}1)$$

Where n represents the carrier density, t is the time, $G \cdot \delta(\mathrm{t})$ is the charge generation through pulsed laser injection. The Shockley−Read−Hall (SRH) recombination via sub-bandgap trap states, free electron−hole recombination, and Auger recombination are represented by $k_1 n, k_2 n^2$ and $k_3 n^3$respectively.[52] The term $D\nabla^2 n$ corresponds to the charge carrier diffusion process. These competing pathways are explained in detail:

In general, the trap states are mostly located at the grain boundaries, perovskite surfaces and interfaces due to a higher possibility of crystal-structure deformation. Chemical composition also has an impact on the trapping densities. These defects are illustrated in Figure 3.2.[53] $MAPbI_3$ perovskite structure is used as an example, point defects like Pb^+ and I^- vacancies, interstitial I^-, Pb_2^+, and Pb-I antisite (Pb_I, I_{Pb}) are the recombination centers for trapping electrons and holes. These point traps are more likely to give rise to deep levels in the bandgap. While grain boundary and surfaces, where the structure is suddenly interrupted, will forming shallow levels with low forming energy.[53]

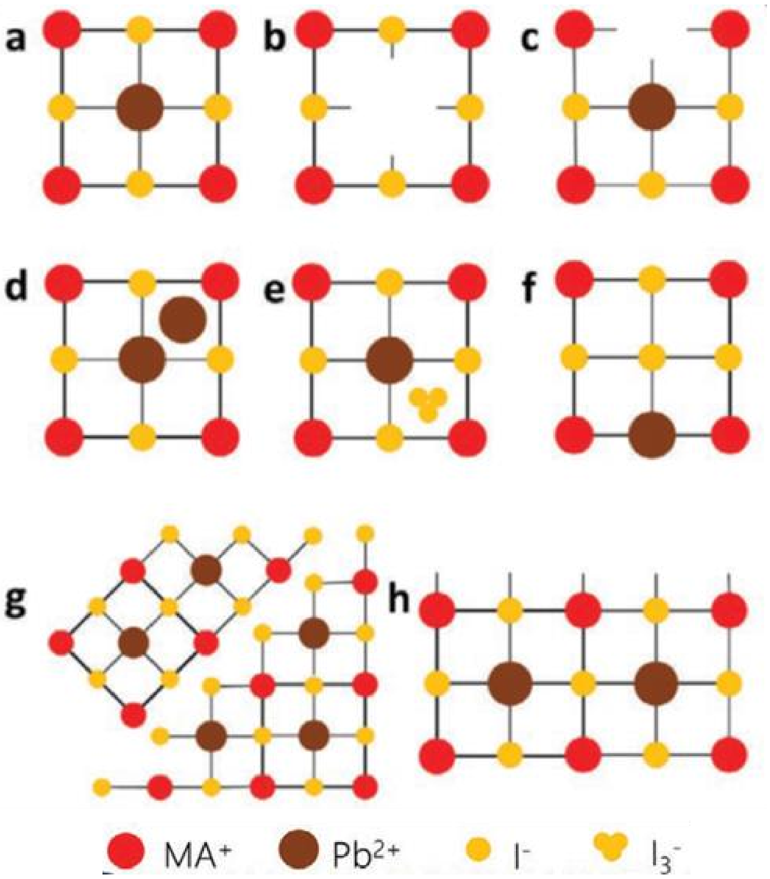

Figure 3.2. Schematic illustration of typical defects in PSCs: (a) perfect lattice, (b) Pb_2^+ vacancies, (c) I^- vacancies, (d) interstitial Pb_2^+, (e) interstitial I_3^-, (f) Pb-I antisite substitution, (g) grain boundary, and (h) dangling bonds on the surface. [53]

Ideally, without defect trapping or Auger recombination, all charge carriers will be diffused and collected by electrodes when solar cell is under operation. In neat perovskites, these carriers will undergo radiative recombination, which is responsible for the PL emission. As the exciton binding energy (E_b) of bulk perovskites are lower than the thermal energy (26 meV), free electrons and holes, rather than excitons, dominantly exists in 3D perovskite structures. These free electrons in the CB radiatively recombine with the free holes in the valence band (VB), leading to the photon emission.

Auger recombination involves three carriers: one electron−hole pair recombines nonradiatively by exciting another carrier into a higher energy level.[54] The energy and momentum required in the three bodies to finish the process is quite strict, which depends on the electronic band structure within the perovskites. The Auger nonradiative recombination process also depends on charge-carrier concentrations. It is only reasonable when the excitation density is high.

Under low excitation fluence, Auger recombination is usually negligible. In this case, defect trapping state and carrier radiative recombination process are dominant mechanism for the carrier recombination. A simplified dynamics model can be established:

$$-\frac{dn}{dt} = An + Bn^2 \qquad (3\text{-}2)$$

where An indicates a first-order process via defect trapping and Bn^2 is the bimolecular recombination. Figure 3.3 (a) gives an example of the time-resolved photoluminescence (TRPL) of a perovskite film.[55] At low excitation intensity ($< 10^{15}$ cm^{-3}), the TRPL shows a single exponential decay, indicating the dominance of trap-assisted nonradiative recombination. With larger excitation, more trap-states are saturated, leading to the larger portion of radiative recombination. The scheme of the saturation of the sub-bandgap trap states is shown in Figure 3.3 (b).[56]

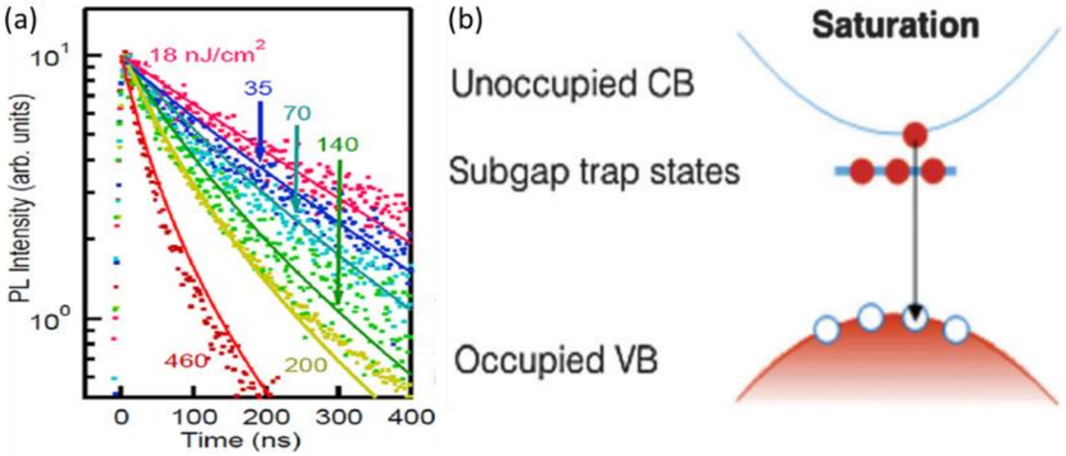

Figure 3.3 (a) PL dynamics of a MAPbI$_3$ film under different excitation intensities.[55] (b) Scheme of the saturation of the sub-bandgap trap states.[56]

The effective lifetime can be extracted by the biexponential function fitting of the TRPL curves: $I(t) = A_1 \exp\left(-\frac{t}{\tau_1}\right) + A_2 \exp\left(-\frac{t}{\tau_2}\right)$. Where $A_1 \exp\left(-\frac{t}{\tau_1}\right)$ represent the fast decay and $A_2 \exp\left(-\frac{t}{\tau_2}\right)$ represent the slow decay. The decay lifetime (τ_1, τ_2) and weight ratio (A_1, A_2) of each decay can be used for the calculation of the effective lifetime:$\tau_{eff} = A_1\tau_1 + A_2\tau_2$. In this fitting model, the defect trapping is responsible for the fast decay, while the electron-hole recombination is represented by the slow decay.

3.1.2 Excitons recombination process in 2D perovskites

In 3D perovskites, the carriers are recombined via trap state, direct bimolecular recombination and Auger recombination processes. However, the excitons, instead of free electrons and holes, are dominant in the dimensionally controlled 2D perovskites, because the electrons and holes are bound in an excitonic state due to quantum and dielectric confinement effects. The Coulomb interaction in 2D perovskites is strictly screened, because of the high contrast in dielectric constants of the organic layers and inorganic layers. Therefore, the electron-hole interaction within the exciton is very strong, resulting in huge oscillator strengths and very large exciton binding energies.[57] In this case, excitons will recombine after laser excitation, as illustrated in Figure 3.4.[58] For instance, Blancon et al. have demonstrated properties of unexpectedly strongly bound excitons (> 120 meV) experimentally and theoretically in $(BA)_2(MA)_{n-1}Pb_nI_{3n+1}$ perovskite with $n \leq 5$.[59] The exciton binding energy of different n-values is shown in Figure 3.5(a). To make a comparison, the binding energy is extremely low in the case of 3D perovskites (65 − 75 meV for $MAPbBr_3$ vs 15 − 50 meV for $MAPbI_3$), which facilitates quick charge separation at room temperature.[58]

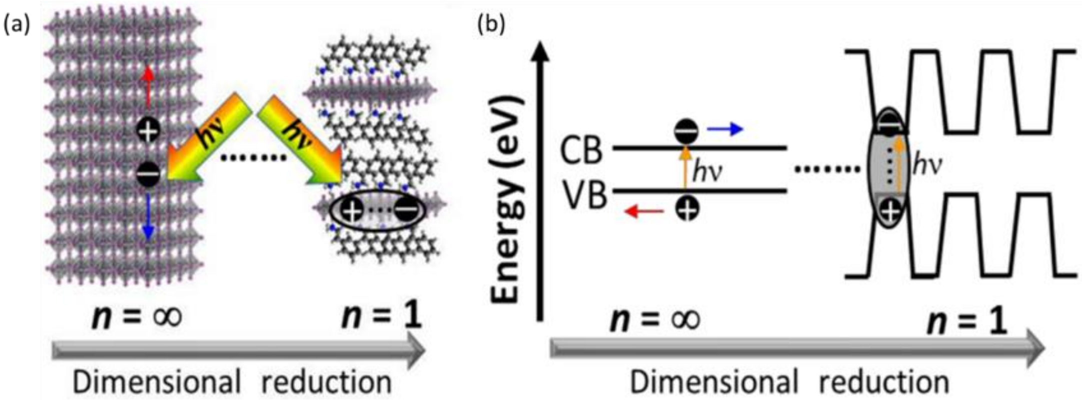

Figure 3.4. (a) Dimensionality effect on generation and recombination of charge carriers and (b) energy landscape in the 3D and 2D perovskites. The electrons and holes are dissociated in the 3D perovskites while bound in the 2D structures because of quantum and dielectric confinement effects.[58]

With the ultra-high binding energy and quantum confinement effects in 2D perovskites, effective band gap and absorption characteristics are increased compared to the 3D perovskites. Both the PL spectrum and the absorption band-edge peak blue-shift with increasing RA fraction (decreased n-value) of 2D perovskites, indicating a decreased dimensionality of the perovskite film. The normalized PL spectra and bandgap energy of 2D perovskites with different n-values are illustrated in Figure 3.5(b, c).[58-59] In addition, the reduced dimensionality leads to faster charge carrier recombination in 2D perovskites (Figure 3.5(d)).[58] The increased exciton binding energy makes the charge separation less facile, at the same time the stronger quantum confinement results in stronger interaction between the photogenerated carriers thus decreasing the carrier lifetime.

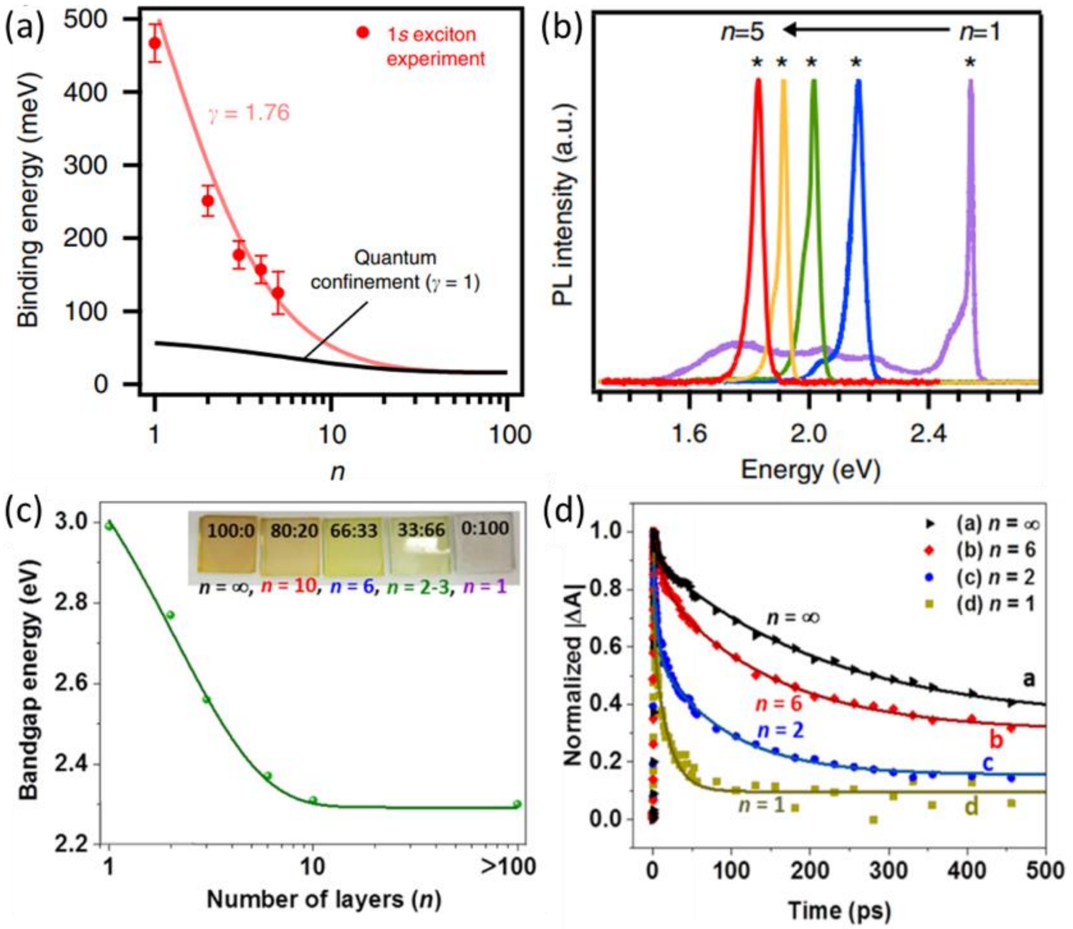

Figure 3.5. (a) The exciton binding energy and (b) photoluminescence spectra of different n-values of $(BA)_2(MA)_{n-1}Pb_nI_{3n+1}$ perovskite, showing the enhancement of the binding energy due to dielectric confinement.[59] (c) Optical bandgap energy and (d) bleach recovery and biexponential kinetic fits probing the bleach maximum of $(PEA)_2(MA)_{n-1}Pb_nBr_{3n+1}$ perovskite with different n-values.[58]

3.1.3 Mobile ions in perovskites

As the ABX_3 perovskite materials show ionic crystal characteristics, a large number of mobile ions such as A^+, X^- or A cation and X anion vacancies exist in organic–inorganic halide perovskites. These mobile ions are observed as defects, as discussed in Chapter 3.1.2, which will enlarge the proportion of nonradiative recombination of perovskites.

Despite carriers trapping states, ion migration and accumulation occur in perovskites under light illumination. The ion migration can be observed by the PL wavelength change in mixed-halide perovskites, as the bandgap shows difference with the halide component change in perovskites. Despite the improvement of photovoltaic performance by better capturing the full solar spectrum, mixed-halide perovskites exhibit unwanted phase segregation under continuous light irradiation. This phenomenon has attracted considerable research interest recently because it is closely related to carrier extraction and hence to the performance of perovskite solar cells. The PL spectra of hybrid perovskites discretely blue-shift or red-shift, indicating halide ions segregate into separate bromide-rich or iodide-rich domains. For instance, under continuous optical irradiation, $MAPb(I_{0.5}Br_{0.5})_3$ thin films was reported to show a decrease in the native emission at $\lambda_{mix} = 652$ nm accompanied by a corresponding rise of emission features at 725 and 527 nm associated with $MAPbI_3$-like or $MAPbBr_3$-like photoluminescence.[60] Another work based on $FAPb(Br_{0.67}I_{0.33})_3$ film shows that the original PL almost completely shifts to a new dominant low-energy PL feature, in accordance with higher PL emissivity of the iodide-rich phases.[61] As depicted in Figure 3.6, Eric Hoke etc. showed that under continuous illumination, the initial $MAPb(Br_{0.4}I_{0.6})_3$ PL spectra at 1.85 eV was decreasing, while an additional PL peak forms and increases at 1.68 eV.[62] Although phase segregation in mixed-halide perovskites has been intensively observed, the observations display much discrepancy, and the detailed physical process is still under debate.[31, 63-66] Mobile ion migration is one of the possible physical mechanisms: the mobile ions are activated under laser excitation, and halide substitution occur during this process, leading to the phase segregation in these perovskites.

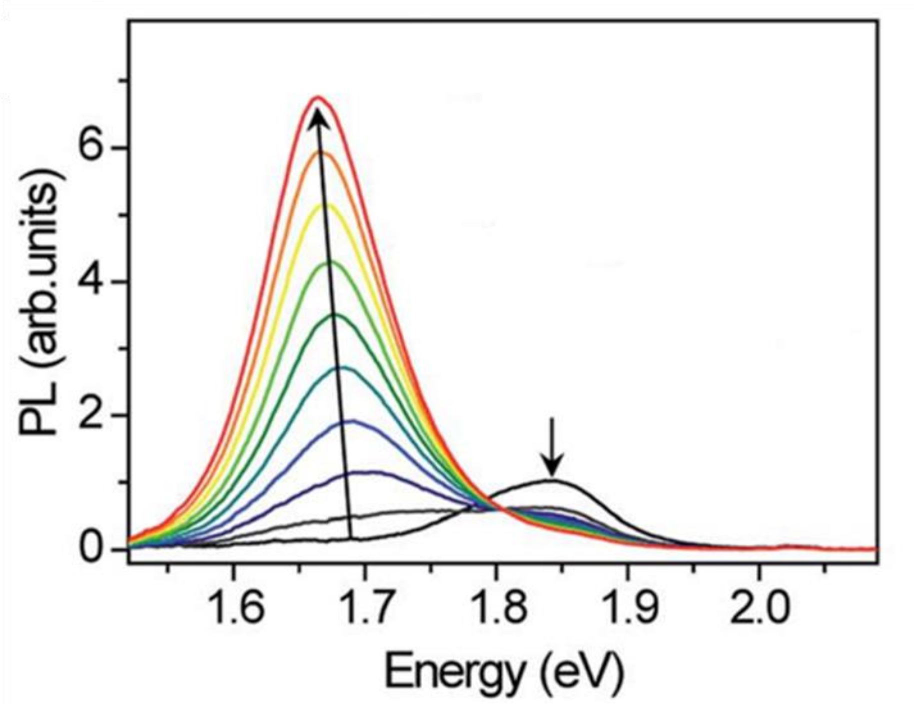

Figure 3.6 PL spectra of an $MAPb(Br_{0.4}I_{0.6})_3$ thin film over 45 s in 5 s increments under 457 nm, 15 mW cm^{-2} light at 300 K.[62]

3.2 The diffusion process of charge carriers

3.2.1 Carrier diffusion dynamics of perovskites

Carrier diffusion is a random motion of electrons and holes in space that leads to spreading from the areas of high concentration to the areas of low concentration. The diffusion process of perovskites is crucial for highly efficient solar cells. To make sure photogenerated charge carriers in perovskite absorber films can be efficiently extracted before recombining, a proper thickness of perovskite film should be consistent with the diffusion length. Therefore, the estimation and calculation of the diffusion coefficient (D) and diffusion length (L) is crucial for the optimization of perovskite solar cell devices.

Basically, in neat perovskite films, the diffusion coefficient is described by the equation 3-1,[55, 67-68] in which the term $D\nabla^2 n$ corresponds to the ambipolar diffusion of charge carriers, quantified through the diffusion coefficient D. The parameter D is normally calculated by fitting the PL decay trace of perovskite materials to equation 3-1. With a given D, the carrier diffusion length can be calculated via $L = \sqrt{D\tau}$, where τ is the carrier lifetime. [55, 67-68] For example, Tian et al. report the direct visualization and quantitative characterization of the carrier diffusion process in individual single-crystal perovskite NPs using TRPL and PL-scanned imaging microscopy (Figure 3.7).[68] The scheme of the diffusion process detection is shown in Figure 3.7 (a), after excitation pulse from a fixed excitation spot, the change of carrier density at different positions is monitored by the TPPL as a function of the delay time. This then constructs a PL kinetics image that reflects the spatial distribution of charge carriers in the perovskite sample. After been fitted by the diffusion model (equation 3-1), the diffusion parameters can be extracted. Figure 3.7 (b, c) shows the PL image and PL kinetics of a $MAPbBr_3$ NP as an example. The diffusion parameters can be quantitative determined by these PL kinetics data.

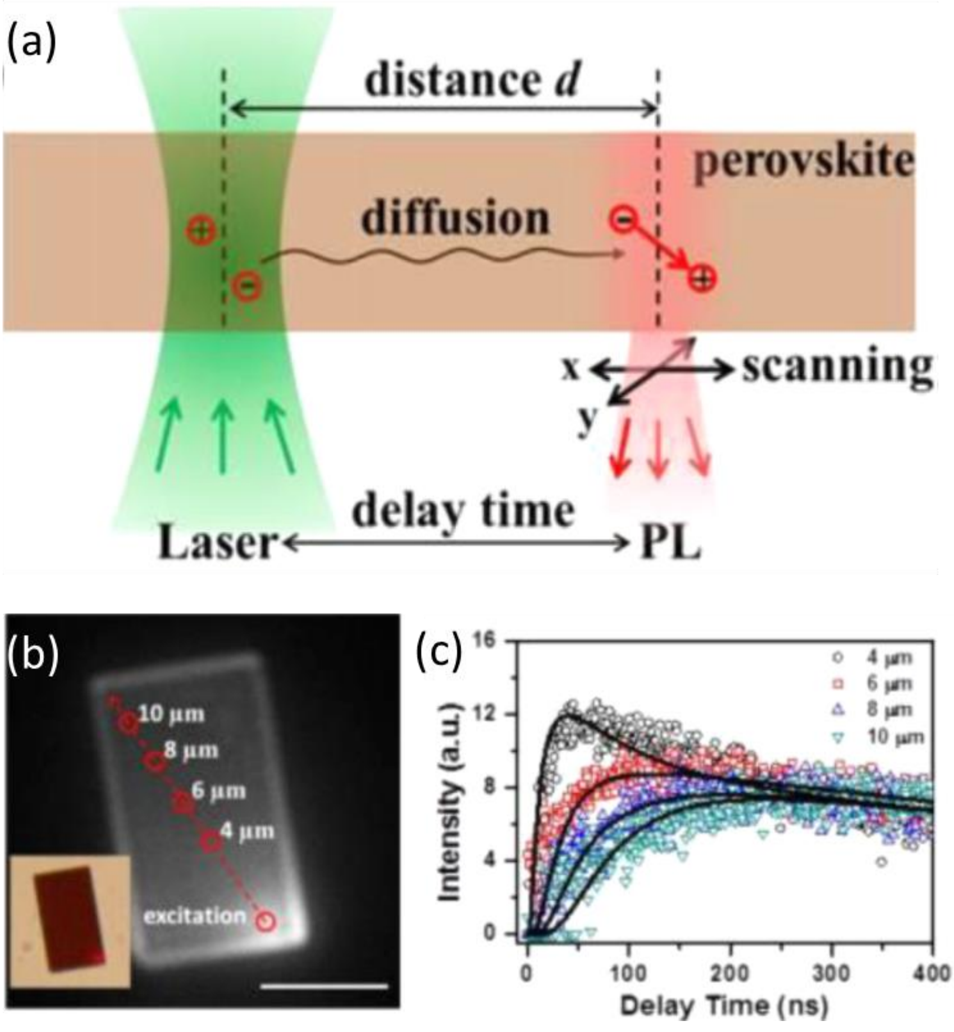

Figure 3.7 (a) Schematic presentation of the charge carrier excitation, diffusion, and recombination processes in perovskites. (b) The PL intensity image, optical image (inset) and (c) a set of PL kinetics collected at different diffusion distances of a $MAPbBr_3$ NP. The scale bar is 5 μm.[68]

Moreover, the electron diffusion length or hole diffusion length can be extracted alone by the PL–quenching measurement. Topped with an electron/hole quenching layer, the electron/hole will diffuse rapidly to the quencher, and the diffusion equation downsize to one-dimension.[69] The electron/hole diffusion parameters can be obtained by modeling the TRPL dynamics of the original perovskite sample and the sample with electron/hole quencher. For instance, both electron and hole diffusion lengths larger than 1 μm are determined by this method in mixed halide perovskites, which is consistent with superior performance in meso-superstructured solar cells and planar heterojunction solar cells.[69]

3.2.2 In-plane carrier diffusion in 2D perovskites

Upon laser excitation, excitons are promptly generated in 2D perovskites instead of free electrons and holes in 3D perovskites. The few-atom thick anionic layers are isolated from one another by means of the organic spacer cations,[70] which suggests the diffusion of excitons are suppressed in the in-plane direction in anionic layers, as illustrated in Figure 3.8 (a). By changing the n-values, different optoelectronic properties were observed by Milot et al., as shown in Figure 3.8 (b).[71] As the n-value of 2D perovskites increases (%PEA increases), quantum confinement effects and exciton binding energy decreases, the charge carrier mobility increases while the direct recombination decreases. The monomolecular recombination rate is affected by two counteracting trends, decreasing first with increasing PEA content due to a trap passivation effect but then increasing as excitonic recombination is enhanced.[71]

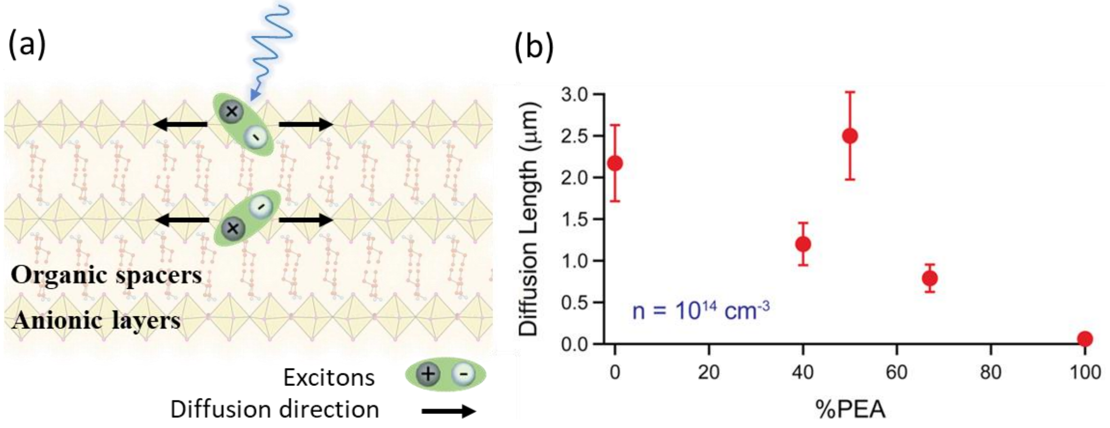

Figure 3.8 (a) Illustration of in-plane diffusion of excitons in 2D perovskites. (b) Charge carrier diffusion length of $MAPbI_3$, $(PEA)_2PbI_4$, and intermediate mixed MA−PEA 2D perovskites.[71]

3.2.3 Downward funneling in gradient-bandgap perovskites

A long carrier diffusion length is crucial for the perovskite-based devices. Beside the polycrystalline and single crystals with diffusion lengths up to micrometers, the perovskite structure whose carrier diffusion is driven by the gradient bandgap has been reported recently. As the carriers will flow directionally from high-bandgap region to the low-bandgap region in the sample, the carrier diffusion length is naturally long. For example, Tian.et al. has reported halide compositional gradient $MAPbBr_xI_{3-x}$ perovskite nanowires with the gradually decreases density of the mixed bromide anion from one end to the other.[11] Driven by the energy funnel, the charge carriers transport in a one-way direction over a few micrometers and accumulated carriers in the low-bandgap iodide-rich region. In their gradient $MAPbBr_xI_{3-x}$ nanowires, carrier transportation driven by the energy funnel delivers ~60% of carriers over a distance of >2 μm.[11]

A multicomponent multilayered $PEA_2MA_{n-1}Pb_nI_{3n+1}$ perovskite film exhibit record high photoluminescence quantum yield (10.6%) under low excitation fluences was reported by Sargent and co-workers.[12] They attribute this advance to the conveyance of excited carriers in a funneling mechanism that provides carrier concentration, enabling more efficient radiative recombination and thereby overcoming the trap-mediated non-radiative recombination at much more practical fluences. Figure 3.9 (a) illustrates the carrier transport in the n = 3 perovskite thin film. The film contains grains with a variety of n-values (n = 2, 3). Similar structure was shown for the n = 5 perovskite film (Figure 3.9 (b)), which contains n = 2, 3,4 and 5 perovskite phases in significant proportions. As the bandgap of 2D perovskite is gradient modulated by the n-value, the unidirectional diffusion of carriers can be driven by the energy difference and emit at the lowest energy position. The scheme of energy funneling in shown in Figure 3.9 (c).

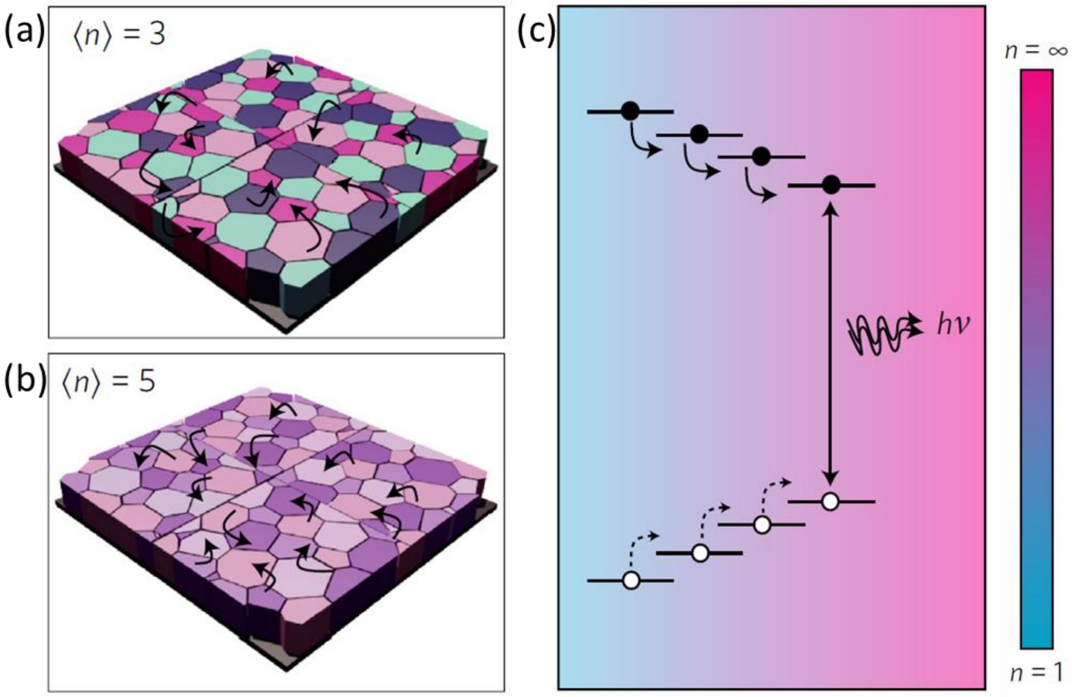

Figure 3.9 (a) The carrier transfer process in n = 3 perovskite. (b) Carrier transfer process in n = 5 perovskite. (c) Multi-phase perovskite materials $PEA_2MA_{n-1}Pb_nI_{3n+1}$ channel energy across an inhomogeneous energy landscape, concentrating carriers to smallest bandgap emitters. The arrows represent the carrier transfer process. [12]

The effective downward carrier funneling in gradient-bandgap structures can improve the intrinsic photophysical properties of perovskites, such as longer carrier diffusion, stronger light harvesting and higher photoluminescence quantum yield. The concept can be applied in photon energy delivery, emissions, LEDs and other optoelectronics.

3.3 Research questions of the thesis

Despite the good behavior, some questions remain for the carrier diffusion of perovskite materials. First, the long carrier diffusion length is one of the most critical properties for the remarkable performance of perovskite solar cells. A wide range of methods have been reported for determine the diffusion length of semiconductor materials. However, most of the techniques are not practical for 2D perovskite NPs and 3D thin perovskite flakes, as large scale of perovskite films or high PL efficiency are required in these techniques. Thus, a proper method for quantitatively characterize the charge carrier behavior of these perovskite NPs is of vital importance.

Second, the charge carrier funneling is quite efficient for the PL efficiency of gradient-bandgaps structure semiconductors. However, funneling structure in gradient bandgap perovskites is not well studied. Under light irradiation, PL shift in mixed-halide perovskites has been intensively observed, which is generally ascribed to phase segregation. This phase segregation phenomenon, as a kind of instability, is detrimental for its application. To date, the observations of phase segregation display much discrepancy, and the mechanism is still under debate. Particularly, in gradient bandgap mixed-halide perovskite, the detailed physical process of phase segregation has not been discussed.

Third, with the gradient halide ratio of Br/I in a single perovskite NP, the gradient-bandgap perovskites have a great potential for the application in the spatially tuning of fluorescence color. However, precise microscale color patterning is still a challenge. To incorporate such perovskite structure into integrated device, a new nanoscale fabrication method should be developed. By combining with the femtosecond direct laser writing (fs-DLW) fabrication technique, the anion-exchange reactions may occur at specific points of the gradient-halide perovskites, which will modulate the fluorescence color at the micrometer scale. Simultaneously, understanding of the ion exchange under nanofabrication in such structure is also crucial for its on-chip applications.

3.4 Spectroscopic techniques for charge carrier dynamics process

3.4.1 Methods for carrier lifetime and diffusion length measurements

The charge carrier processes has been widely investigated by several techniques. For instance, the TA technique for ultrafast process on the picosecond scale, and the cathodoluminescence method on the nanoscopic scale. Among these techniques, TRPL detect the carrier process on the microsecond scale, which is the scale for the lifetime of perovskite materials. Based on the repetitive time registration of single fluorescence photons under laser pulse, the fluorescence intensity decay and thus lifetime is obtained by this method. The typical TRPL experimental setup is illustrated on Chapter 3.4.2.

Various techniques and methods have been utilized for the study of carrier diffusion lengths. For instance, optical spectroscopic contactless methods like photoluminescence quenching (PLQ) and TA microscopy techniques, as well as electrical probes such as time-of-flight (TOF) technique, Hall effect technique and space-charge limited-current (SCLC) measurements are employed.

For the electrical techniques, an electrical field or magnetic field is added to the device. For example, following a voltage pulse, the transient current is monitored in TOF method. By identifying the transit time and the thickness carrier travelled, the carrier mobility is thus extracted. In Hall effect measurements, the carrier mobility is calculated according to the built-up Hall voltage induced by the deflection of charge carriers in magnetic fields. Meanwhile, the SCLC technique extracts the charge-carrier mobility from the Mott-Gurney law, after monitoring the current as a function of bias voltage.

As the optical spectroscopic techniques are contactless methods, it is more popular for the carrier diffusion length measurement of neat perovskite materials. In principle, these techniques can be classified into two mechanisms, absorption and fluorescence, both mechanisms can be divided into steady-state (with time integral) and time-resolved techniques.

Among the absorption techniques, a variety of spectroscopic techniques have been employed for the investigation of charge carrier dynamics processes, including the transient absorption and transient PL spectroscopies based on terahertz absorption, optical absorption, microwave conductivity and so on.

For instance, transient absorption (TA) spectroscopy is a well-established pump-probe technique, with time resolution down to femtosecond regime. This method measures the absorption changes in the excited sample by the laser pump, and the information comes without relying on the radiative efficiency of the sample.[49] Due to its ultrafast probe, the hot carrier dynamics can be investigated by a unique kinetic model.

Time-resolved terahertz absorption spectroscopy (TRTS) is an optical pump / THz probe technique on a sub-picosecond timescale. It selectively monitors photoinduced free charge carriers, as a THz wave with a photon energy in the 1–100 meV range can be responded by the low-energy excitations of photo-generated charges in terms of carrier generation, scattering and lattice vibrations.[7] The diffusion parameters of bulk film perovskites can also be extracted by the TRTS technique, however, the method depends on the Drude-like model, which is not suitable for the nanostructured perovskites.

By fabricating thin films with and without an electron/hole layer, PL quenching technique is possible to accurately determine the diffusion length and diffusion coefficient. After obtaining the PL decay of samples with the absence and presence of carrier quenching layers, these results can be analysed in a diffusion equation, and the diffusion length or both electrons and holes will be determined by changing the quenching layer.

3.4.2 Steady-state and time-resolved photoluminescence technique

For fluorescence techniques, the steady-state and time-resolved photoluminescence technique is a versatile and most common tool among these spectroscopic techniques. By recording the PL wavelengths and intensities, the steady-state PL helps with the analysis of material components and some optical characteristics. By recording the population of emitted photons as a function of time after the sample been excited by a pulsed light source, the TRPL results help with the analysis of carrier recombination and diffusion processes.

A localized steady-state PL and TRPL system is used in our experiment. In this measurement setup, a confocal microscope setup helps to locate and focus the excitation position on a small part of the sample. Under laser excitation, the fluorescence is collected by an objective and then analyzed by both PL and TRPL units. The PL unit investigates the spectrally selected components of the fluorescence while the TRPL measurement shows the PL decay as a function of time difference between excitation and emission. Figure 3.10 shows the schematic illustration of the localized PL and TRPL system setup in our experiments.

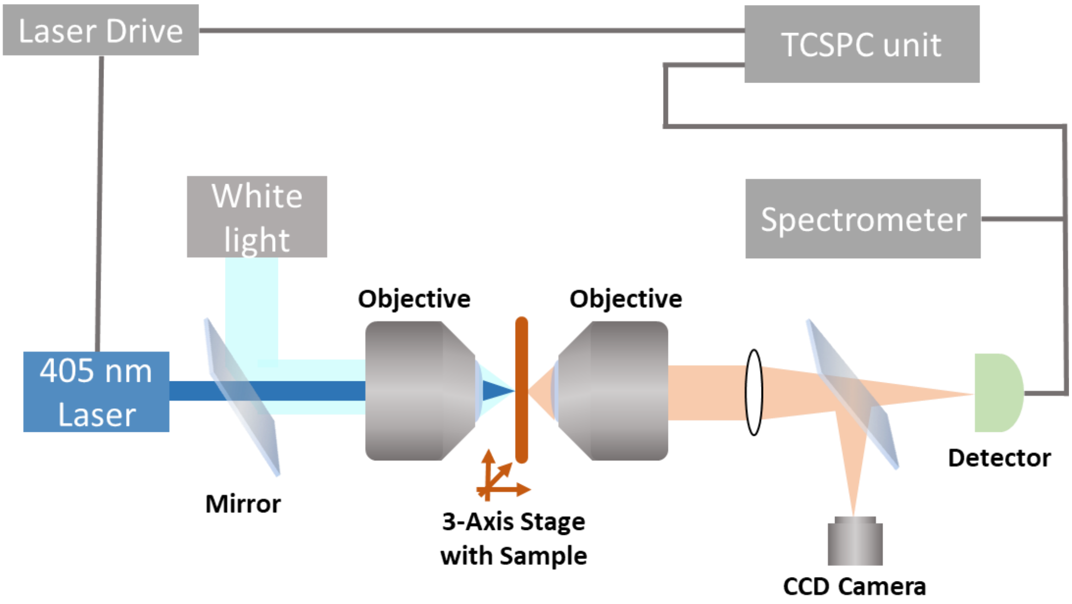

Figure 3.10 The schematic illustration of localized time-resolved and steady-state PL measurement setup.

In this setup, the sample is fixed on a 3-axis stage so that the sample location can be adjusted conveniently. The fluorescence is measured by a transmission configuration in which the laser is directed at the left side and the emission is collected from the right side of the sample. The 405 nm pulse laser is focused on the sample surface via an objective, and a neutral density filter is used to attenuate the laser intensity. Upon excitation, the sample will emit fluorescence at a longer wavelength than that of the excitation laser. Before collected by detectors, the emission is gathered by another objective and a focusing lens, and then passed through an optical long-pass filter to block out scattered excitation light. The two objectives are strictly aligned to ensure the transmitted PL is largely acquired. A bright-field microscopy technique is used to help locate the sample. The white light transmitted the sample, and the sample image is collected by a charged-coupled device (CCD). Under laser excitation, the sample fluorescence image can also be collected by the CCD after the laser excitation is blocked out, an example of the CCD image and fluorescence image of an $FAPbBr_3$ perovskite NP is shown in Figure 3.11 (a, b).

The steady-state PL is analyzed by a spectrometer. By breaking up the collected fluorescence, the spectrometer detects the fluorescence wavelengths and intensities, which is helpful to investigate the spectroscopic behavior of perovskites, for example, to identify or confirm halide components of mixed-halide perovskites by PL wavelengths. The PL result of the $FAPbBr_3$ perovskite NP is illustrated in Figure 3.11 (c).

The detection of photons in TRPL measurements is achieved by the time-correlated single photon counting (TCSPC) technique, which involves two repeated steps: First, the pulse laser is running on its internal clock and excite the sample repetitively. The trigger signal of each pulse is synchronized to the TCSPC unit directly by the power supply of the laser. Second, the emitted photon from the sample is collected and detected by a single photon avalanche diode (SPAD), and the time of the photon arrival is determined by the TCSPC unit as well. The time difference between excitation and emission is thus obtained for every detected photon like a stopwatch. With periodic excitation and emission, the stopwatch readings are collected over multiple cycles and the fluorescence decay profile can be reconstructed when sufficient counts have been collected. Figure 3.11 (d) shows the TRPL result of the $FAPbBr_3$ perovskite NP obtained by this experimental setup.

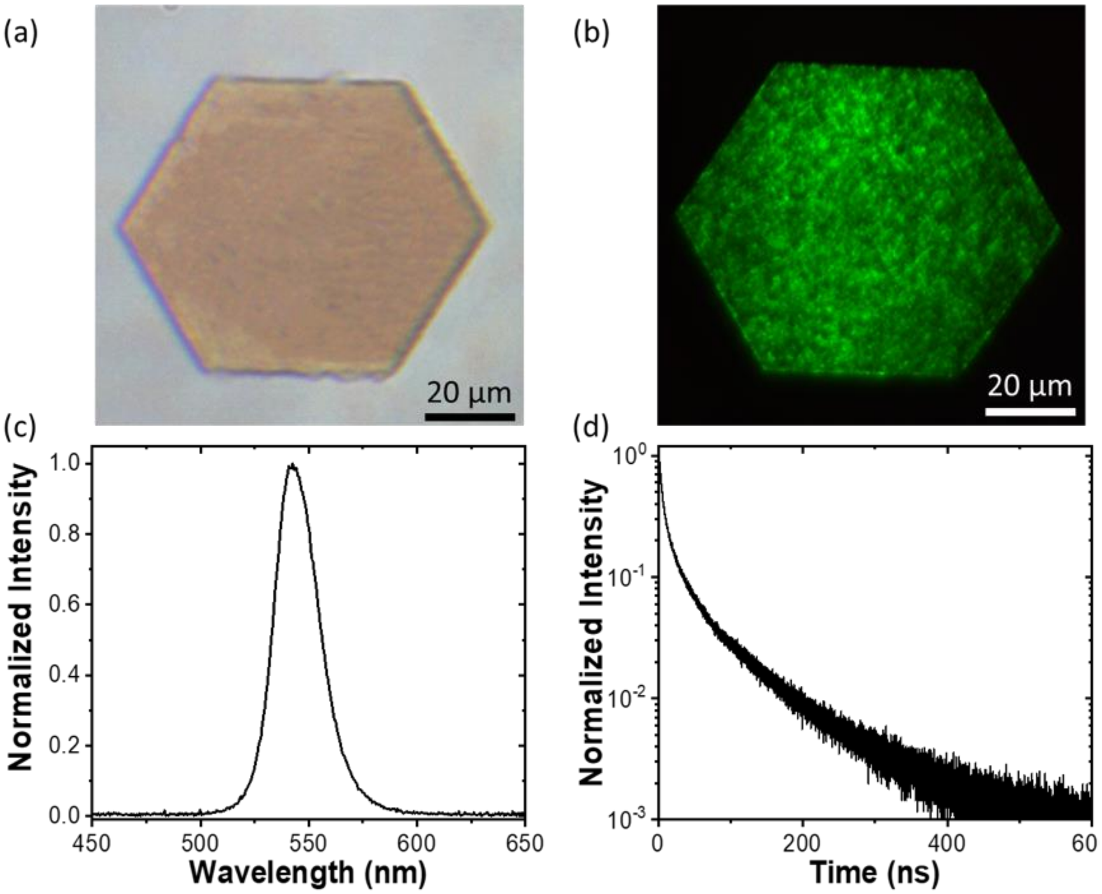

Figure 3.11 An example of the (a) CCD image, (b) fluorescence image, (c) normalized PL and (d) TRPL results of an $FAPbBr_3$ perovskite NP based on the experimental setup.

Moreover, PL and TRPL measurements for samples at macroscopic scales can be achieved by removing the two objectives in Figure 3.10. Instead of been focused on a small point, the laser pulses will excite on a larger area. Meanwhile, all the emission is collected, and the results will be the average PL properties of the sample.

Besides the system in our experiment, TRPL systems are also compatible with other components. For instance, by point-to-point scan, the single point excitation/single photon detection TCSPC method can generate an image for the whole sample, which is known as fluorescence lifetime imaging (FLIM) technique. The image is based on the contrast of individual fluorophore lifetime. The spatially distribution and local carrier dynamics of perovskite grains can be investigated.[72-73]

3.4.2 Femtosecond direct laser writing technique for on-chip fabrication

The direct fabrication of precise micropatterns on a single perovskite crystal is of great importance for its optical applications such as nanolasers, photonic chips, and multicolor displays. For instance, Dou et al. demonstrate spatially resolved multicolor $CsPbX_3$ (X = Cl, Br, I, or alloy of two halides) nanowire heterojunctions with a pixel size down to 500 nm with the photoluminescence tunable over the entire visible spectrum.[74] By combining the facile anion-exchange chemistry with nanofabrication techniques, the method make accurate control over the composition, band gap, energy level (band bending), and doping level show great potential in high-resolution multicolor displays beyond current state-of-the-art technology as well as high-density diode/transistor arrays.

Direct laser writing is a mask-free, inexpensive nanofabrication technique with high enough quality. It has emerged as a rapid, flexible fabrication of nanostructure in recent years. The experimental setup of a homemade fs-laser fabrication system is shown in Figure 3.12.[75] By controlling the fs-laser power, a designed amount of sample in the laser exposed regions can be removed and/or photochemical reactions can be induced, leading to the reduction of sample thickness, as well as the change of local physical properties. For example, Zheng et al. fabricated the microscale graphene oxide lenses by this one-step fs-DLW technique.[76] An unique and giant refractive index and absorption modulations of the sprayable graphene oxide thin film was achieved during the fs-DLW process. Combining with this nanofabrication technique, spatially resolved fine-tuning of the fluorescence color may achieve. Moreover, in a specifically designed mixed-halide perovskites in which the ratio of iodide-bromide changes along the depth and thus exhibits gradient bandgap along the depth, it is possibly to vertically modify the sample together with high resolution in plane, which allows to develop on-chip optical applications.

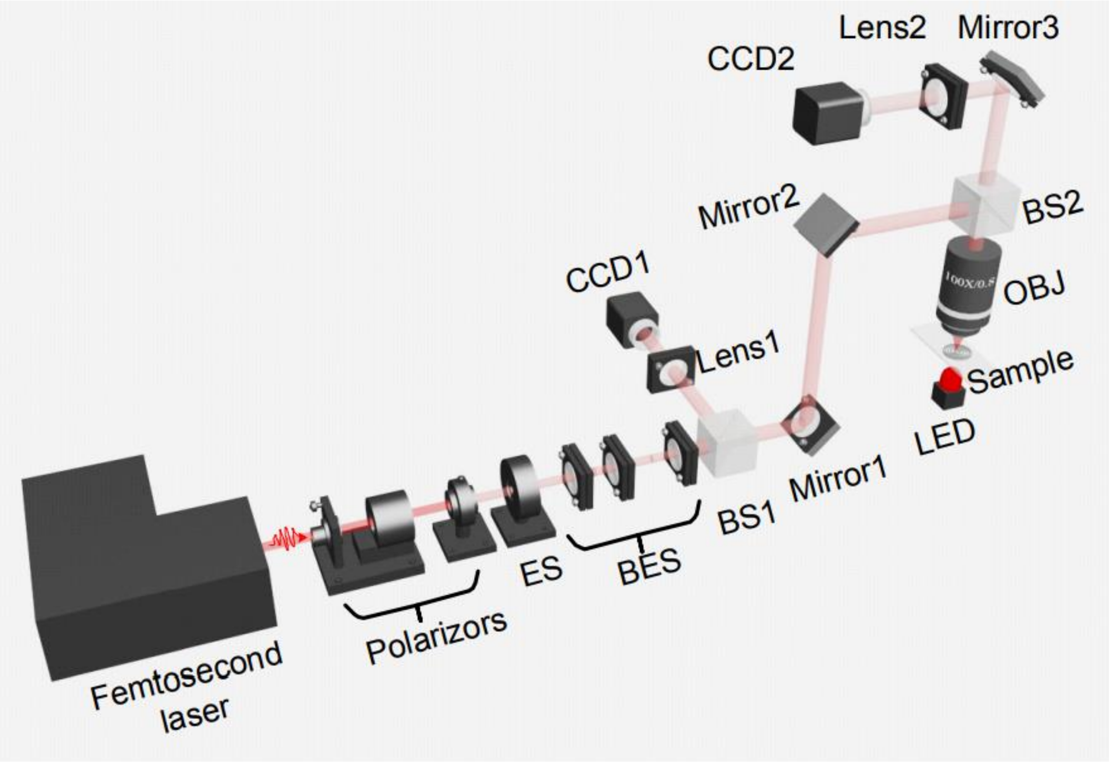

Figure 3.12 Experimental setup of the laser fabrication system. ES: electronic shutter; BES: beam expanding system; BS1 and BS2: beam splitter; LED: light-emitting diode; Sample: GO film; OBJ: objective; CCD1 and CCD2: charge coupled device.[75]

Chapter 4

Determining In-Plane Carrier Diffusion in Two-Dimensional Perovskite Using Local Time-Resolved Photoluminescence

The diffusion length of photogenerated carriers is a crucial parameter in semiconductors for optoelectronic applications. However, it is a challenging task to determine the diffusion length in layered nanoplatelets due to their anisotropic diffusion of photogenerated carriers and nanometer-thin thickness. Here, we demonstrate a novel method to determine the in-plane diffusion length of photogenerated carriers in layered nanoplatelets using local time-resolved photoluminescence. An in-plane carrier diffusion length of 1.82 μm is obtained for an exfoliated $(BA)_2PbI_4$ ($BA=CH_3(CH_2)_3NH_3$) perovskite nanoplatelet. This method is particularly useful for weak luminescent materials and the materials that are easily damaged by long-term laser beam because of the high detection sensitivity. This technique is extendable to other layered materials and therefore plays a valuable role in the development and optimization of 2D and 3D semiconductor materials and devices for photovoltaic and photonic applications.

4.1 Introduction

The family of two-dimensional (2D) materials has grown considerably since the first isolation of graphene. Their unique properties, which are very different from their bulk counterparts, offer a great flexibility in terms of their potential applications.[77] Organic-inorganic hybrid perovskites have attracted considerable research interest in recent years due to the enormous potential for highly efficient optoelectronic applications, such as solar cells[2, 29], light-emitting diodes (LEDs)[12, 78] and photodetectors (PDs)[15, 79-80]. With intrinsic higher photostability and chemical stability, two-dimensional (2D) Ruddlesden-Popper perovskites (RPPs) are promising candidates for various functional devices.[20, 77, 81-83] In such 2D RPP structures, natural multi-quantum-well (MQW) structures are formed as inorganic layers and intercalated with organic cations acting as spacers.[70] Due to the quantum confinement, the electron-hole interaction within the exciton is very strong, resulting in substantial oscillating strengths and large exciton binding energies.[71] What is more, only in-plane anisotropic carrier diffusions are allowed in these natural MQW structures.[84]

Diffusion length is a critical parameter for semiconductor materials and the optimization of their applications. Long diffusion length is considered as one of the most critical advantages of perovskites for its applications in solar cells.[69, 85] However, the diffusion length measurement of 2D thin perovskite samples is difficult, and the results are very controversial.[6] Proper methods for determining the diffusion length, both theoretically and experimentally, are of vital importance. Therefore, a wide range of techniques have been reported to date,[6-7] such as time-resolved microwave conductivity[86], space-charge limited current[8], Hall coefficient, and resistivity measurements[25], time-of-flight transients[29] and PL quenching[9]. Most of these techniques require a large-scale sample to enable the deposition of electrodes or obtain detectable spectroscopic signals, which are not practical for the measurement of 2D nanoplatelets (NPs), such as perovskite ultrathin flakes. Exciting progress using microscopic and spectroscopic techniques has been made recently. Tian et al. obtained carrier diffusion lengths of individual single-crystal nanowire and nanoplate on a confocal microscope by parking the excitation laser spot in a specific position and scanning the whole sample to emit photons.[68] Using femtosecond transient absorption microscopy, Huang, and co-workers[87] measured the carrier diffusion length in perovskite polycrystalline film. The limitation of these techniques is that the PL efficiency of the sample should be very high and/or the sample must be stable under high laser excitations to ensure enough photons are collected for good quality PL signal.

Here, a novel method using the time-resolved micro-PL technique is developed for robust measurement of the in-plane diffusion length in 2D RPP, not requiring specifically designed confocal scanning microscope or transient absorption microscopy. In this technique, the measurement can be conveniently achieved in thin NPs, and the edge trapping states of these NPs are used as natural quenching sources for determining the in-plane carrier diffusion from the laser excitation spot to sample edge. Different from the previous confocal microscope method,[24] the collecting spot is the same as the excitation spot, and lower excitation intensity is required for acquiring high quality signal. Therefore, this method can be applied to samples with relatively low PL efficiency. By modelling the PL kinetics of multiple excitation positions with gradually decreased distance to the edge of the NP, the diffusion length of 1.82μm is determined in a 2D perovskite thin NP exfoliated from a $(BA)_2PbI_4$ single crystal ($BA=CH_3(CH_2)_3NH_3$). This method can be extended to other 2D nanosheets, which is hugely useful in the development and optimization of 2D materials and their devices.

4.2 Experimental Section

Synthesis of 2D BA_2PbI_4 crystals: The synthesis of BA_2PbI_4 single crystals is based on the method by Stoumpos et al.[20] with some modifications. Lead acetate ($Pb(COO)_2$) powder (1.6 g) was dissolved in 5 mL of 57% w/w aqueous hydroiodic acid (HI) solution at room temperature under constant magnetic stirring, which formed a bright yellow solution. Meanwhile, in another bottle, n-$CH_3(CH_2)_3NH_2$ (0.9 mL) was slowly neutralized with 5 mL of HI 57% w/w in an ice bath. Then, the n-$CH_3(CH_2)_3NH_3I$ solution was dropwise added to the lead solution under 100°C and stirring, which initially produced a black precipitate, and subsequently dissolved under heating the combined solution to boiling. The stirring was then stopped, and the solution was left to cool to room temperature during which time orange plate-shaped crystals can be obtained. The precipitation was deemed to be complete after about 2 hours. The crystals were isolated by filtration and thoroughly dried under reduced pressure.

Synthesis of 3D $MAPbBr_3$ NPs: The $MAPbBr_3$ NPs were fabricated by the CVD method. First, 1 mg of $PbBr_2$ powder was dissolved in 1 mL of deionized water and heated at 90 °C to get the saturated $PbBr_2$ aqueous solution. Hexagonal $PbBr_2$ nanosheets were observed a few minutes after the solution was dropped into glass substrate. Second, the MABr powder was placed at the centre of a CVD furnace, while the substrates with PbI_2 nanosheets were mounted downstream of the apparatus. During the whole vapor conversion process, temperature was 140 °C, and pressure was ≈500 mTorr with a controlled Ar gas flow rate of 35 sccm. After around 2 h, $MAPbBr_3$ NPs were synthesized.

Optical spectroscopy: Steady-state PL spectra and PL decay trace were performed on a microscopic fluorimeter system. A 405 nm picosecond diode laser (pulse duration 50 ps) is used as excitation source. The perovskite NPs were excited through an objective of 80 x NA 0.75 at a repetition rate of 2.5 MHz. The laser beam is attenuated using a neutral density filter and the excitation fluence is 200 mW/cm^2. The emission was filtered through a 515 nm longpass filter. PL spectra were detected by a spectrometer (Ocean Optics, QE-Pro). TRPL were acquired by time correlated single photon counting (TCSPC, PicoHarp 300). The thickness of the sample was determined using an optical profiler (Bruker). All the measurements were conducted at room temperature.

4.3 The determination of carrier diffusion

4.3.1 The method design for the carrier diffusion determination

The 2D perovskite $(BA)_2PbI_4$ single crystal used in this study was synthesized by a modified Stoumpos' method[20] and stored in a nitrogen atmosphere (see the Experimental Section for details). The exfoliated NP was peeled off from the as-synthesized perovskite single crystal by the Scotch-tape mechanical cleavage technique[88] and attached to a glass substrate. The transmission electron microscopic (TEM) image of the exfoliated crystal can be found in Figure S4.1 (a)[57] in Supporting Information.

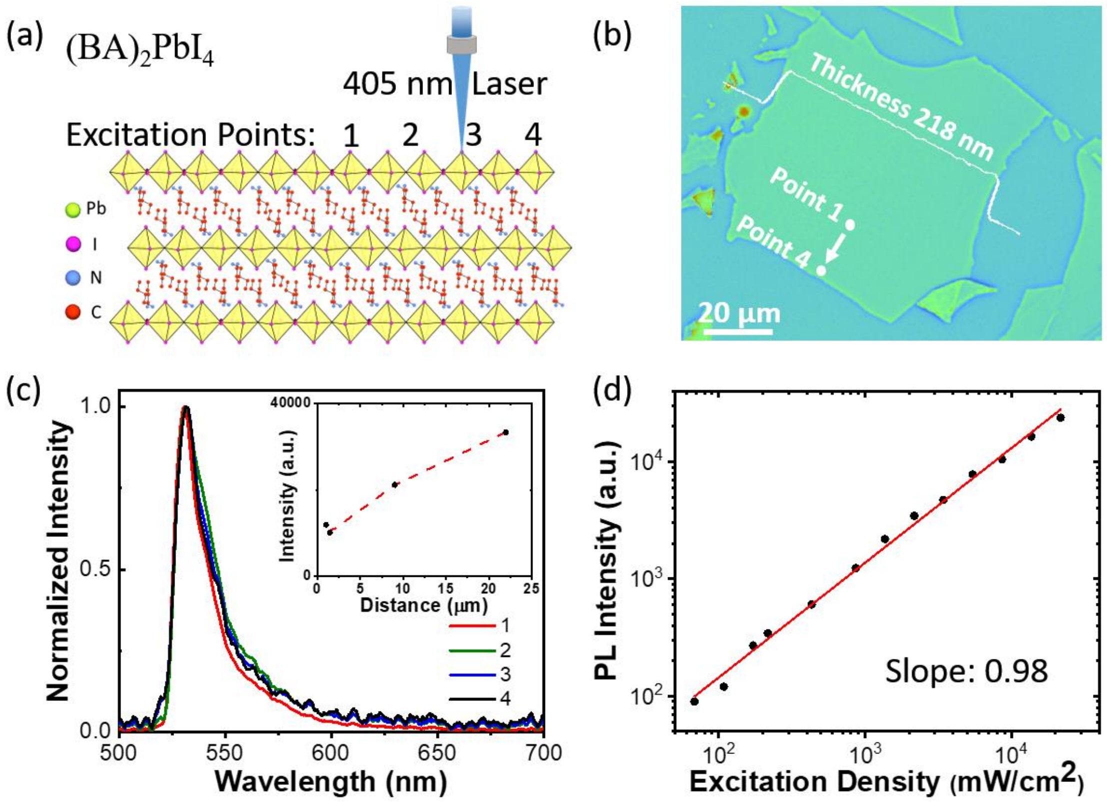

Figure 4.1 (a) Layered structure of $(BA)_2PbI_4$, and the scheme of laser excitation points. (b) Optical Image of the exfoliated $(BA)_2PbI_4$ NP, and locations of excitation points. The height profiles indicate the thickness of 218 nm. (c) Normalized PL spectra at various points under 405 nm laser excitation. The inset is the PL intensity of the excitation points as a function of the distance to the edge. (d) Excitation power density versus integrated PL intensity for Point 1 (black dots) and the linear fitting in dual-logarithmic coordinate (red line).

Local steady-state PL spectra and time-resolved PL decay were performed on the exfoliated $(BA)_2PbI_4$ NP over a range of distances to the NP edge. The scheme of the layered structure 2D perovskite is shown in Figure 4.1 (a). Photogenerated carriers will diffuse along the inorganic layers. Without further processing or passivation, edge-trapping states are available at the edges, as the 2D expansion of perovskite layer terminates at the NP edges.[89-92] The edge trapping state acts as a quenching source for the photogenerated carriers when the excitation spot is close to the edge, resulting in an extra direction. Different laser excitation positions are designed from the center to the edge. The first point chosen is at the NP center (far from the edge where edges effects are negligible, e.g., about 20 µm away depending on the diffusion coefficient). Remaining three points are selected with a gradually decreased distance to the edge (for example, 9.03 µm, 1.44 µm away from the edge). The last point should be close to the edge (e.g., 1.01 µm) where edge effect plays a vital role in trapping/draining photogenerated charge carriers. These designed laser excitation positions (Point 1 to Point 4) correspond to the positions in the optical image of $(BA)_2PbI_4$ NP (Figure 4.1 (b)). The thickness of the NP is 218 nm, measured by a 3D profiler, and the absorption spectrum is shown in Figure S4.1 (b).

Normalized PL spectra of different points at an excitation of 405 nm laser are presented in Figure 4.1 (c), with the same PL peak at 530 nm. There are reports in the literature that PL of thin $(BA)_2PbI_4$ films shows a symmetric peak centered at 519 nm when no other optical effects, e.g., photon reabsorption, is presented.[93] In comparison, the PL spectrum of the $(BA)_2PbI_4$ films red-shifted in our case, which can be ascribed to the disorder of the crystal with thickness increasing.[57, 94-95] PL intensities of different points are compared under the identical excitation intensity (Figure 4.1 (c) inset). The PL intensity decreases from the NP centre to the edge (point 1→3) due to the gradually increased edge quenching effect. When the excitation point is very close to the edge (point 4), PL intensity increases, which is similar to other studies.[96-97] Waveguide effect can be an essential factor in this experiment. For the first three points away from the edges, a large portion of the interior PL emission cannot be extracted due to the large refractive index.[57] However, at point 4, part of the emission can be extracted from the edge in addition to that from the upper surface, taking into account the high numerical aperture (NA 0.75) of the collection objective.

To confirm the carrier recombination mechanism, PL intensity was measured as a function of excitation fluence (Figure 4.1 (d) for point 1). In a double-logarithmic scale, the linearity with a slope of 0.98 suggests excitons dominated the recombination process[98]. In 2D layered-structure perovskites, the thickness of the metal halide layer decreases to the scale of de Broglie wavelength[99], resulting in the enhanced quantum confinement on charge carrier behavior, similar to that in the typical multiple quantum wells. The significant mismatch in dielectric constants between inorganic and organic layers will result in high exciton binding energy (~300 meV) and anisotropic charge transport.[57, 100] In such a strong confined system of dielectric and quantum, excitons are expected to be the dominant carriers.[101-103] Similar results were shown in the other 3 detected points.

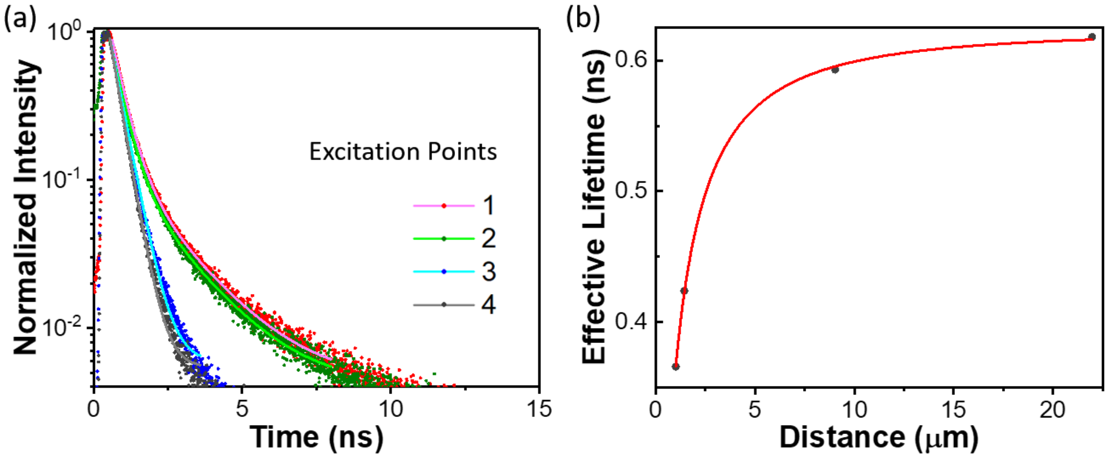

Figure 4.2. (a) PL decay (dots) and bi-exponential fitting (lines) for various excitation points. (b) Effective lifetime (black dots) plotted vs. the distance. The data were fitted by equation 2 (red line), Edge recombination velocity, and diffusion coefficient values are acquired.

4.3.2 Determining in-plane carrier diffusion in 2D perovskite

PL decay traces are measured by time-correlated single-photon counting (TCSPC) technique (Figure 4.2 (a)). To confirm the uniformity of the sample, PL decay curves were firstly measured at a few central points (far from the edge with a distance larger than 20 μm). For these points, the distance to the edge is initially expected to be much larger than the diffusion length, according to the reported diffusion length of a 3D perovskite single crystal (6.0 μm for $MAPbBr_3$[68]). The very similar PL decays indicate the excellent uniformity of the sample. Secondly, PL decay traces were measured at point 1→4 under an identical condition. With the distance to the edge decreasing, PL decay curves exhibit a faster decay. This can be ascribed to an increased contribution of edge trapping.[104]

Upon laser excitation, photons are absorbed by the perovskite in the spot, and photogenerated excitons are quickly formed. The excitons will relax radiatively via emitting photons, or non-radiatively through defect trapping. When the distance to the edge is significantly larger than the diffusion length (in the case of point 1 with distance > 20 μm), the role of the edge trapping is negligible.[52, 56] In this case, the dominant relaxation mechanism includes exciton recombination and Shockley−Read−Hall recombination.[56] When the excitation spot is close to the edge, excitons can diffuse toward the edge and be trapped via nonradiative recombination. As the distance decreases, the possibility of excitons being trapped by the edge has increased. We notice that photon recycle can result in the change of PL decay.[57] Taking the details of the experiment into account in which the sample has the uniform thickness and the identical experimental conditions are applied for each point, the influence by photon recycling is expected to be the same for measurement for all the selected points. Therefore, edge state quenching is the dominant mechanism for the lifetime variation observed in different points/locations, and photon recycle would not apparently impact the conclusion in these measurements.

To obtain quantitative insight into the carrier diffusion and edge trapping, the PL decay curves are fitted by a two exponential decay function: $I(t) = A_1 \exp\left(-\frac{t}{\tau_1}\right) + A_2 \exp\left(-\frac{t}{\tau_2}\right)$. [52, 105] PL decay curves are nicely fitted by this function and shown in Figure 4.2 (a). All fitting parameters are tabulated in Table S4.1, and the effective lifetime is calculated by $\tau_{eff} = \frac{A_1\tau_1 + A_2\tau_2}{A_1 + A_2}$ for each point.[106] When approaching the edge, the excitons have increased possibility to be trapped by edge states. This additional relaxation channel can result in a faster PL decay. Their effective relaxation rate (τ_{eff}) originates from the interior relaxation rate (τ_{in}) and the edge trapping rate (τ_{edge}) with the following relationship: [107]

$$\frac{1}{\tau_{eff}} = \frac{1}{\tau_{in}} + \frac{1}{\tau_{edge}} \qquad (4\text{-}1)$$

where τ_{in} includes radiative recombination, nonradiative recombination and surface defects trapping by the barriers (surface). Figure 4.2 (b) shows the effective lifetime as a function of the distance to the edge.

The diffusion lengths of perovskite materials have been previously reported in the range of hundreds of nanometers to a few micrometers.[52, 69, 85] For point 1 in our experiment, the distance to the edge (21.96 μm) is much larger than the reported diffusion length. Thus, excitons are unlikely to diffuse to the edge, and carrier trapping by the edge is negligible ($\tau_{eff} \approx \tau_{in}$). This is confirmed by the very similar PL decay curves at the different spots with a large distance to the edge (>20 μm).

When the excitation point is approaching the edge, excitons have increased possibility to diffuse to the edge and be trapped. The τ_{edge} can be approximately given by[52, 107-108]

$$\tau_{\text{edge}} \cong \frac{W}{ERV} + \frac{4}{D}\left(\frac{W}{\pi}\right)^2 \qquad (4\text{-}2)$$

where W is the distance between the excitation spot to the edge, D is the in-plane diffusion coefficient of the excess excitons, and ERV is the edge recombination velocity.

Combining equations (4-1) and 4-(2), the relationship between the effective lifetime τ_{eff} and the distance W can be obtained by:

$$\tau_{eff} = \tau_{in} \cdot [1 - \frac{\tau_{in}}{\frac{W}{ERV} + \frac{4}{D}\left(\frac{W}{\pi}\right)^2 + \tau_{in}}] \qquad (4\text{-}3)$$

The effective lifetime as a function of the distance can be well fitted by equation 4-3 (Figure 4.2 (b), red line), and parameters of D and ERV are acquired: $D = 53.6$ cm^2/s and $ERV = 1.24\times10^5$ cm/s. Then, the in-plane diffusion length is calculated by $L = \sqrt{D\tau_{eff}}$,[85] $L = 1.82$ μm. Herz et al. estimated that the diffusion length of 2D perovskites can reach a maximum of 2.5 μm according to the mobility[14] although others consider the diffusion length should be below 100 nm referring to the organic semiconductors with similar exciton binding energy because the excitonic effect tends to enhance charge carrier recombination and curtail carrier diffusion.[109]

The diffusion coefficient/length acquired by this method is larger than other works, calculated diffusion lengths of 2.5 μm (mobility 10 cm^{2}V^{-1}s^{-1}, by THz probe)[71] and 0.16 μm (D = 0.06 cm^2/s, by femtosecond TA microscopy).[110] Two possible reasons should be taken into account: (1) the diffusion in our work is actually quasi-one dimensional (directional) due to the quenching of the edge trapping, which means that larger carrier density gradient can form due to large edge/surface recombination velocity, and the reported diffusion length in one-dimensional nanowire is generally large, e.g. average diffusion length of 14.0 ± 5.1 μm for $CH_3NH_3PbI_3$ and 6.0 ± 1.6 μm for $CH_3NH_3PbBr_3$;[68] (2) Because of the high detection sensitivity of the same-position excitation-detection TCSPC set-up, significantly larger impacted radium (up to 4-5 μm) is observed. In contrast, the impacted radium is usually less than 1μm in other works. For example, in TA microscopy method, where the incident laser is fixed on one point and the surrounded TA signal is acquired by scanning the probe, a short diffusion length of 0.16 μm was obtained for isotropic in-plane diffusion in 2D perovskite.[110] The large impacted radium is approximately matched with the large diffusion length.

To understand the role of the thickness of 2D perovskite on carrier recombination dynamics, an exfoliated $(BA)_2PbI_4$ NP with a thickness of 2305 nm was investigated, as shown in Figure S4.2 (a). Four points were chosen from the center to the edge to perform the measurement. It is reasonable that the PL spectrum (Figure S4.2 (b)) is the same as that of the thin NP because they were exfoliated from the same perovskite crystal. PL decay curves were measured under the same condition (Figure S4.2 (c)). All these curves can be well fitted by the same bi-exponential function. The fitting parameters and effective lifetimes are summarized in Table S4.2. Like the thin NP, the lifetime of thick NP decreases upon approaching the edge. Fitted by equation 4-3, the in-plane diffusion coefficient D = 47.8 cm^2/s, edge recombination velocity ERV = 1.13×10^5 cm/s and diffusion length L = 1.83 μm are extracted. These 2D perovskite materials with two different thicknesses ~200 nm and 2000 nm can roughly represent the range from the nanoscale to macroscale, while the resulted diffusion parameters are similar in both cases. These results illustrate that the thickness of $(BA)_2PbI_4$ NP has a limited impact on its diffusion length, which is not surprising as excitons in 2D perovskites are expected to be tightly confined in the inorganic layers. This is considered to be a general case in the 2D perovskites with n>1, as long as that the quantum-well like in-plane confinement is valid in these 2D perovskites because of the confinement of the organic spacers.

One might note that some 2D RPPs with n>1 have intricate energy band structure and photocarrier dynamics, therefore yielding not only excitons but also edge-state emissions[42] and affecting the applicability of this model. Essentially, the carrier/exciton population on the conduction band is detected through probing the PL decay at corresponding wavelength. A suitable bandpass filter was used for selecting the PL emission and filtering the other wavelength emission, since edge state emission is found at the lower energy/longer wavelength compared to exciton-state PL. In our model, the edge trapping effect is considered to generate a quenching source of photo-generated carriers/excitons, which will direct the excited carriers/excitons to diffuse directionally toward the edge. Therefore, the detected PL decay will not be affected by the edge-state emission in our experiments. It is important to selectively detect the decay of the band-to-band emission if the sample has intricate energy band structure. Therefore, this method also works for 2D RP perovskites with n>1.

4.3.3 Determining carrier diffusion in 3D perovskite

This method can also be used in 3D thin perovskite NPs, providing a simple technique for experimental measurement of diffusion coefficient (diffusion length) and edge recombination velocity. A $MAPbBr_3$ NP (205 nm thickness) was used as an example. The NP was fabricated by a chemical vapor deposition (CVD) method,[52, 111] and details are provided in the Experimental Section. When the distance between the excitation spot and the edge decreases, the photogenerated carriers have an increased possibility to diffuse and be trapped by the edge. This will result in the change of PL decay. Schematically shown in Figure 4.3 (a), four points are selected from the NP centre to the edge. The optical image of the perovskite NP and four excitation points are shown in the inset of Figure 4.3 (b). The absorption spectrum is shown in Figure S4.3 (a).

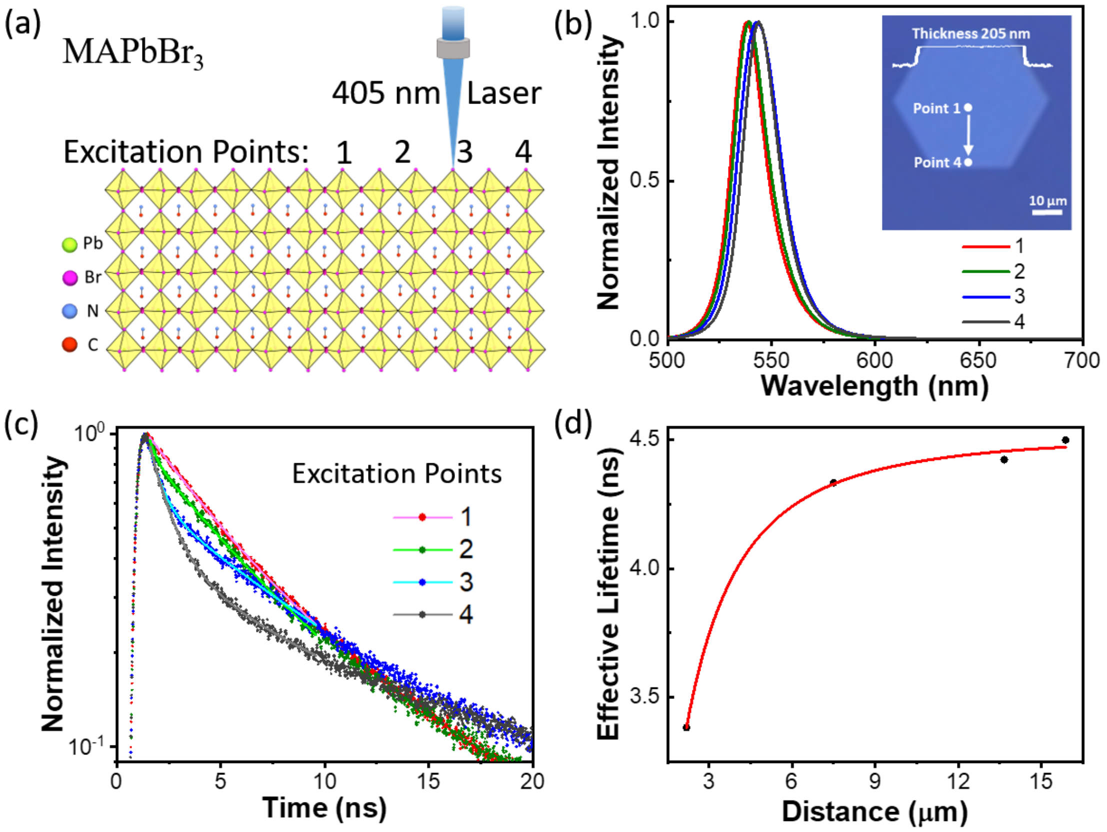

Figure 4.3 (a) $MAPbBr_3$ cubic structure and exciting points located from the center to the edge. (b) Normalized PL spectra of different points. The inset is the optical image, locations of excitation points, and the thickness (205 nm) of the $MAPbBr_3$ NP. (c) Experimental PL decay (dots) and bi-exponential fitting (lines). (d) Extracted effective lifetimes (black dots) and fitting (red line) by equation 4-3, plotted vs. the distance.

Figure 4.3 (b) shows the PL spectra of these points. A slight wavelength shift was observed, from PL peak of 538 nm (Point 1) to 544 nm (Point 4), suggesting the presence of defect states or shallow trapping levels at the edge.[73, 112] The PL intensity as a function of distance for the 3D crystal is shown in Figure S4.3 (b). The tendency is not the same as that of 2D perovskite. This is expected to be a complicated process in which PL emission generation, carrier diffusion, photon propagation, and photon recycle occur in the interior region of the sample (refractive index around 1.4). The emitted photons partly refract/escape out and are collected by the objective. The edge has a quenching effect and results in a decrease of PL intensity. The waveguide effect of the platelet sample results in an increase of PL intensity in the edge, but the effect also depends on the edge shape. Therefore, it is difficult to accurately estimate the contribution of each component. We consider that the waveguide effect plays a dominant role in the 3D sample while the quenching effect dominates in the 2D sample. Therefore, PL intensity is not used for accounting for the quenching effect of the edge state. Besides, the 3D NP shows a slope of 1.9 in a double-logarithmic scale of steady-state PL (Figure S4.3 (c)), unsurprisingly confirming that the bimolecular recombination of free electrons and holes dominates the recombination process.[52, 56]

Therefore, PL decay curves were measured for various points using identical excitation intensity, shown in Figure 4.3 (c). As distance decreases, a fast-decay component appears and keeps enhancing in the PL decay curve, indicating that more carriers can diffuse to the edge, which highlights the contribution of edge trapping. By performing bi-exponential fitting, the effective lifetimes were obtained (Table S4.3). By fitting the effective lifetime using equation 4-3, D = 2.9 cm^2/s and ERV = 3.1×10^4 cm/s are extracted. The diffusion length of L = 1.16 μm is then obtained. It should be noticed that the edge trapping does not selectively quench electrons or holes in this case. Therefore, this diffusion length is for both electron and hole, along the in-plane direction. Moreover, these measured results are within the range of reported values measured in similar MAPbBr$_3$ NPs,[68] rationalizing the measurement and calculation for determining the diffusion coefficient (length), and edge recombination velocity.

4.3.4 Advantages and application of the methods

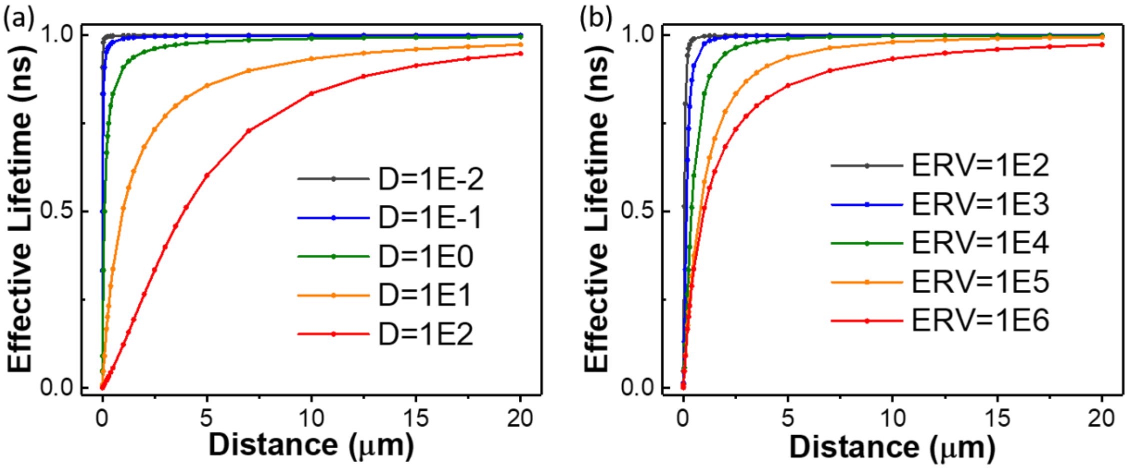

Figure 4.4 Effective lifetimes are calculated and plotted as a function of the distance between the excitation spot and the edge for various edge recombination rates (*ERV*) and diffusion coefficient (*D*). The lifetime τ_{in} was set to 1 ns for demonstration. (a) Various *D* at *ERV*=10^5 cm/s; (b) Various *ERV* at *D* = 10^2 cm^2/s.

The precision and suitability of the method can be further explored. The typical range of diffusion coefficient in semiconductors is 10^{-2}~10^2 cm^2/s.[113-115] For a non-passivated surface (interface or edge) in similar semiconductors, the recombination velocity is usually in the range of 10^2~10^6 cm/s.[116-118] The effective lifetimes as a function of the distance to the edge are calculated according to equation 4-3 and shown in Figure 4.4. The interior lifetime (τ_{in}) is normalized to 1 ns for demonstration. It is reasonable that the edge-impacted distance is sensitive to the diffusion coefficient, and therefore the measured spots should match correctly (Figure 4.4 (a)). For a low *D* range (10^{-2} to 10^{-1} cm^2/s), the distance is smaller than one micrometer. This indicates the laser spot size is an important factor, which is constrained by the optical diffractive limitation. For a precise measurement, a large NA objective and a small laser beam size should be used. At present, the spot radius of 0.33 μm is approximately estimated by $0.61 * \frac{\lambda}{\mathrm{NA}}$ (405 nm laser is focused by an objective with NA = 0.75).

In our method, a directional diffusion of the photogenerated carrier/exciton is produced due to the presence of high density of edge defects, which acts as a natural quenching source. As shown in Figure 4.4 (b), a low edge recombination velocity (*ERV*< 10^2) will result in a decrease of the directional diffusion. Consequently, the variation of the lifetimes and the impacted distance will decrease, results in a decreased measurement precision. In this case, an electron or hole transport layer can be deposited as a quenching source to replace the natural quenching source. Therefore, this technique also provides a possible extension in which electron diffusion length or hole diffusion length can be selectively measured by depositing electron transport or hole transport layer on the edge surface.

Moreover, this method of measuring in-plane diffusion length is relatively simple and easily approached as it can be performed in conventional micro-TRPL setup without critical requirements for sample preparation and imaging precision.

Another advantage is that the excitation and detection are in the same point and very low excitation intensity is required for acquiring high quality signal. Compared to the techniques based on the fixed-point excitation and detection in surround points, which requires much high excitation for acquiring same quality PL signal, this method is particularly useful for weak luminescent materials and materials that are easily damaged by long-term laser beam.

In addition, the deviation of the parameters of measurement does not depend on any single point. Instead, it averages multiple points so that higher precision is expected compared to any other single measurement.

4.4 Conclusions

We have demonstrated a novel method for determining carrier in-plane diffusion length in 2D layered and thin NPs, using localized time-resolved PL spectroscopy. In a typical 2D perovskite $(BA)_2PbI_4$ single crystal, diffusion coefficient (53.6 cm^2/s) and diffusion length (1.82 μm) of the $(BA)_2PbI_4$ single crystals are determined. The method is also applied to a 3D perovskite NP, and the carrier diffusion length of 1.16 μm is determined. This technique can also apply in 2D and 3D thin films and low luminescent samples. Moreover, this simple method can be further conveniently extended to, for example, the selective measurement of the electron or hole diffusion length by depositing electron or hole transport layer on the sample edge.

4.5 Supporting information

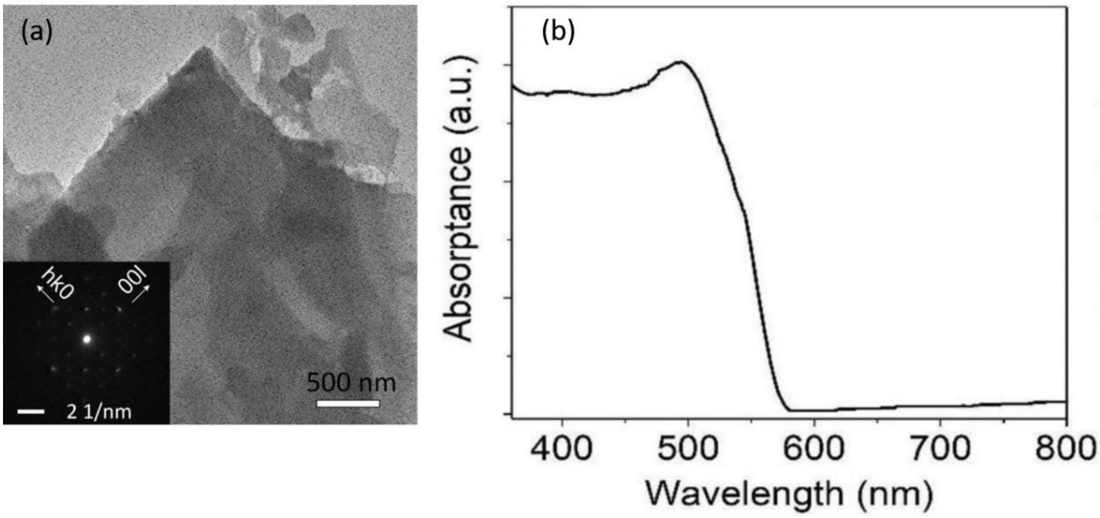

Figure S4.1 (a) TEM image of a thin 2D $(BA)_2PbI_4$ nanoplatelet. Inset: Electron diffraction pattern. (b) Absorption spectrum of a 2D perovskite nanoplatelet.

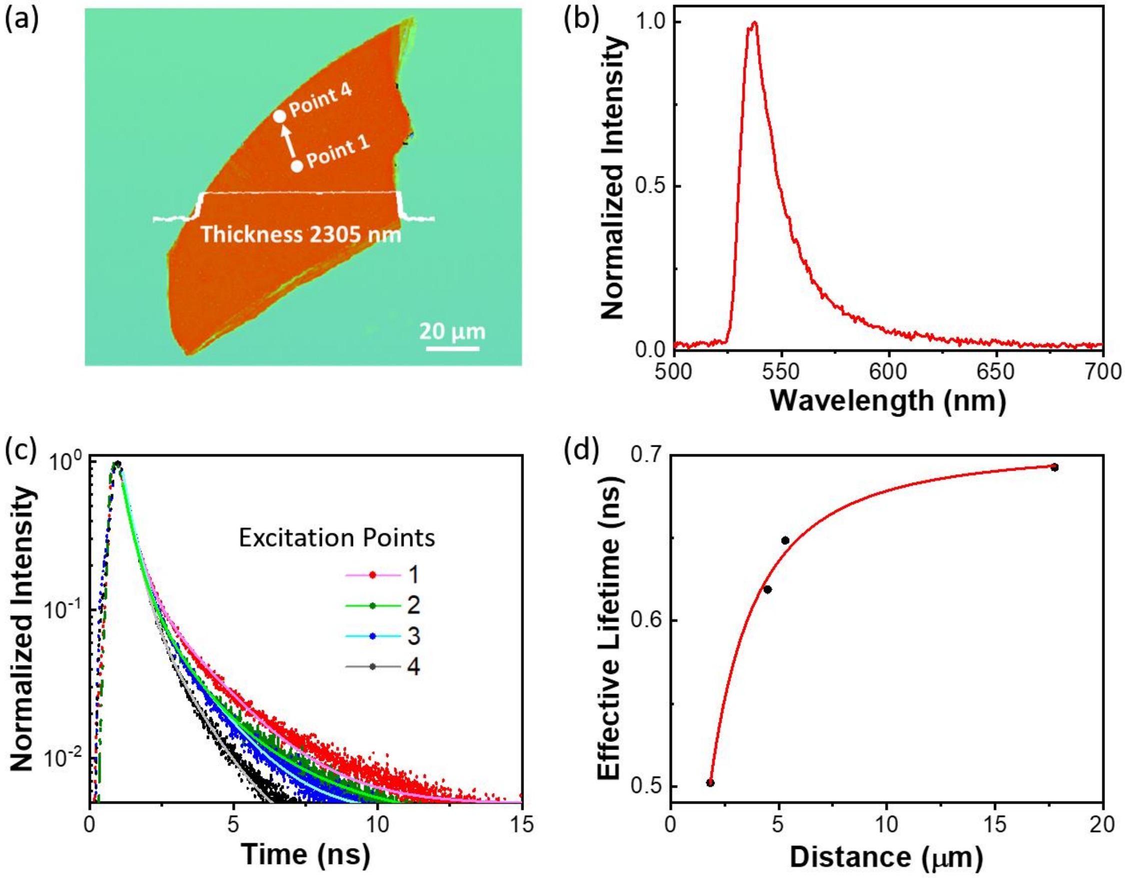

Figure S4.2. (a) Optical Image of the thick 2D perovskite NP, and locations of the excitation points. The height profiles indicate the thickness of 218 nm. (b) Normalized PL spectra of Point 1 under 405 nm laser excitation. (c) (a) PL decay (dots) and bi-exponential fitting (lines) for various excitation points. (d) Efficient lifetime (black dots) plotted vs. the distance. The data was fitted by equation 4-2 (red line).

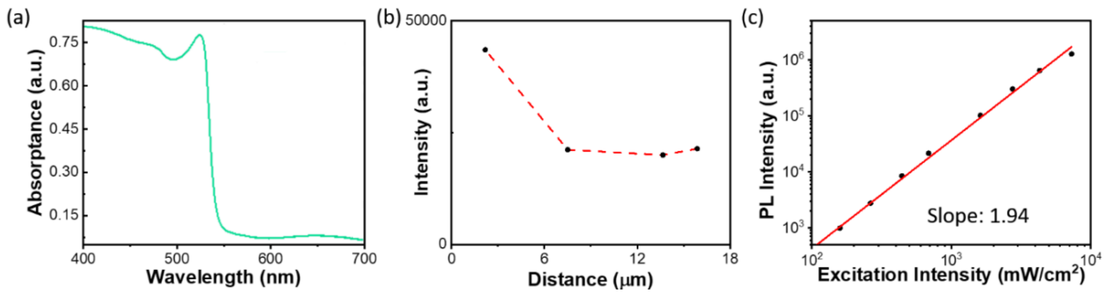

Figure S4.3. (a) Absorption spectrum of a 3D $MAPbBr_3$ Nanoplatelet. (b) PL intensity of the 3D NP as a function of the excitation distance to the edge. (c) Light excitation intensity dependence of the integrated PL for Point 1 of 3D perovskite (black dots) and the fit to the data (red line).

	Distance (μm)	A_1	τ_1 (ns)	A_2	τ_2 (ns)	τ_{eff} (ns)
Point 1	21.96	0.936	0.449	0.095	2.270	0.618
Point 2	9.03	0.924	0.434	0.098	2.095	0.593
Point 3	1.44	0.503	0.424	0.049	0.424	0.424
Point 4	1.01	0.530	0.366	0.037	0.366	0.366

Table S4.1 PL decay fitting parameters and effective lifetimes for different points in thin 2D perovskite using bi-exponential decay function.

	Distance (μm)	A_1	τ_1 (ns)	A_2	τ_2 (ns)	τ_{eff} (ns)
Point 1	17.76	0.701	0.392	0.174	1.939	0.693
Point 2	5.31	0.674	0.401	0.127	1.928	0.649
Point 3	4.49	0.631	0.354	0.164	1.636	0.618
Point 4	1.84	0.766	0.344	0.162	1.251	0.502

Table S4.2 PL decay fitting parameters and effective lifetimes for different points in thick 2D perovskite using bi-exponential decay function.

	Distance (μm)	A_1	τ_1 (ns)	A_2	τ_2 (ns)	τ_{eff} (ns)
Point 1	15.88	0.201	4.5	0.672	4.5	4.5
Point 2	13.66	0.111	0.337	0.77	5.013	4.424
Point 3	7.5	0.298	0.572	0.522	6.477	4.334
Point 4	2.18	0.504	0.993	0.391	7.149	3.382

Table. S4.3 PL decay fitting parameters and effective lifetimes of different points in 3D perovskite using bi-exponential decay function.

The work in this chapter has been published in the journal article: Zhou, C.; Chen, W.; Yang, S.; Ou, Q.; Gan, Z.; Bao, Q.; Jia, B.; Wen, X., Determining In-Plane Carrier Diffusion in Two-Dimensional Perovskite Using Local Time-Resolved Photoluminescence. *ACS Applied Materials & Interfaces* **2020**.[119]

Chapter 5

Illumination-Induced Halide Segregation in Gradient Bandgap Mixed-Halide Perovskite Nanoplatelets

Efficient energy funneling has exhibited great contribution to the high performance of perovskite-based optoelectronic devices. Here, formamidinium (FA^+, $HC(NH_2)_2^+$) lead mixed-halide nanoplatelets ($FAPb(Br_xI_{1-x})_3$) with gradient bandgap are fabricated using chemical vapor deposition followed with bromide–iodide substitution by exposure to FABr vapor. The as-fabricated perovskite nanoplatelets exhibit pure bromide phase in the thin nanoplatelet (tens of nanometers) and a gradual bromide–iodide composite, thus with gradient bandgap (2.29–1.56 eV), in the thick nanoplatelet (more than hundreds of nanometers). Accordingly, photoluminescence (PL) spectra are observed at 540, 560/610, and 735/790 nm, respectively. In such gradient bandgap structures, photogenerated carriers can effectively transfer and emit in the low bandgap region by energy funneling. With illumination, the PL spectrum of Br-rich phase exhibits blueshift and therefore 610 nm band disappears. In contrast, redshift is observed in I-rich phase due to the decrease of 735 nm band while an increase of 790 nm band. It is demonstrated that irreversible and stable phases are formed with illumination in both Br-rich and I-rich nanoplatelets. This investigation develops a method to fabricate gradient bandgap perovskites with designed energy funneling, and also provides significant insight into the halide segregation in such special perovskites, which greatly benefits their future optoelectronic applications.

5.1 Introduction

Organic–inorganic hybrid perovskites have attracted considerable research interest in recent years due to the enormous potential for highly efficient optoelectronic applications such as solar cells, light-emitting diodes (LEDs), and photodetectors (PDs).[13, 41, 78, 120] The power conversion efficiency (PCE) of perovskite-based solar cells has already exceeded 22%[121] since the first reports of perovskite solar cells in 2009.[2] The excellent performance has been attributed to their unique properties including long carrier diffusion lengths,[25] high optical absorption coefficients,[122] and high defect tolerance.[123] More recently, mixed-halide and mixed-cation perovskites have been demonstrated with high thermal and humidity stability[27, 122] as well as the ability of continuously tuning the bandgap, which are critically important for their practical applications and commercialization.[124] By increasing the portion of iodide ions, the bandgap of mixed-halide perovskite decreases, leading to the redshift of photoluminescence (PL) spectra. [28] It has been shown that the bandgap can be tuned over the range of 1.6–2.3 eV by changing the ratio between Br and I or Cl and I in mixed-halide perovskites,[125] which extends their optoelectronic applications such as tandem solar cells.[29, 126] In special halide-gradient perovskite materials, photogenerated carriers can transfer effectively from high-bandgap region to low-bandgap region, which can achieve highly efficient energy funneling.[11] For example, Tian et al. reported long-distance charge carrier funneling over a few micrometers in bromide-gradient mixed-halide perovskite single-crystalline nanowires.[11] A bright and efficient near infrared LED using solution-processed perovskite energy funnels was also reported.[12]

Numerous efforts have been made on bandgap engineering of perovskite layers by replacing the metal cations and/or varying the composition of halide ions, because of the potentially enhanced electron–hole collection efficiency and thus improved efficiency in perovskite-based tandem solar cells or LEDs.[10, 127] Despite these improvements of photovoltaic performance, mixed-halide perovskites exhibit unwanted phase segregation under light irradiation or electric field exposure, which is detrimental for applications.[29, 31, 64, 128-130] It was reported that the formamidinium (FA^+, $HC(NH_2)_2^+$) cation mixed-halide perovskite $FAPb(Br_{0.67}I_{0.33})_3$ film exhibits significant

PL redshift from 620 to 785 nm, accompanied with a small phase appearing at around 540 nm under a continuous illumination.[125] Moreover, spectrally resolved electroluminescence as a function of time under constant current injection conditions is also observed.[131] Although PL shift in mixed-halide perovskites has been intensively observed, and is generally ascribed to phase segregation, the observations display much discrepancy, and the mechanisms is still under debate.[31, 43, 64-66, 132] The detailed physical process for phase segregation and illumination effect, in particular for gradient bandgap mixed-halide perovskite, has not been discussed before and remains unclear to date.

Compared to the solution-based method, vapor deposition processes allow more uniform deposition of high crystalline perovskite materials in a precisely tuneable and scalable environment. Here, using a two-step chemical vapor deposition (CVD) method, we fabricated high-quality halide-mixed $FAPb(Br_xI_{1-x})_3$ nanoplatelets (NPs) by using halide substitution from pure $FAPbI_3$. In the suitably thick NPs, the ratio between Br and I exhibit gradual variation along the depth, and therefore gradual bandgap changes from 2.29 eV ($FAPbBr_3$) to 1.56 eV ($FAPbI_3$). The gradient halide composition along the thickness is demonstrated by a depth-resolved energy dispersive spectroscopy (EDS) measurement. Using steady-state micro-PL imaging and time-resolved PL methods, we investigate the halide substitution and the special configuration of halide composite along the depth. We show the PL funneling in such gradient bandgap NPs. Light illumination-induced phase segregation is observed and discussed in the gradient bandgap NPs.

5.2 Experimental Section

The $FAPb(I_xBr_{1-x})_3$ nanosheets were fabricated by the CVD method.[133] First, 1 mg of PbI_2 powder was dissolved in 1 mL of deionized water and heated at 90 °C to get the saturated PbI_2 aqueous solution. Hexagonal PbI_2 nanosheets were observed a few minutes after the solution was dropped into glass substrate. Second, the FAI powder was placed at the center of a CVD furnace, while the substrates with PbI_2 nanosheets were mounted downstream of the apparatus. During the whole vapor conversion process, temperature was 140 °C, and pressure was $\approx$500 mTorr with a controlled Ar gas flow rate of 35 sccm. After around 2 h, $FAPbI_3$ NPs were synthesized. Then, under excess FABr vapor environment at the same temperature and pressure, bromide substitution occurred partially or completely depending on the thickness of the as-grown $FAPbI_3$ nanoplatelets. $FAPb(Br_xI_{1-x})_3$ perovskite NPs on glass substrates were finally resulted.

Steady-state PL spectra and PL decay trace were performed on a microscopic system. Hybrid perovskite NPs were excited by a 405 nm picosecond diode laser (pulse duration 50 ps) at 2.5 MHz repetition rate through an objective. PL was collected and focused onto the spectrometer and detected by a CCD detector. FLIM and TRPL were recorded by confocal microscopy (Picoquant Micro Time 200). The thickness of the sample was measured using an optical profiler (Bruker). All the measurements were conducted at room temperature.

5.3 Gradient bandgap structure of the mixed-halide perovskite nanoplatelets

The mixed-halide perovskite NPs were prepared by a two-step CVD method, as schematically shown in Figure 5.1 (a) (see the “Experimental Section” for details). First, saturated PbI_2 solution was cast onto a glass substrate and heated at an elevated temperature, during which PbI_2 nanosheets will nucleate.[43, 132] Subsequently, the $FAPbI_3$ perovskite NPs were fabricated by intercalating the FAI molecules into the interval sites of PbI6 octahedron layers.[43, 132] The thicknesses of these NPs vary from dozens to thousands of nanometers. In the second step, to synthesize halide-gradient $FAPb(Br_xI_{1-x})_3$ NPs, as-grown $FAPbI_3$ perovskite NPs were placed in excess FABr vapor environment. During this process, halide exchange reaction occurs, i.e., the iodide in $FAPbI_3$ is slowly replaced by bromide, from the top surface and then gradually to the inner part of the NPs. It is expected that the thickness plays an integral role in determining the internal structure of $FAPb(Br_xI_{1-x})_3$ NPs as iodide is partially or completely exchanged by bromide at certain reaction time. Thus, these NPs can be classified into thin (dozens of nanometers), medium (hundreds of nanometers), and thick (thousands of nanometers) NPs according to their thickness. Similar halide substitution of perovskite has been studied in solution and thin films,[134-135] but still not seen in the CVD method.

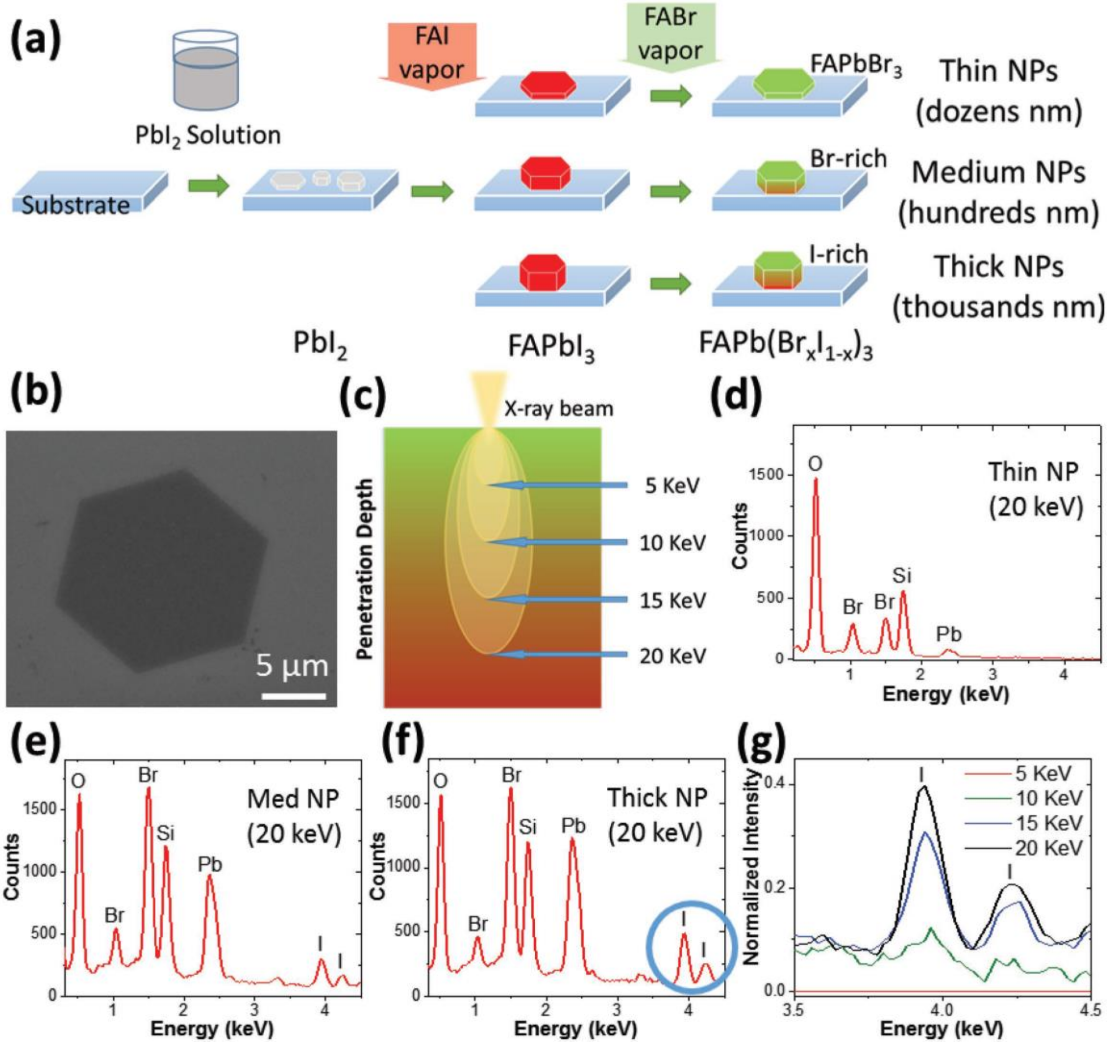

Figure 5.1 (a) Schematics of the CVD fabrication of FAPb(Br$_x$I$_{1-x}$)$_3$ NPs by halide exchange reaction in FAPbI$_3$ NPs with different thicknesses. (b) Typical SEM image of a thick NP. (c) Schematic of the EDS e-beam penetration depth within thick perovskite NP of energy deposited at 5, 10, 15, and 20 keV. EDS results of (d) thin (dozens of nanometer), (e) medium (hundreds of nanometer), and (f) thick (thousands of nanometer) FAPb(Br$_x$I$_{1-x}$)$_3$ NPs, respectively. (g) Enlarged iodide peaks of EDS spectra under different e-beam energies of the thick NP.

The scanning electron microscopic (SEM) image of an NP is shown in Figure 5.1 (b), illustrating that the as-grown perovskite NP exhibits a hexagonal shape with good uniformity. EDS with different e-beam energy (5, 10, 15, and 20 keV) and thus different penetration depth was used to examine the compositional distribution of the $FAPb(Br_xI_{1-x})_3$ NPs. The scheme of penetration depth–dependent EDS is shown in Figure 5.1 (c). First, a 20 keV e-beam is used for the measurements of thin (Figure 5.1 (d)), medium (Figure 5.1 (e)), and thick (Figure 5.1 (f)) NPs. For the thin NP, bromide was the only presented halide anion, without the peak of iodide. As the penetration depth of a 5 keV e-beam in perovskite is around 100 nm,[136] the depth of 20 keV e-beam should be deeper, indicating that elementary information across the entire thickness is included in the EDS result, conforming the iodides have been completely substituted by bromides. For the medium NP, in contrast, the component of iodide is displayed with a dim iodide peak (Figure 5.1 (e)), while bromide portion is still the dominant halide component. Considering the thickness of medium NP is about 200 nm, the penetration depth of the 20 keV EDS e-beam is estimated to be 200 nm or deeper. For the thick NP, evident signal of iodide is detected. To further understand the material, EDS measurement is conducted under different e-beam energies, and the results are normalized by the peak of lead (Figure 5.1 (g)). When detected in 5 keV, the iodide signal cannot be seen, confirms that the iodide ions on the top surface have been fully substituted by bromide ions. As the penetration depth increases, iodide peak increases, confirming the gradually increased iodide along the depth.

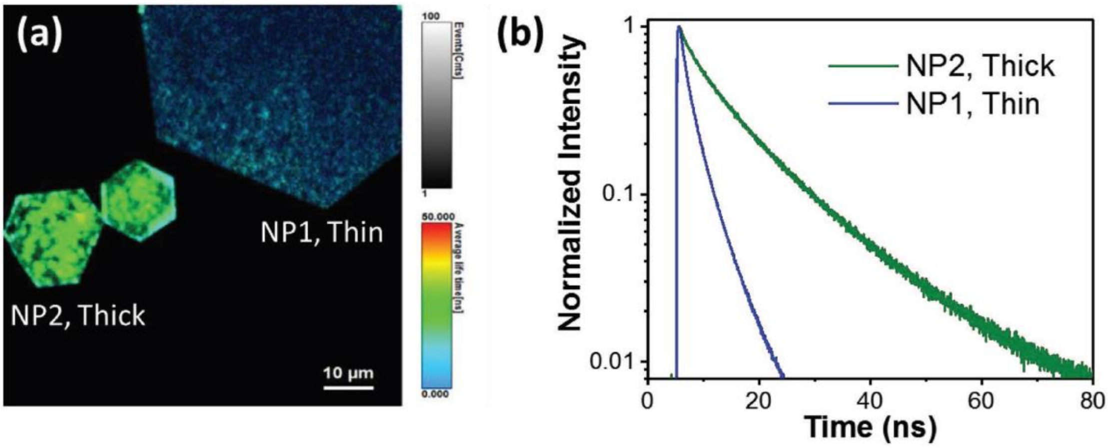

Figure 5.2 (a) FLIM image of thin (large, blue) and thick (small, green) perovskite NPs. Here the brightness represents the PL intensity and the color represents the PL lifetime. (b) The corresponding PL decay traces of NP1 (thin) and NP2 (thick).

Fluorescence lifetime imaging microscopy (FLIM) measurements were performed based on time-correlated single photon counting (TCSPC) technique (Figure 5.2 (a)).[137] One thin and two thick NPs were investigated. With an excitation wavelength at 405 nm (PL spectra are detected through reflection configuration), the FLIM image displays PL intensity (brightness) and photon lifetime (color) of perovskite NPs under the identical excitation. The FLIM image of a single NP shows a generally uniform brightness and color (blue for thin NP or green for thick NPs), means the carrier dynamics across the whole NP plane are generally homogeneous. On the other hand, NPs of different thicknesses show different PL lifetimes. The lifetimes of NP1 (thin) and NP2 (thick) are extracted and shown in Figure 5.2 (b), where thick NPs exhibit significantly longer lifetime than the thin one. A possible reason is the impact of surface recombination that leads to a shorter lifetime in thin NPs.[52] Another likely reason is that the PL lifetime of I-rich perovskite is naturally longer than the Br-rich perovskite.[7, 138] Thus, the significantly longer lifetime may indicate the higher iodide portion in the thick NPs, which is well consistent with the EDS results in Figure 5.1.

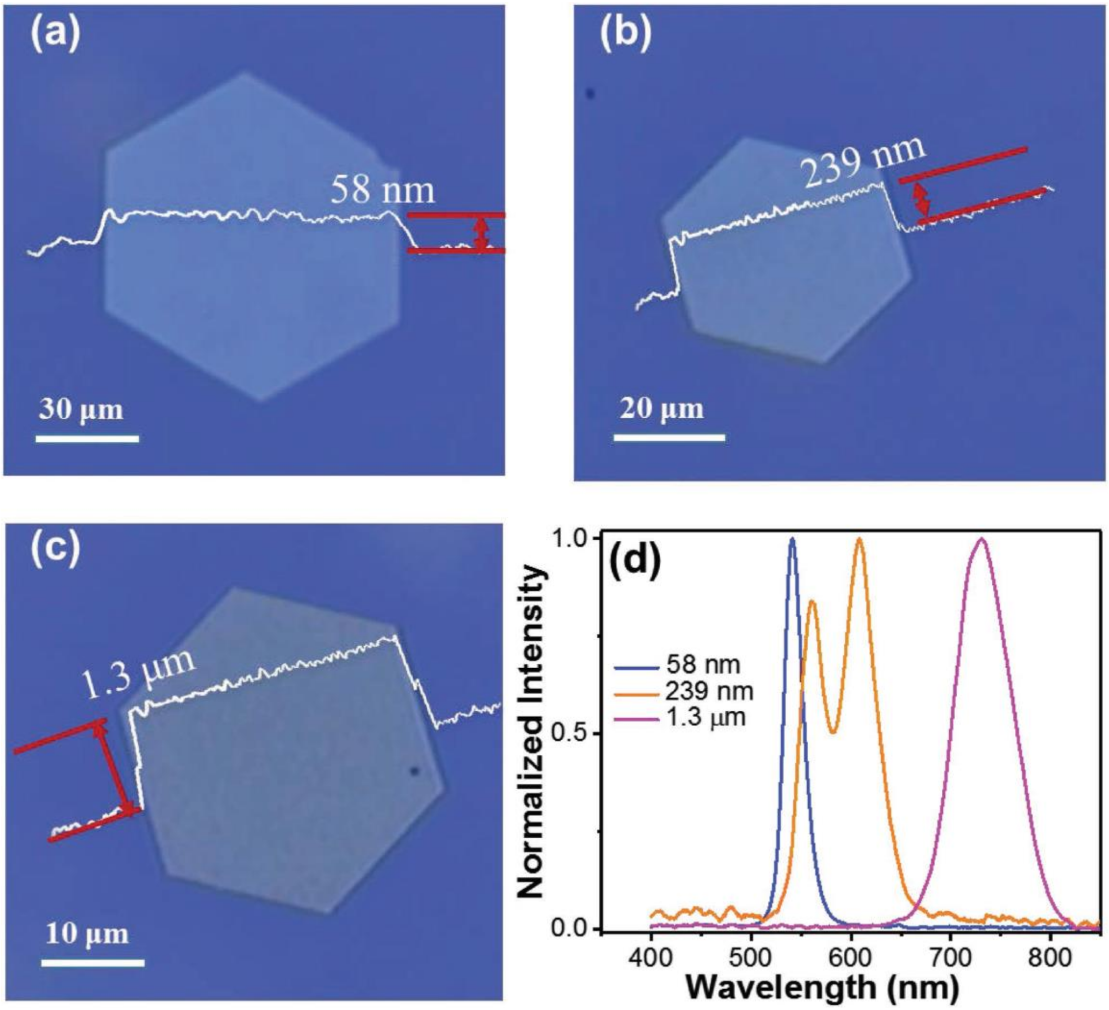

Figure 5.3 Optical images of FAPb(Br$_x$I$_{1-x}$)$_3$ NPs with different thicknesses. The height profiles indicate the thickness of (a) 58 nm, (b) 239 nm, and (c) 1.3 µm. (d) Normalized PL of NPs with different thickness excited at 405 nm.

To obtain clear insight into the halide substitution in the NPs by the FABr vapor process, three groups of perovskite with typical thicknesses of thin (58 nm), medium (239 nm), and thick (around 1300 nm) NPs are selected for detailed investigation. Their optical microscopic images and thicknesses are shown in Figure 5.3 (a–c). These images illustrate that the as grown perovskite NPs maintain good uniformity, consistent with FLIM images. Steady-state PL spectra were acquired for probing the halide substitution because the ratio of halide composite can sensitively result in the PL shift.[15] Upon the iodide anion being replaced by bromide anion (ratio of iodide to bromide decreases), the bandgap energy increases,[15, 30, 62] and a blueshift in PL spectrum is expected. Steady-state PL spectra of NPs with different thicknesses were measured using the transmission configuration (laser excited from the perovskite surface side and PL collected from the substrate side), as displayed in Figure 5.3 (d), the scheme of transmission/reflection configuration in a thick NP is shown in Figure 5.4 (a). As the NP thickness increases, the PL peak shifts to the longer wavelengths, confirming that thickness plays an important role in determining the composition distribution of NP structure. Specifically, for thin NP (58 nm), the PL peak is located at around 540 nm. This PL peak is very similar to the typical peak of $FAPbBr_3$ perovskite.[125] It indicates that the iodides in $FAPbI_3$ have been completely substituted by bromide during the process of FABr vaporing, resulting in $FAPbBr_3$ structure in the entire NP, consistent with the EDS results. The PL spectrum of the medium thickness NP (239 nm) has significantly distinctive features with two peaks at around 560 and 610 nm, approximately, corresponding to $FAPb(Br0_{.85}I_{0.15})_3$ and $FAPb(Br_{0.67}I_{0.33})_3$, indicating that the iodide has not been fully substituted and thus the PL spectrum displays consistently with mixed-halide perovskite in the composite.[125] The thick NP (1.3 μm) exhibits a very broad PL spectrum (71 nm of full width at half maximum(FWHM)), which suggests that the broad PL band originates not only from the pure iodide phase ($FAPbI_3$ with the center around 790 nm) but also from the bromide–iodide mixed phase(such as $FAPbBrI_2$ with the center around 700 nm).

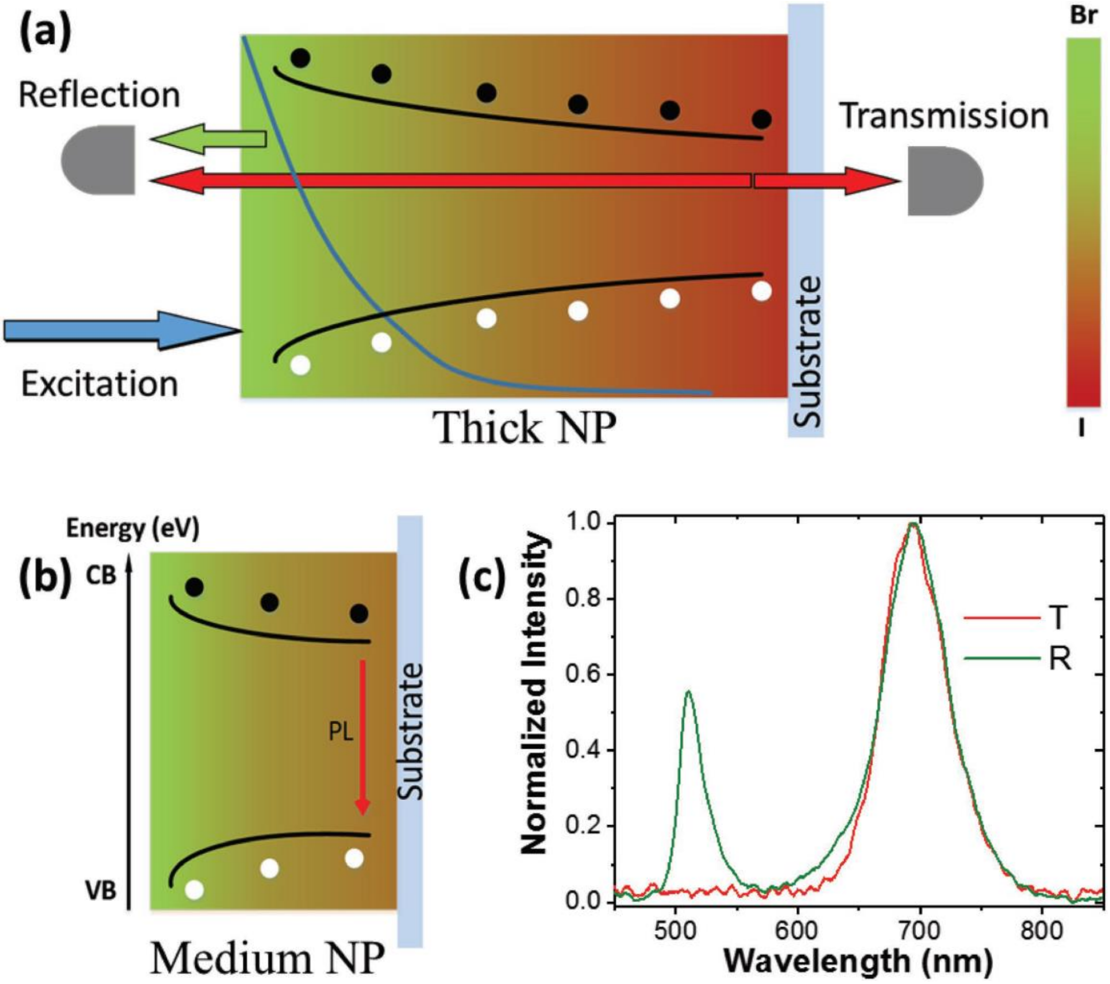

Figure 5.4 (a) Schematic showing the experimental setup of transmission and reflection experiments for the thick NP (≈1 μm) with bandgap structure comprising a Br-rich region and an I-rich region. (b) Schematic illustration of bandgap structure of the medium (≈200 nm) halide-gradient $FAPb(Br_xI_{1-x})_3$ perovskite NP. (c) PL spectra of a thick NP (thickness ≈1 μm) from both transmission and reflection geometries.

For the medium thickness NP (239 nm), the 560 nm minor PL peak indicates the coexistence of bromide and iodide halide compositions (Br-rich phase) in the NPs. Note the PL spectrum is measured in the transmission configuration and the penetration depth for 405 nm laser is ≈140 nm ($\alpha = 0.7 \times 10^5$ cm^{-1}).[139] The bandgap of the mixed-halide perovskite decreases upon increasing the ratio of iodide to bromide.[140] The initial emitted photons cannot pass through the bottom layer; instead, there is a strong possibility for them to be absorbed by the following layers and re-emit photons at lower energy phases. The energy difference between the surface side (540 nm) and this minor emission peak (560 nm) is calculated to be $\Delta E \cong 0.08$ eV, which is sufficient to create an effective energy funnel.[11-12] Consequently, only lower-energy PL peaks were observed. As the sample was excited from the surface side ($FAPbBr_3$ region, high bandgap) and the PL emission was detected from the substrate side $FAPb(Br_xI_{1-x})_3$ region, low bandgap), it is evident that the fabricated medium NP has a halide-gradient bandgap structure, as schemed in Figure 5.4 (b). In such a structure, driven by the energy funneling, the charge carriers will transfer directly from $FAPbBr_3$ layers to Br-rich layers and recombine in the low-bandgap side, which results in a high PL efficiency.

It is interesting to note that another major peak at lower energy (610 nm) was also observed in the medium thickness NP. Essentially, such double peaks should originate from two composites with different ratios of I/Br, corresponding to two separated bandgaps. We ascribe this to the formation of Br- rich and I-rich domains in the NP during the FABr vaporing process due to inhomogeneous diffusion and the substitution of bromide anions.[141] In these domains, the ratio of iodide to bromide fluctuates and therefore emits at slightly different wavelengths.[141-142] Moreover, for the formation of relatively stable domain, the ratios of Br/I in the mixed-halide perovskite cannot be an arbitrary number; instead, they are usually some discrete values.[62] This results in the formation of separated I-rich domains and Br-rich domains in the Br-rich region.

For the thick (1.3 μm) NP (Figure 5.4 (a)), it is reasonable to assume that the halide substitution on the surface side is almost completed as bromide is the dominant halide anion at the surface side. While at the substrate side, the observation of 735 nm PL peak suggests I-rich $FAPb(Br_xI_{1-x})_3$ phases remain at the bottom. For thin and medium NPs, the light will penetrate more than the thickness of the nanoplatelet. While for the thickness of thick NPs, upon laser excitation, the photogenerated carriers initially distribute near the surface as the thickness of 1.3 μm is significantly larger than the penetration depth of the excitation laser. In the special gradient bandgap structure, although the excitation only penetrates to a shallow surface, the photogenerated carriers will not only recombine directly but also funnel and recombine finally in the lowest-energy bandgap region. The observation of a broader PL peak in the thick NP, spanning from 700 to 800 nm, suggests a fluctuation of I/Br ratio in the I-rich $FAPb(Br_xI_{1-x})_3$ region, which even includes pure iodide phase ($FAPbI_3$) at the substrate side. We speculate the I-rich FAPb(Br_xI_{1-x})$_3$ phase is formed and pure iodide $FAPbI_3$ phase is preserved around the substrate side during the FABr vaporing process, due to inhomogeneous diffusion and substitution of bromides. For PL measurement by transmission configuration, the apparent PL spectrum critically depends on the bandgap of the bottom layers and therefore is composition dependent. In such a heterogeneous NP, the broadband PL spectrum can be ascribed to the inhomogeneous bandgaps of different bromide compositions.

However, whether the downward funneling of carriers is through photon recycle[143] or carrier diffusion[69] is still unknown. To make it clear, a thick NP (thickness ≈1 μm) was chosen and measured in both transmission and reflection geometry (Figure 5.4 (c)). As shown in the result, the PL by transmission only exhibits a 690 nm peak in the I-rich region at the bottom, while the PL by reflection shows a small peak in the Br-rich region at the surface in addition to the 690 nm peak. For any photogenerated carriers, two competitive processes simultaneously occur: effective carrier diffusion toward the low-bandgap region or recombination (also result in photo recycling). Note that the emission of the low bandgap due to carrier funneling can also be detected in the reflection geometry because of the low absorption for the emission of the low bandgap. Assuming the photon recycling process is dominant, the peak from the Br-rich region should be dominant in reflection geometry, and it may not totally disappear in the transmission mode. The observations evidently disagree with photon recycling assumption. As discussed above, the carrier diffusion dominates the energy funneling process.

5.4 Illumination-induced halide segregation in the perovskite nanoplatelets

In order to reveal the insight of halide substitution in the mixed-halide perovskite NPs, PL spectra of these FAPb(Br_xI_{1-x})$_3$ NPs were investigated under continuous illumination with a constant intensity (λexc = 405 nm, Iexc = 358 mW cm−2). As illustrated in Figure 5.5 (a), for the thin NP, no PL peak shift was observed in 300 s observation time. The PL intensity also did not exhibit significant variation during the observation time. This is not surprising since there is no phase segregation occurring under light illumination because the iodides in $FAPbI_3$ have been completely substituted by bromides during the FABr vaporing. The stable intensity indicates the excellent photostability in such CVD-fabricated NPs, consistent with the previous reports.[132] For a medium NP (Figure 5.5 (b)), two distinct peaks at 560 and 610 nm are observed initially. Upon illumination, the PL intensity of the 610 nm peak decreased and accompanied by an increase of the PL intensity of the 560 nm peak. The evolution of PL intensity (Figure 5.5 (c)) clearly shows their gradual changes, both tend to saturate after around 10 min. The 560 nm peak finally dominates the spectrum. In the thick 1.3 μm NP, the PL spectrum exhibits a substantial shift from 735 to 790 nm with continuous wave illumination, while the FWHM decreases from 71 to 58 nm.

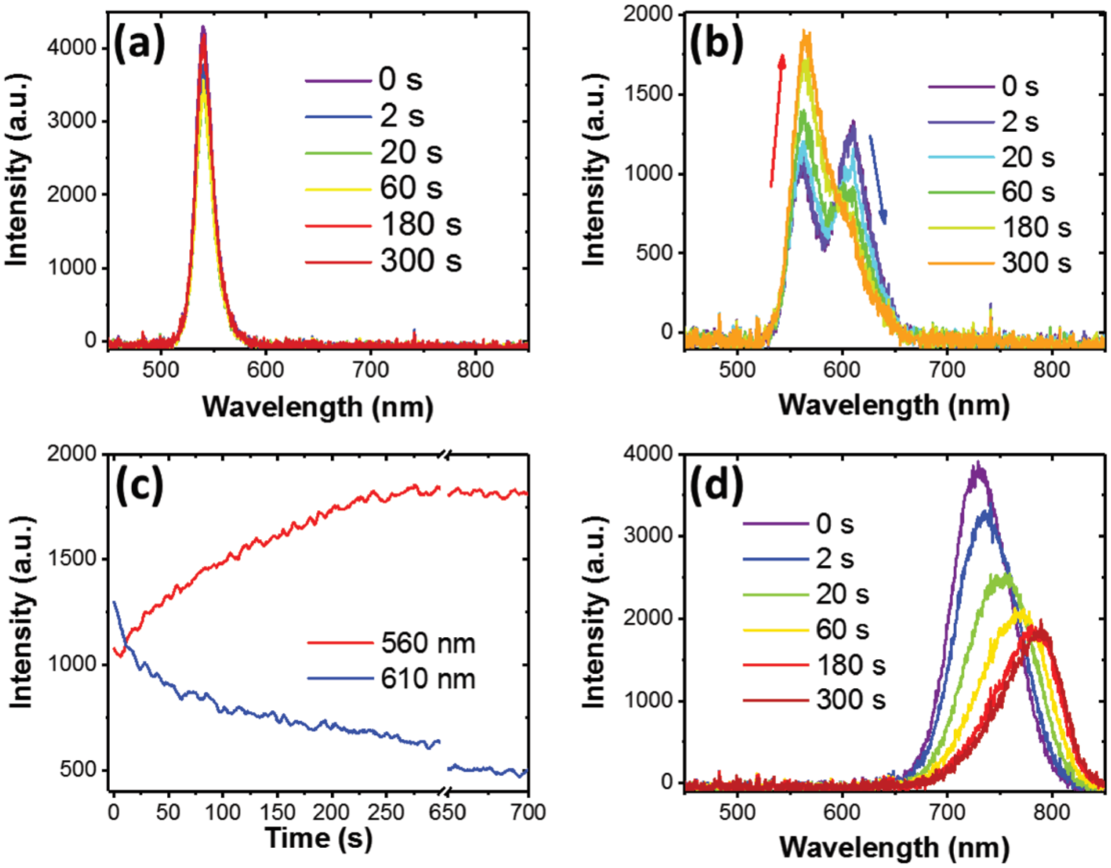

Figure 5.5 PL spectra taken under 405 nm continuous illumination for NPs with thicknesses of (a) 58 nm, (b) 239 nm, and (d) 1.3 μm. (c) PL intensity of the two peaks of the medium thickness NP as a function of the illumination time.

To obtain quantitative insight into the illumination-induced halide substitution, the PL spectra of the 239 nm thickness NP were fitted by two Gaussian profiles at several illumination times. Each PL spectrum can be well fitted; for instance, the fitting of spectra after 20 s continuous illumination is shown in Figure 5.6 (a). The evolution of Gaussian components within 5 min is shown in Figure 5.6 (b). The intensity of 560 nm band (Gaussian amplitude) can be fitted by a one-exponential function, and a time constant (rise) of 186 s is acquired. While the intensity of 610 nm band is well fitted by a two-exponential function, two time constants of 30 and 185 s are acquired. The similar time constant of around 186 s for the increase of 560 nm peak and the decrease of 610 nm peak suggests an intrinsic correlation between them. It is reasonable to speculate that this is due to the halide substitution reaction induced by the illumination.

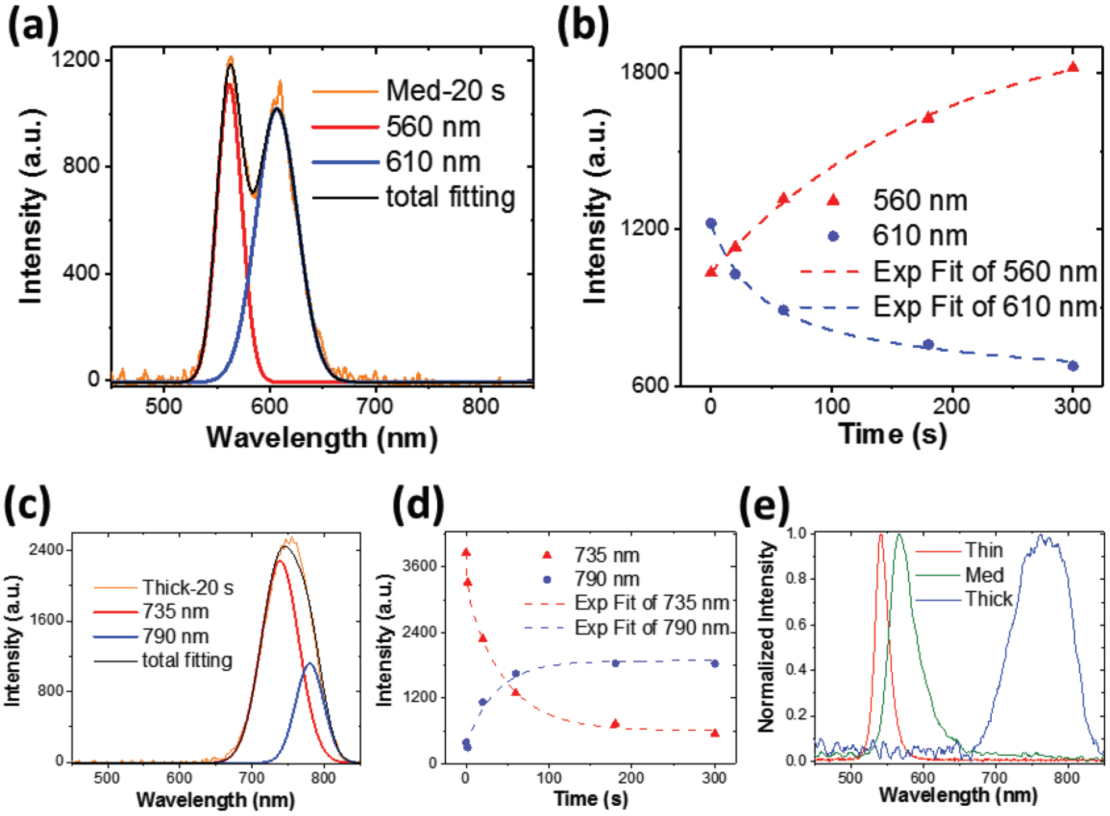

Figure 5.6 (a, c) PL spectra and their two-Gaussian fitting taken after 405 nm continuous-wave illumination for 20 s for (a) medium and (c) thick NPs. (b, d) PL intensity of the two subpeaks as a function of the illumination time. Relative intensity as a function of time for (b) medium and (d) thick NPs. The solid lines are the

exponential fits of the plots. (e) Normalized PL spectra of thin, medium, and thick NPs after continuous illumination for 5 min followed by 1 week in the dark.

Upon laser illumination, carriers on the top surface layers ($FAPbBr_3$) are photogenerated to the high excited state and then relax quickly into the edge of the conduction and valence bands by emitting phonons.[144-145] Then, these charge carriers transfer toward the substrate side (I-rich layers) by carrier diffusion due to the specific gradient bandgap, passing energy to the longitudinal optical (LO) phonon.[146] The influence of transverse optical phonon and acoustic phonon can be ignored in this process.[147-148] The LO phonon provides the driving force to deform the surrounding halide anion lattice through entropy, stochastic composition fluctuations, and lattice strain.[146] Some of the halide ions are then activated as mobile ions.

The 560 nm band corresponds to the average iodide/ bromide ratio at the substrate side, while the 610 nm band originates from the I-rich domains. For the 610 nm peak, the fast time constant of 30 s may be ascribed to the initial illumination-induced iodide activation, and then these iodide ions escape from the lattice. The decrease of 610 nm band is due to the iodide escape from the I-rich domains and therefore decrease of the fluorophore. During the FABr vaporing process, it is expected that many bromide anions diffuse into interstitial structure of the NP but not yet substitute iodides.[149-150] Iodide anions are thus surrounded by a large portion of bromide anions, making them unstable and likely to be activated at this phase. Upon light illumination, these iodide ions are activated (for about 30 s), and the vacancies are gradually substituted by the interstitial bromides. Such an illumination- induced halide activation and substitution of bromide to iodide result in an increase of 560 nm band and a decrease of 610 nm band with the similar time constant of 186 s. After that, the gradient bandgap halide perovskite structure is getting smoother; more electrons can transport directly to the substrate side, recombine with holes, leading to the increase of the 560 nm PL peak.

For the thick 1.3 μm NP, the broad PL peak can be fitted nicely by a two-peak Gaussian function with centers at around 735 and 790 nm, respectively. Figure 5.6 (c) shows the fitting result of the spectrum with 20 s of illumination. This suggests the broad PL band consists of both pure iodide phase ($FAPbI_3$) and I-rich phase ($FAPb(Br_xI_{1-x})_3$). Hoke et al. reported that light illumination induces the formation of a strong and reversible sub-bandgap PL at around 1.68 eV (738 nm), which disappears after several minutes in the dark (Hoke effect).[31] This band has been attributed to phase separation and the formation of I-rich domains.[140, 151] Figure 5.6 (d) shows the evolution of intensities of these two peaks as a function of the illumination time. The evolutions can also be fitted by an exponential function and a similar time constant of 36 s can be obtained. With continuous illumination, charge carriers are photogenerated initially at surface layers, followed by the carrier diffusion/photon recycling and finally emit at bottom layers with lower bandgap. During this process, the phonons are well emitted and therefore effectively activate halide ions and thus initiating the halide substitution. The similar time constant 36 s of the 790 nm band increase and the 735 nm band decrease suggest that the bromides are substituted by the iodides in the I-rich phase (bottom layers) upon illumination. It is interesting to note that the Br-rich layers and I-rich layers exhibit opposite substitution tendency, that is, 610 nm band to 560 nm band in the medium NP (iodide is substituted by bromide) and 735 nm band to 790 nm band in the thick NP (bromide is substituted by iodide). This is probably ascribed to the fact that the Br-rich domain (735 nm band) is a metastable phase and therefore tends to transform toward the stable pure phase of $FAPbI_3$.[31, 62]

We emphasize that the illumination-induced wavelength shift is irreversible, which is very different from many previous reversible observations.[31, 152] After illumination, the NPs were stored under nitrogen atmosphere in the dark at room temperature for 1 week, and the PL spectra keep unchanged (Figure 5.6 (e)). In fact, in previous reports, both reversible and irreversible phase segregations have been reported,[153] depending on the external stimulations and initial structures. For our gradient bandgap mixed-halide perovskite NPs fabricated by the CVD method, the substitution reaction is abruptly stopped; thus, the acquired samples are metastable phases. In other words, the initial structures before irradiation are less stable. When they are exposed to intensive illumination, the metastable phases segregate into I-rich and Br-rich phases to reach the lowest energy and most stable structure. This suggests the illumination-induced formation of composition and lattice has improved stability. Phase segregation originates from halide migration and substitution, which will affect perovskite composition and thus lattice structure and lattice strain. Illumination-induced phase segregation is most likely to improve compositional uniformity, reduce defect density, and also significantly improve the stability, which is a great benefit to the practical applications. Note that segregation may be driven by the strong gradient in carrier generation rate in some cases.[63] As high density of carriers is generated near the surface, phonon density is higher near the surface. As a consequence, the halide ions are likely activated by phonon coupling, and segregation occurs near the surface. In our sample, gradient carriers are similarly generated. Then, carriers quickly diffuse toward the low-bandgap region due to effective funneling. The activation and movement of halide are intrinsically driven by electron– phonon coupling, which mainly happens during the cooling of hot carriers. Therefore, halide segregation is expected to occur along the depth. The gradient charge carrier distribution also has minor influence on the segregation process.

Moreover, the time constant of 35 s extracted from the evolution of I-rich phase is significantly shorter than that occurring in Br-rich phase, 186 s. The time constant essentially represents the halide exchange rate. This confirms that halide substitution of iodide by bromide in the Br-rich layer is much slower (186 s) than that of bromide by iodide in the I-rich layer, under the same illumination condition. This is very different from Pellet et al.'s observation of halide exchange by infiltrating in halide solution;[66] in their case, the exchange of iodide by bromide is striking fast while the exchange of bromide by iodide is slower. The observed PL band of 735 nm is coincidently the same as that in the Hoke effect. However, 735 nm band exhibits quite different dynamic features in our thick NP. For instance, illumination results in its decrease or disappearance, and the tendency is irreversible. Moreover, the significant shorter time constant of 35 s confirms that it is a metastable phase.

5.5 Conclusions

The mixed-halide compositional gradient $FAPb(Br_xI_{1-x})_3$ perovskite NPs are fabricated by the two-step CVD method; first, $FAPbI_3$ NPs are prepared and then followed by the treatment by FABr vaporing. During the FABr vapor process, bromide ions substitute iodide ions gradually from the top surface (Br-rich phase) to the bottom (I-rich phase). Consequently, a specific gradient bandgap structure is achieved from $FAPbBr_3$ (2.29 eV) to $FAPbI_3$ (1.56 eV). The different ratios of iodide to bromide have been obtained in different thickness NPs. In such a gradient bandgap structure, photogenerated carriers can effectively transfer to the low-bandgap region by energy funneling and emit at redder wavelengths. Accordingly, PL spectra were observed in 540, 560/610, and 735/790 nm for thin, medium, and thick NPs, respectively. We have observed the illumination-induced phase segregation in the NPs with different thicknesses. With illumination, the PL spectrum of Br-rich phase exhibits blueshift and, therefore, 610 nm band disappears. In contrast, redshift is observed in I-rich phase due to the decrease of 735 nm band and increase of 790 nm band. We demonstrate the formation of irreversible and stable phases with illumination in both Br-rich and I-rich phases. This investigation provides significant insight into the halide segregation in such specific gradient bandgap perovskites, greatly benefits their future optoelectronic applications, such as solar cells, LEDs, and lasers.

The work in this chapter has been published in the journal article: Zhou, C.; Ou, Q.; Chen, W.; Gan, Z.; Wang, J.; Bao, Q.; Wen, X.; Jia, B. Illumination-Induced Halide Segregation in Gradient Bandgap Mixed-Halide Perovskite Nanoplatelets. Advanced Optical Materials 2018, 6 (24), 1801107. [154]

Chapter 6

Spatially Modulating the Fluorescence Color of Mixed-Halide Perovskite Nanoplatelets through Direct Femtosecond Laser Writing

Lead halide perovskites are widely applied in not only photovoltaics but also on-chip light sources and photon detection. To promote the incorporation of perovskite into integrated devices, microscale color patterning flexibility is a very important step. Here, we demonstrate spatially resolved modulation of the fluorescence of nanoplatelets (NPs) by femtosecond direct laser writing (fs-DLW). As the perovskite NP for the fs-DLW pattern is specially designed with a gradual bromide−iodide composition along the depth, the replacement of iodide ions by bromide ions can be activated under a controlled laser pulse and fluorescence is thus modulated from red to green. The effect of processing depth and NP thickness on fluorescence modulation is systemically investigated. The as-grown thick NP (thickness ≈ 500 nm) mainly exhibits a 690 nm emission from the bottom iodine-rich phase. After halide substitution induced by fs-DLW, a new fluorescence peak appears in the wavelength range of 540−600 nm; the peak position and intensity are controlled by the DLW conditions. The fluorescent color is spatially modulated from red to green, enabling microscale-resolved multicolor emission. Compared with other currently available techniques, microscale color patterning via fs-DLW is a straightforward mask-free one-step operation, yielding high spatial resolution and enabling three-dimensional patterning by the multiple-photon method. We demonstrate that arbitrary patterns can be drawn on a wide range of perovskite NPs, implying the potential applications in microencryption, sensors, multicolor displays, lasers, and light-emitting devices.

6.1 Introduction

The mixed organic−inorganic hybrid lead halide perovskites have attracted enormous attention for optoelectronic applications, including solar cells, light emitting devices, photodetectors, and lasers.[2, 112, 155-170] One of the important advantages is that their band gaps and consequently the emission/absorption wavelengths can be flexibly tuned by halide compositions.[88, 171-176] For the light-emitting applications, color-tunable light-emitting diodes and lasers have been realized via mixed halide perovskites.[46, 177-178] On the other hand, regarding photovoltaic applications, the composition-dependent electronic structures allow precise engineering of their optical response between ~1.5 and 2.4 eV, enabling the harvesting of the full solar spectrum in the visible range.[46, 179-181] A state-of-the-art tandem cell made with silicon and perovskites could surpass 30% efficiency.[182-183]

Integration of various compositions of mixed perovskite into one chip or direct fabrication of precise micropatterns on a single perovskite crystal is of great importance for high performance semiconductor optoelectronic devices, such as photonic chips, multicolor displays, band-tunable photodetectors, and nanolasers. However, spatially inhomogeneous halide distribution on a single nanoplatelet (NP) or nanowire is still a challenge. In 2003, Cheng et al. reported the patterning on a perovskite film by using a pioneering soft lithographic method via a contact molding approach.[184] To date, lithographic and contact printing are the main methods used to pattern perovskite materials. For example, uniform and wafer-scale patterning was achieved by photolithographic patterning of PbX_2 seeds followed by vapor-phase conversion to perovskites.[185-186] Meanwhile, a liquid-contact printing method was also developed to control the size and location of perovskite crystals.[187] These methods offer potential pathways to scalable patterning on perovskite but are inherently multi-stepped and rely on masks. To avoid using masks, Chou et al. developed a direct laser writing (DLW) procedure for lead halide perovskites,[188] taking advantage of the inverse relationship between solubility and temperature of lead perovskite precursors.[189] This technique enables the spatially confined crystal growth from the precursor solution, using a laser to induce microscale heating of a transducing substrate. They demonstrated arbitrary pattern formation of crystalline $CH_3NH_3PbBr_3$ on a range of substrates and fabricated a microscale photodetector using this approach.[189] However, this DLW technique fails to spatially tune the band gap. Recently, Dou et al. showed that the nanofabrication techniques can be combined with anion-exchange chemistry, which can precisely control the halide composition in single-crystalline halide perovskite nanomaterials.[74] In their design, the exposed part of a nanowire after e-beam lithography is dipped into oleylammonium halide solution for an anion-exchange reaction. The acquired heterojunctions show distinct electronic states across the interface; thus, spatially resolved multicolor $CsPbX_3$ (X = Cl, Br, I, or alloy of two halides) with the photoluminescence (PL) tunable over the entire visible spectrum is realized.

Therefore, to pattern spatially resolved multicolor on perovskites, the current available techniques are multistep methods based on nanofabrication and additional anion exchange treatment. There are opportunities to develop complementary processing techniques for patterning on perovskites to achieve device integration and functionalization. In this paper, the halide composition of the mixed perovskite nanoplatelets (NPs) is specially designed and gradually distributed along the depth so that the DLW can locally change the halide composition according to the processing conditions. Femtosecond (fs) laser fabrication is used to demonstrate significant advantages of high spatial resolution, low surround damage, and high processing efficiency.[76] The fs-DLW can directly induce anion-exchange reactions at specific points within the NPs; therefore, spatially resolved fine-tuning of the chemical composition and electronic properties is achieved without any additional chemical treatment. This straightforward technique allows the possibility to develop a range of optoelectronic devices.

6.2 Experimental Section

Sample Preparation. $FAPb(I_xBr_{1-x})_3$ NPs were fabricated by the chemical vapor deposition (CVD) method.[43, 154] First, 1 mg of PbI_2 powder was dissolved in 1 mL of deionized water and heated at 90 °C to get the saturated PbI_2 aqueous solution. The solution was then dropped into a glass substrate, and hexagonal PbI_2 nanosheets were observed after a few minutes. Second, the FAI powder was placed at the center of a CVD furnace, whereas the substrates with PbI_2 nanosheets were mounted downstream of the apparatus. The temperature was 140 °C, and the pressure was ∼500 mTorr with a controlled Ar gas flow rate of 35 sccm during the whole vapor conversion process. After about 2 h, $FAPbI_3$ NPs were synthesized. Then, under excess FABr vapor environment, bromide substitution occurred partially or completely depending on the thickness of the as grown perovskite NPs. $FAPbI_xBr_{3-x}$ NPs on glass substrates were finally resulted.

Characterization. AFM images were taken by NT-MDT. PL spectra were performed on a microscopic system. Hybrid perovskite NPs were excited by a 405 nm picosecond diode laser (1 MHz, pulse duration 50 ps) through an objective. PL was collected and focused onto a spectrometer. PL images were captured by a colorful CCD detector.

Femtosecond Laser Fabrication. A homemade DLW system was used to fabricate the patterns on the as-grown perovskite NPs.[189] A femtosecond pulsed laser beam (10 kHz, 100 fs pulse, 800 nm) was used to minimize the thermal effect. The sample was mounted on a 3D nanometric piezo stage. The arbitrary patterns were created by a computer-controlled system.

6.3 Theory of fluorescence color modulating

High-quality halide-mixed formamidinium (FA^+, $HC(NH_2)_2^+$) lead mixed-halide ($FAPb(Br_xI_{1-x})_3$) NPs were fabricated by using a two-step chemical vapor deposition (CVD) method.[154] Pure $FAPbI_3$ perovskite NPs were grown in the first step. In the second step, as-grown $FAPbI_3$ perovskite NPs were placed in excess FABr vapor environment for halide substitution. As we previously confirmed,[154] the halide substitution gets completed thoroughly for the thin NPs (tens of nanometers) and the obtained perovskite NPs exhibit a pure bromide phase, whereas, in the suitably thick NPs, the ratio between Br and I exhibits gradual variation along the depth, and therefore gradual band gap changes from 2.29 eV ($FAPbBr_3$, surface) to 1.56 eV ($FAPbI_3$, bottom). This innovative structure enables DLW to regulate halide composition with a specific localization without post chemical treatment.

A homemade fs-DLW system[75, 190] is used to fabricate the patterns on the as-grown perovskite NPs (Figure 6.1 (a)). An 800 nm fs pulsed laser (with a tunable power range from 0 to 2.3 W, repetition rate = 10 kHz) is focused on the surface of NPs by a 100× objective (NA = 0.85). A designed pattern can be fabricated by moving the sample mounted on a three-dimensional (3D) nanometric piezo stage, which is a mask free technique. The incident laser beams directly induce decomposition of the perovskite NP surface, resulting in redundant Br halogen. Subsequently, the halide substitution proceeds in depth. After laser processing, on one hand, a hole is dug at a specific spot. On the other hand, the laser pulses induce the redistribution of halide composition, in which the iodine is replaced by bromine in a depth range determined by the incident laser dose.

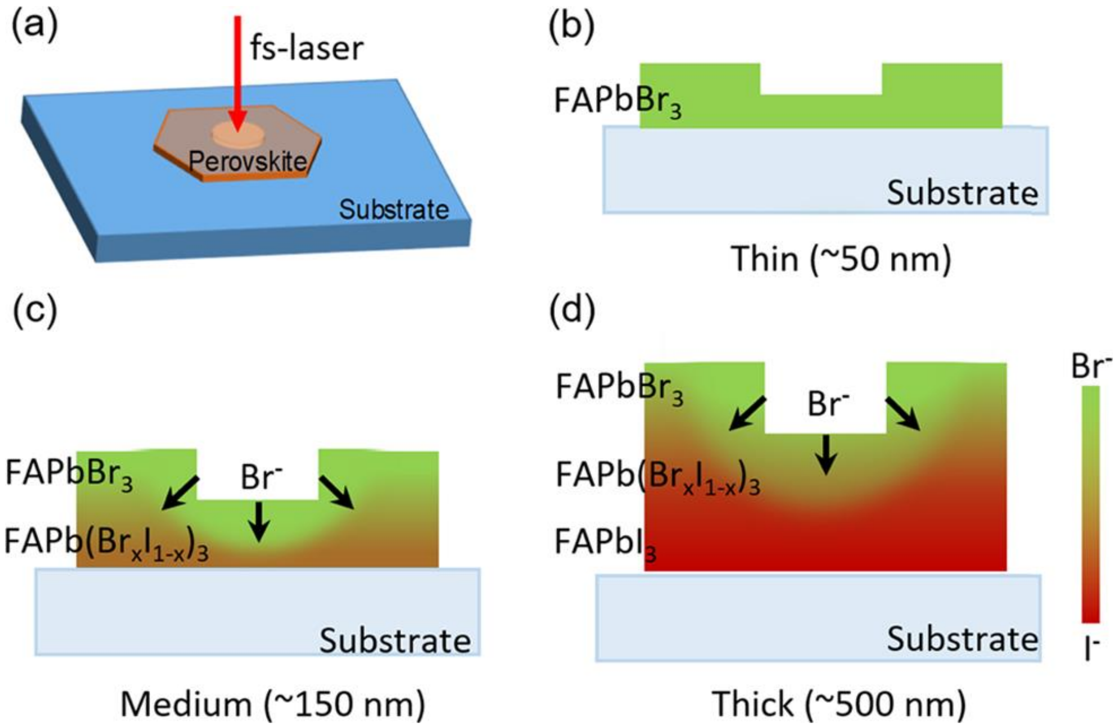

Figure 6.1 (a) Scheme of the DLW on a perovskite NP. (b) Thin NP (~50 nm) after DLW. (c, d) Scheme of the anion exchange on (c) medium NPs (~200 nm) and (d) thick perovskite NPs (500−1000 nm) directly induced by laser writing.

Three different situations are expected depending on the thickness of the NPs. The first case is a thin NP with a thickness of ~50 nm (Figure 6.1 (b)) whose composition before DLW is the pure bromide phase. Thus, there is no anion exchange induced by DLW. The emission will not change after the DLW processing. For the second case, a medium thickness NP with a thickness of ~150 nm is patterned by DLW (Figure 6.1 (c)). The medium thickness is defined by a depth smaller than the depth of focus of the laser beam but allows for the halide substitution. The anion exchange always proceeds throughout the entire depth. The emission of the as-grown medium NP mainly exhibits a mixed phase $FAPb(Br_xI_{1-x})_3$ due to the energy funneling effect,[154] but after fs-DLW, the treated point is expected to exhibit emission of pure bromide phase $FAPbBr_3$. The third typical case (Figure 6.1 (d)) is that of a thick NP with a thickness of about 500 nm (or larger). The redistribution of halide composition relies on the DLW conditions. If high laser energy is applied, the processing depth is expected to be deeper; a larger density of active bromine is generated. As a consequence, the iodine phase $FAPbI_3$ in the bottom largely transforms to mixed phase $FAPb(Br_xI_{1-x})_3$. However, because of the large thickness, the substitution reaction yet cannot reach the lowest bottom layer. Consequently, a boundary of halide composition appears after the DLW. As illustrated in Figure 6.1 (d), the upper side of the boundary is a mixed phase whereas the lower side is a pure iodine phase. The fraction x of the mixed phase is determined by the processing depth. A deeper hole means more substitution reaction, resulting in a larger fraction of Br in the mixed phase. Therefore, after fs- DLW, the thick NP will display two emission peaks, one of the iodine phases and one of the mixed halide phases. And the latter one can be controlled by the fs-DLW conditions.

6.4 Results of spatially modulating the fluorescence color

6.4.1 Modulating fluorescence color in different perovskite nanoplatelets

The three typical cases above are demonstrated by our DLW experiments. As deigned, a series of concentric circles are patterned on the NPs by DLW to fabricate the holes. To facilitate spectral testing, big holes with diameters of about 5−7 μm are fabricated. It is noteworthy that the sizes of the holes do not represent the processing precision. Figure 6.2 (a−c) shows the scheme of the fabricated holes and their depth in thin (Figure 6.2 (a)), medium (Figure 6.2 (b)), and thick (Figure 6.2 (c)) NPs. Figure 6.2 (d−f) shows the pictures of the fabricated holes by atomic force microscopy (AFM). Figure 6.2 (g−i) confirms the corresponding depth profiles on thin, medium, and thick NPs, respectively. At a 405 nm laser excitation, the fluorescence spectra of these NPs and holes were acquired and are shown in Figure 6.2 (j−l); the corresponding lifetime of each spectrum is shown in Figure 6.2 (m−o). Figure 6.2 (a, d, g, j, m) verifies the first case of thin NPs. The thickness is about 50 nm with hole depth of 35 nm. The hole and the as-grown NPs display almost the same PL emission, with only a peak at 545 nm corresponding to the pure bromide phase. For the PL decay curve, a short lifetime was observed in the thin NP, consistent with our previous study.[52] After DLW, the lifetime increases. This can be interpreted as follows: the PL decay in such thin NPs is dominated by the surface states other than the bulk recombination. Meanwhile, the DLW process provides an effect of surface passivation in which the surface trapping is suppressed. Therefore, a slower PL decay was observed due to the decreased surface trapping. However, with increased NP thickness, the bulk recombination becomes the dominant factor for the PL decay.

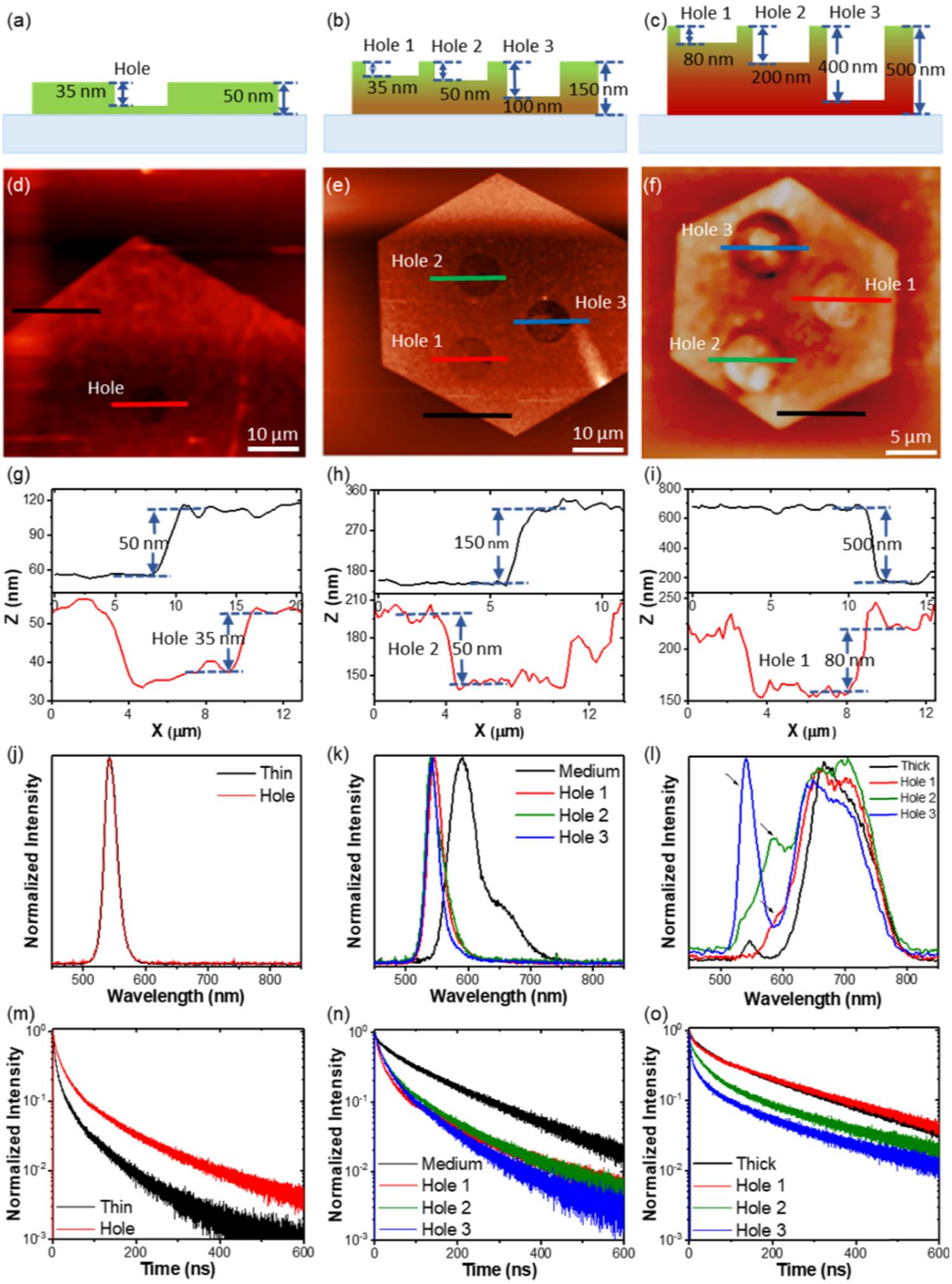

Figure 6.2 (a, b, c) Scheme of the NPs with three typical thicknesses and the fabricated holes by fs-DLW, thin (a), medium (b), and thick (c). (d, e, f) AFM images of the NPs after laser writing corresponding to (a), (b), (c), respectively. (g, h, i) The height profiles of the NPs and a selected hole for each thickness of NP. (j, k, l) PL

spectra measured at different regions on the three typical NPs. (m, n, o) Corresponding PL decay curves of each PL spectrum.

The second case of medium thickness (150 nm) is demonstrated in Figure 6.2 (b, e, h, k, n). Three different holes are fabricated by the DLW. The hole depth increases (35, 50, 70 nm) from hole 1 to hole 3 as the power of fs-laser increases (30, 70, 110 μW). As shown in Figure 6.2 (k), a PL peak located at 590 nm is observed in the as-grown medium NP, suggesting that the Br/I ratio of the bottom layer is about 0.85/0.15,[125] which is a mixed halide phase. After DLW processing, PL of all holes blue-shifts to 545 nm, implying the thorough substitution reaction induced by DLW. The mixed phase completely transforms to bromide phase regardless of the power of laser, which is consistent with our design. The PL decay measurement can further illustrate this. As the thickness increases, longer lifetimes were observed in the original medium and thick NPs. This is due to the shorter intrinsic lifetime of bromide perovskite compared to that of its iodide counterpart.[191] For the holes of medium NP, as the mixed phase completely transformed to the bromide phase after DLW, the lifetimes were expected to be shorter, irrelevant to the depth of the holes. The PL decay results show similar shorter lifetimes for the three holes, which is consistent with the fluorescence spectra.

The results shown in Figure 6.2 (c, f, i, l, o) demonstrate the third case of a thick NP (500 nm). Three holes with depths of 80 nm (hole 1), 300 nm (hole 2), and 400 nm (hole 3) are fabricated with the fs laser power of 100, 150, and 200 μW specifically. The thick NP mainly exhibits a 690 nm emission from the bottom iodine-rich phase, which has been explained by the energy funneling effect in our previous report.[76] As expected, after anion exchange induced by DLW, a new peak appears in the holes. And the new peak shows more wavelength shift and higher intensity with increasing depth (595 nm for hole 1, 580 nm for hole 2, 550 nm for hole 3). Meanwhile, a fast component appears in the PL decay curves and the impact is larger with more wavelength shift, which can be attributed to the larger Br/I ratio of the new peak. It is also noticeable that the PL decay of hole 1 is very similar to the original thick NP, due to the minor impact of both the surface passivation and the small amplitude of 595 nm peak by DLW. In this case, the emission wavelength, i.e., the fluorescent color, can be spatially modulated by the DLW pattern, enabling multicolor emission distributing at microscale resolution. Figure 4.3 shows Commission Internationale de L'Eclairage (CIE) chromaticity coordinates corresponding to the emissions shown in Figure 6.21. The fluorescent color is tuned from red to green.

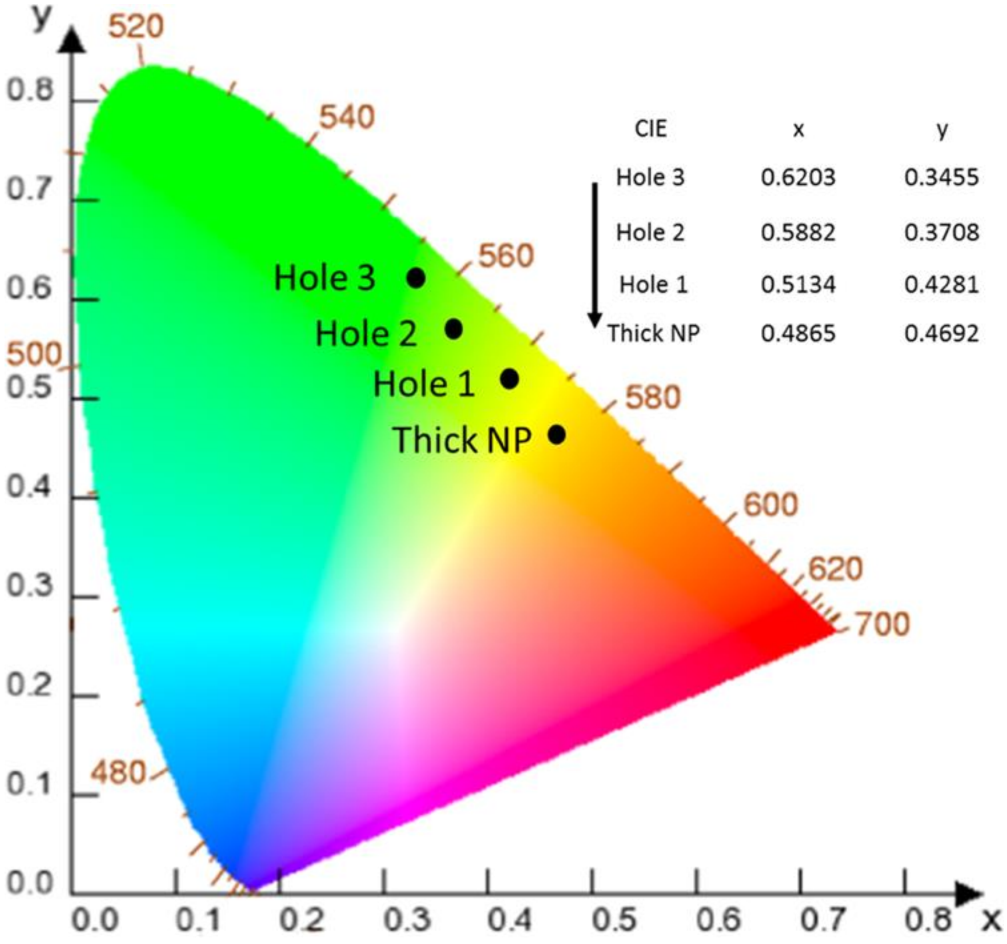

CIE	x	y
Hole 3	0.6203	0.3455
Hole 2	0.5882	0.3708
Hole 1	0.5134	0.4281
Thick NP	0.4865	0.4692

Figure 6.3 CIE coordinates corresponding to emissions of the thick NP and the laser-fabricated holes.

Thus, the spectrum regulation range is broader in thicker NPs. During the synthesis of the NPs by CVD method, the halide exchange reaction occurs from the top surface and then gradually to the inner part of the NPs. As the NP thickness increases, the PL peak shifts to longer wavelengths, indicating a broader range of halide composition. Before laser writing, for a thick NP, the x value of $FAPb(Br_xI_{1-x})_3$ changes from 1 to 0 from the surface to the bottom. However, for a medium NP, the x value is only tunable in the range of about 0.85−1. The laser induced redistribution of halide composition should lie in this range; thus, the thicker the NPs, the broader is the range of spectrum regulation.

6.4.2 Florescence microscope and arbitrary patterns

Figure 6.4 (a, b) shows the fluorescence micrographs of a typical thin NP (Figure 6.4 (a)) and a thick NP (Figure 6.4 (b)) without a pattern by DLW. The as-grown thin NP displays green color whereas the thick NP shows red color when excited by a 405 nm laser, which is in good agreement with the PL spectra shown in Figure 6.2 (j, l), respectively. We would like to emphasize that arbitrary two-dimensional (2D) patterns can be easily accomplished by the DLW. As intuitive evidences, the characters "STU" (Figure 6.4 (c−g)) and different shapes (circles, squares, and triangles in Figure 6.4 (h)) are patterned on different perovskite NPs. The processing resolution is as high as 1 μm, which is higher than the other reported methods with masks.[184-187]

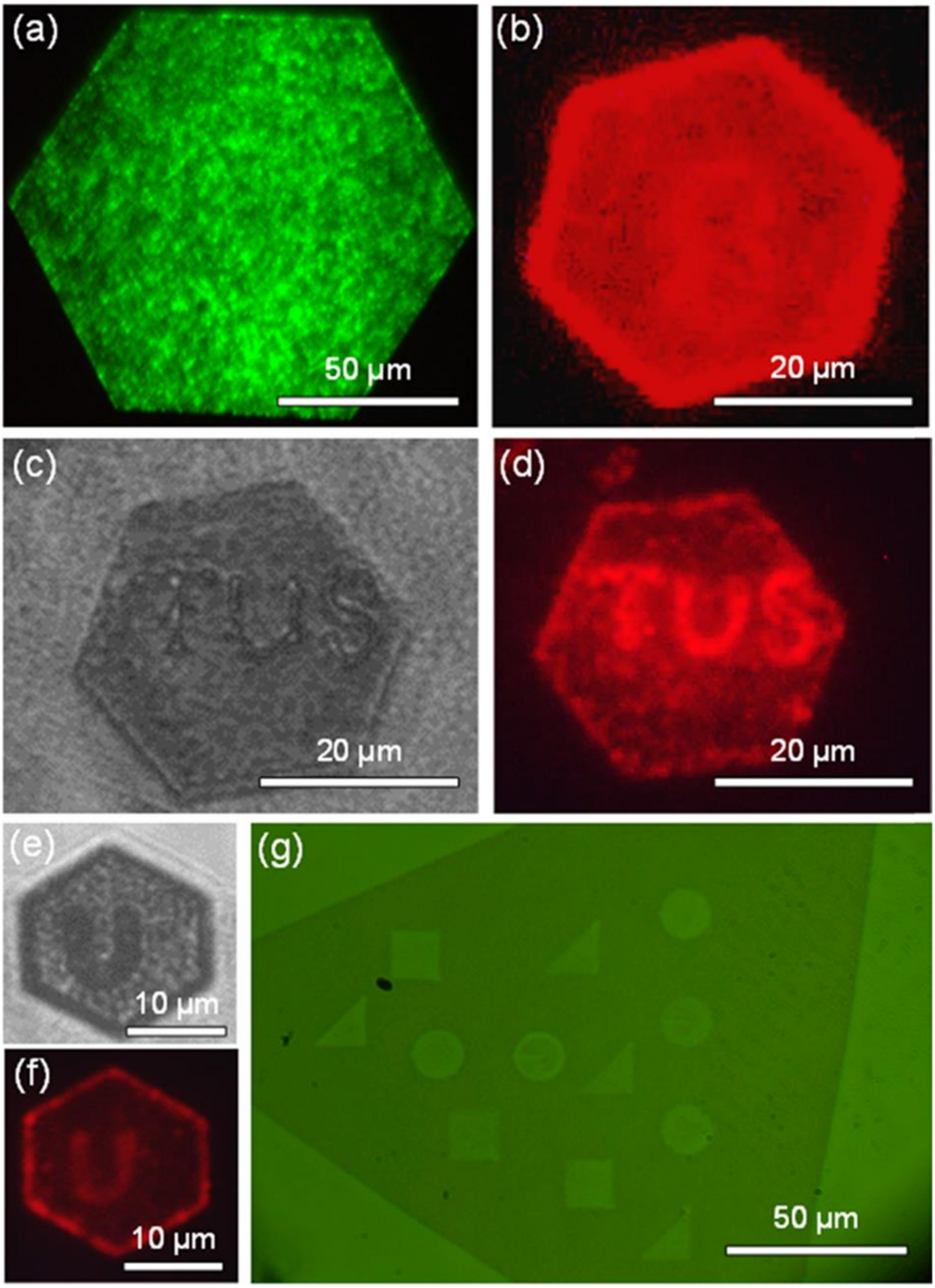

Figure 6.4 (a, b) Fluorescence micrographs of a thin NP (a) and a thick NP (b) without pattern. A 405 nm laser is used as excitation. (c, e) Microscopic images of NPs with laser patterned characters. (d, f) Fluorescence micrographs of the patterned NPs under laser excitation. (g) Microscopic image of a large NP patterned with different shapes by DLW.

6.4.3 spatially modulating the fluorescence color

The spatial modulation of fluorescent color by the fs-DLW is demonstrated in Figure 6.5. A fan-shaped pattern is drawn on a thick NP. As illustrated in Figure 6.5 (a), the blades of the fan are fabricated with gradually increased power (0−150 μW) along the counter-clockwise direction. Figure 6.5 (b) shows AFM image of the thick NP with the fan-shaped pattern, verifying the depth of blades increases along the counter-clockwise direction. The bright-field and fluorescence microscopic images are displayed in Figure 6.5 (c, d), respectively. Two distinguishing fluorescent colors are observed in Figure 6.5 (d). The deep blades exhibit green emission, whereas the surrounding edges are red. Note that the original NPs only contain two halogens; thus, the emission color is limitedly tuned from green to red. If chlorine could be added in the initial CVD reactions, the DLW on ternary mixed halide perovskites is expected to spatially tune the fluorescent color across the entire visible range.

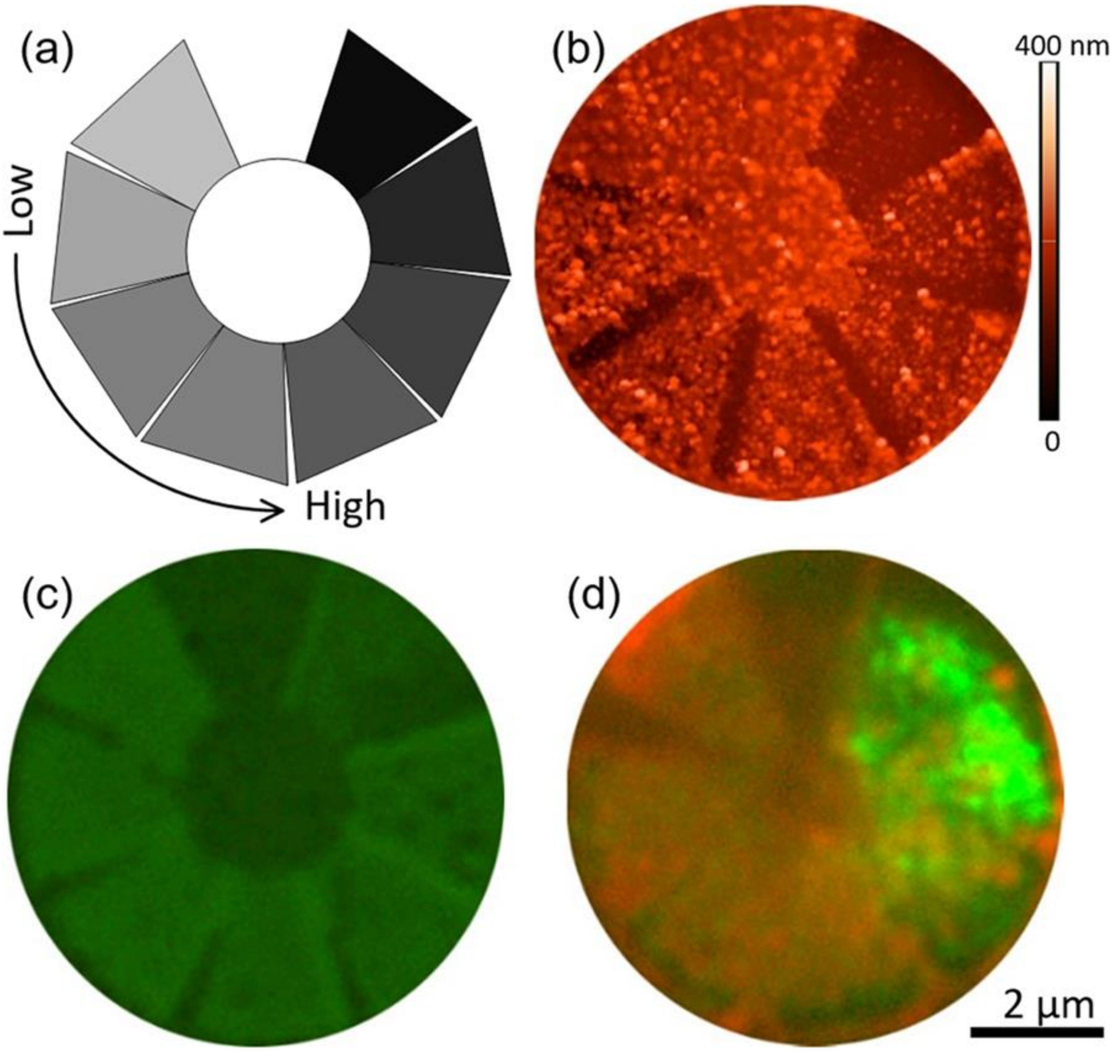

Figure 6.5 (a) Fabrication of a fan-shaped pattern with gradually increased fabrication power. (b) AFM image of the thick NP with a fan-shaped pattern. (c) Bright-field microscopic image of the acquired pattern. (d) Fluorescence micrograph of the NP with a fan-shaped pattern. Two colors are observed.

6.5 Conclusion

In summary, the Experiment mixed-halide compositional gradient FAPb(Br_xI_{1-x})$_3$ perovskite NPs are designed for fs-DLW pattern. When the NP is as thin as 50 nm, the DLW fabricated hole and the as-grown NP display almost the same PL emission, with only one peak at 545 nm corresponding to the pure bromide phase. For the medium NP with a thickness of 150 nm, a PL peak locating at 590 nm of the mixed phase is observed in the as-grown NP. After DLW processing, PL of the holes blue-shifts to 545 nm, implying the substitution reaction is induced by DLW. When a thick NP (thickness ≈ 500 nm) is patterned by DLW, a new peak appears in the wavelength range of 540−600 nm due to anion exchange induced by DLW, in addition to the initial 690 nm emission of the NP. The peak position and intensity are controllable according to the DLW conditions. Thus, the fluorescent color can be modulated from red to green, enabling microscale-resolved multicolor patterns by the straightforward, mask-free, and simple step DLW technique. We demonstrate that arbitrary 2D patterns can be achieved on a range of perovskite NPs.

The work in this chapter has been published in the journal article: Zhou, C.; Cao, G.; Gan, Z.; Ou, Q.; Chen, W.; Bao, Q.; Jia, B.; Wen, X. Spatially Modulating the Fluorescence Color of Mixed-Halide Perovskite Nanoplatelets through Direct Laser Writing. ACS applied materials & interfaces 2019, 11 (29), 26017-26023.[111]

Chapter 7

Conclusions and Future Work

7.1 Conclusions

This work focuses on the fundamental carrier diffusion properties of the organic-inorganic perovskites. A wide range of topics has been covered including the experimental and theoretical methods, the physical understanding of the carrier dynamics, and the application for the on-chip devices. The major achievements can be summarized as follows:

1. The carrier diffusion length is a vital parameter for the photovoltage and optoelectronic applications of organic-inorganic perovskites. However, the determination of carrier diffusion length is a challenge task for 2D layered and 3D thin perovskite NPs. For the first time, a novel method is used to determine the in-plane carrier diffusion in 2D perovskites by taking advantage of the edge trapping state as a natural quenching source for carriers. In 2D perovskites, the photogenerated carriers will diffuse along the in-plane direction due to the quantum confinement in the depth direction. The edge of the platelet acts as a natural quenching source of carriers as the 2D expansion of perovskite layer terminates there. When the exciting spots are closer to the edge of a perovskite NP, the carriers have an increased possibility to diffuse to the edge and are quenched by the edge trapping state. Thus, points with gradual decreased distance to the edge will show a decreased PL lifetime when excited by a pulsed laser. In the other word, the lifetime can be described as a function of the distance between the excitation point and the edge. The relationship between lifetime and the

distance to the edge can be described by a one-direction diffusion model. The diffusion coefficient and diffusion length will thus be extracted. A 2D $(BA)_2PbI_4$ single crystal is investigated; the diffusion length (1.82 µm) and in-plane diffusion coefficient (53.6 cm^2/s) are experimentally extracted.

This method is applicable in 3D perovskite thin flakes, because the edge-trapping states can act as quenching source as well, leading to the carrier directional diffusion in the thin 3D perovskites flakes. The diffusion length / coefficient of a thin $MAPbBr_3$ NP are extracted, within the range of the reported values, rationalizing this method in 3D materials. Another advantage is the method can be applied to low-luminescent samples, as the laser excitation and PL detection are at the same point so that a high PL collection efficiency, together with the very high detection sensitivity of TCSPC method, which requires low excitation intensity for the measurement.

2. Compared to the homogeneous perovskite with a uniform bandgap along the depth, the bandgap engineering provides a possibility to accelerate or suppress the carrier transport; potentially very important for high efficient optoelectronic applications. In the mixed halide perovskite with gradient bandgap, the carriers will flow directionally from high-bandgap region to the low-bandgap region. A gradient bandgap mixed-halide $FAPb(Br_xI_{1-x})_3$ perovskite NP is fabricated by a CVD method. The halide composition is gradually changed from bromide (top) to iodide (bottom) along the depth. Consequently, the gradient bandgap structure is formed by halide substitution during the annealing. The carrier funneling is observed directly from the PL emission wavelength. Under 405 nm laser excitation, the carriers will transfer from the high bandgap bromide region to the low bandgap iodide region and emit. The PL spectra were observed in 735/790 nm, from the iodide-rich regions.

Like other mixed-halide perovskites, the illumination-induced phase segregation phenomenon was observed. The PL spectra exhibit blueshift in Br-rich phases and redshift in I-rich phases under continuous illumination. We demonstrated the irreversible and stable phases are formed, which will improve the compositional uniformity, reduce defect density, and improve the stability of the gradient bandgap structure.

3. Combined with the fs-DLW fabrication technology, the microscale color pattern is achieved in the gradient-bandgap perovskite NP, which is an important step for its on-chip applications. Under the femtosecond direct laser writing, the thickness of perovskite NP decreased. Anion exchange occurs during this process, leading to the fluorescence color change. For instance, a new peak in the wavelength range of 540−600 nm appears, as bromide substitute iodide during the laser fabrication. By controlling the fabrication conditions, different fluorescence colors are shown in the perovskite NP from red to green. Arbitrary 2D patterns are demonstrated by this method. Thus, fluorescence color of mixed-halide perovskite NP can be spatially modulated via the straightforward, mask-free, and simple step fs-DLW technique.

7.2 Future work

Although much progress has been made in understanding the carrier diffusion in perovskites, there are significant more to be further explored.

1. Understanding the diffusion process of the excitons in 2D perovskites would address the mystery of their unexpected success in photovoltaics and develop further optoelectronic applications. Determining and comparing the carrier diffusion length in 2D and quasi-2D perovskites with different n-values may provide a solution. As the n-value increases, more organic-halide octahedron slabs layers are sandwiched between the long-chain organic cations. For 2D perovskites with n = 1, the excitons are confined in one single anionic layer, with the restrict in-plane diffusion direction, as presented in Chapter 4. However, when the n-value increases at 2D /quasi-2D perovskites, more anionic layers are stacked between the organic spacers, leading to a weaker quantum confinement. Moreover, excitons can dissociate near edges in 2D perovskites with n-value larger than 1, which makes the carrier diffusion process more complex. Thus, the determination, calculation, and comparison of diffusion lengths as well as the edge state efforts in these materials are of great importance. Investigation of this project would further help with the understanding of the carrier dynamics of 2D perovskites and the optimization of their applications.

2. The bandgap engineering by halide mixture is a significant exploration. It has been showed such halide mixture results in specific gradient bandgap. The carrier funneling effect and their application by fs laser writing are presented in Chapter 5 and 6. Further bandgap engineering with mixed halides with chloride can cover blue color so it is possible to cover all color. Moreover, organic-inorganic mixture and metal alloy (Cs-MA) and Pb-Sn) will be possible for bandgap tuning. To provide profound knowledge, the carrier diffusion process can be further clarified under the excitation of different energy / wavelength lasers. Our work was focused on the high energy excitation on the gradient-bandgap perovskites, where carriers are excited from the highest bandgap region. However, when selectively excited by a lower energy laser, corresponding to a given depth below the surface, only the relevant lower bandgap regions can be excited, and carriers will diffuse and funneling from the inner part of the perovskite NP. Meanwhile, by changing the excitation intensity, different diffusion phenomenon may show in such gradient-halide perovskite NPs.

3. With tunable optical bandgap, the mixed-halide perovskites are with good optical and electrical properties. However, for the commercial applications, the instability induced by mobile ions is a critical issue to be addressed. The phase segregation and ion migration have negative impacts on the local defect levels for the mixed-halide perovskites. In addition to the energy funneling effects and carrier diffusion process investigated in this thesis, the improvement of stability should be further investigated. For instance, as the stability of 2D perovskites is significantly improved by quantum confinement, merging these two families of perovskites is an interesting scientific task to obtain high-efficiency and stable solar cells.

4. For the commercialization of perovskite solar cells, ensuring intrinsic stability and pursuing higher PCE are of great importance. By combining different cations and halide anions, the mixed perovskites are intrinsically stable. Moreover, as carriers can gradually flow from high to low bandgaps in the gradient-bandgap materials, carriers are effectively collected, which has a potential for high-efficiency solar cells. Using gradient-bandgap mixed-halide perovskite for perovskite solar cells could thus be a topic in the future topic.

Publication Lists

Journal articles:

1. **Zhou, C.;** Ou, Q.; Chen, W.; Gan, Z.; Wang, J.; Bao, Q.; Wen, X.; Jia, B., Illumination - Induced Halide Segregation in Gradient Bandgap Mixed - Halide Perovskite Nanoplatelets. *Advanced Optical Materials* **2018,** *6* (24), 1801107.

2. **Zhou, C.;** Cao, G.; Gan, Z.; Ou, Q.; Chen, W.; Bao, Q.; Jia, B.; Wen, X., Spatially modulating the fluorescence color of mixed-halide perovskite nanoplatelets through direct femtosecond laser writing. *ACS applied materials & interfaces* **2019,** *11* (29), 26017-26023.

3. **Zhou, C.;** Chen, W.; Yang, S.; Ou, Q.; Gan, Z.; Bao, Q.; Jia, B.; Wen, X., Determining In-Plane Carrier Diffusion in Two-Dimensional Perovskite Using Local Time-Resolved Photoluminescence. *ACS Applied Materials & Interfaces* **2020**.

4. Zheng, F.; Zuo, C.; Niu, M.; **Zhou, C.;** Bradley, S. J.; Hall, C. R.; Xu, W.; Wen, X.; Hao, X.; Gao, M.; Smith, T. A.; Ghiggino, K. P., Revealing the Role of Methylammonium Chloride for Improving the Performance of 2D Perovskite Solar Cells. *ACS Applied Materials & Interfaces* **2020**.

5. Gan, Z.; Chen, W.; **Zhou, C.;** Yu, L.; Dong, L.; Jia, B.; Wen, X., Efficient Energy Funnelling by Engineering Bandgap of Perovskite: Förster Resonance Energy Transfer or Charge Transfer? *The Journal of Physical Chemistry Letters* **2020**.

6. Gan, Z.; Zheng, F.; Mao, W.; **Zhou, C**.; Chen, W.; Bach, U.; Tapping, P.; Kee, T. W.; Davis, J. A.; Jia, B.; Wen, X., The optical properties of Cs4PbBr6–CsPbBr3 perovsite composites. *Nanoscale* **2019,** *11* (31), 14676-14683.

7. Gan, Z.; Wen, X.; **Zhou, C.;** Chen, W.; Zheng, F.; Yang, S.; Davis, J. A.; Tapping, P. C.; Kee, T. W.; Zhang, H.; Jia, B., Transient Energy Reservoir in 2D Perovskites. *Advanced Optical Materials* **2019,** *7* (22), 1900971.

8. Gan, Z.; Wen, X.; Chen, W.; **Zhou, C.;** Yang, S.; Cao, G.; Ghiggino, K. P.; Zhang, H.; Jia, B., The Dominant Energy Transport Pathway in Halide Perovskites: Photon Recycling or Carrier Diffusion? *Advanced Energy Materials* **2019**, 1900185.

9. Gan, Z.; Chen, W.; Yuan, L.; Cao, G.; **Zhou, C.;** Huang, S.; Wen, X.; Jia, B., External stokes shift of perovskite nanocrystals enlarged by photon recycling. *Applied Physics Letters* **2019,** *114* (1), 011906.

10. Wen, X.; Chen, W.; Yang, J.; Ou, Q.; Yang, T.; **Zhou, C.;** Lin, H.; Wang, Z.; Zhang, Y.; Conibeer, G.; Bao, Q.; Jia, B.; Moss, D. J., Role of Surface Recombination in Halide Perovskite Nanoplatelets. *ACS Applied Materials & Interfaces* **2018,** *10* (37), 31586-31593.

11. Chen, J.-Y.; Kadam, G.; Gupta, A.; Anuradha; Bhosale, S. V.; Zheng, F.; **Zhou, C.-H.;** Jia, B.-H.; Dalal, D. S.; Li, J.-L., Cover Feature: A Biomimetic Supramolecular Approach for Charge Transfer between Donor and Acceptor Chromophores with Aggregation-Induced Emission (Chem. Eur. J. 55/2018). *Chemistry – A European Journal* **2018,** *24* (55), 14568-14568.

Conferences:

1. **Zhou, C.;** Cao, G.; Gan, Z.; Ou, Q.; Bao, Q.; Jia, B.; Wen, X., *Tuning the florescence color of gradient bandgap perovskite nanoplate by direct laser writing*. SPIE: 2019; Vol. 11201.

2. Chen, W.; Vũ, Y.; **Zhou, C.;** Jia, B.; Wen, X., *Light soak study of perovskite-based materials via scanning imaging spectroscopy*. SPIE: 2019; Vol. 11201.

References

(1) Chakhmouradian, A. R.; Woodward, P. M. Celebrating 175 years of perovskite research: a tribute to Roger H. Mitchell. *Physics and Chemistry of Minerals* **2014,** *41* (6), 387-391.

(2) Kojima, A.; Teshima, K.; Shirai, Y.; Miyasaka, T. Organometal halide perovskites as visible-light sensitizers for photovoltaic cells. *Journal of the American Chemical Society* **2009,** *131* (17), 6050-6051.

(3) Yang, X.; Zhang, X.; Deng, J.; Chu, Z.; Jiang, Q.; Meng, J.; Wang, P.; Zhang, L.; Yin, Z.; You, J. Efficient green light-emitting diodes based on quasi-two-dimensional composition and phase engineered perovskite with surface passivation. *Nature Communications* **2018,** *9* (1), 570.

(4) Jena, A. K.; Kulkarni, A.; Miyasaka, T. Halide perovskite photovoltaics: background, status, and future prospects. *Chemical reviews* **2019,** *119* (5), 3036-3103.

(5) Zhao, Y.-Q.; Ma, Q.-R.; Liu, B.; Yu, Z.-L.; Yang, J.; Cai, M.-Q. Layer-dependent transport and optoelectronic property in two-dimensional perovskite: $(PEA)_2PbI_4$. *Nanoscale* **2018,** *10* (18), 8677-8688.

(6) Herz, L. M. Charge-carrier mobilities in metal halide perovskites: fundamental mechanisms and limits. *ACS Energy Letters* **2017,** *2* (7), 1539-1548.

(7) Peng, J.; Chen, Y.; Zheng, K.; Pullerits, T.; Liang, Z. Insights into charge carrier dynamics in organo-metal halide perovskites: from neat films to solar cells. *Chemical Society Review* **2017,** *46* (19), 5714-5729.

(8) Zhumekenov, A. A.; Saidaminov, M. I.; Haque, M. A.; Alarousu, E.; Sarmah, S. P.; Murali, B.; Dursun, I.; Miao, X.-H.; Abdelhady, A. L.; Wu, T. Formamidinium lead halide perovskite crystals with unprecedented long carrier dynamics and diffusion length. *ACS Energy Letters* **2016,** *1* (1), 32-37.

(9) Shaw, P. E.; Ruseckas, A.; Samuel, I. D. Exciton diffusion measurements in poly (3-hexylthiophene). *Advanced Materials* **2008,** *20* (18), 3516-3520.

(10) Jiang, F.; Liu, T.; Luo, B.; Tong, J.; Qin, F.; Xiong, S.; Li, Z.; Zhou, Y. A two-terminal perovskite/perovskite tandem solar cell. *Journal of Materials Chemistry A* **2016,** *4* (4), 1208-1213.

(11) Tian, W.; Leng, J.; Zhao, C.; Jin, S. Long-Distance Charge Carrier Funneling in Perovskite Nanowires Enabled by Built-in Halide Gradient. *Journal of the American Chemical Society* **2017,** *139* (2), 579-582.

(12) Yuan, M.; Quan, L. N.; Comin, R.; Walters, G.; Sabatini, R.; Voznyy, O.; Hoogland, S.; Zhao, Y.; Beauregard, E. M.; Kanjanaboos, P.; Lu, Z.; Kim, D. H.; Sargent, E. H. Perovskite energy funnels for efficient light-emitting diodes. *Nature Nanotechnology* **2016,** *11* (10), 872-877.

(13) Green, M. A.; Ho-Baillie, A.; Snaith, H. J. The emergence of perovskite solar cells. *Nature Photonics* **2014,** *8* (7), 506-514.
(14) Saparov, B.; Mitzi, D. B. Organic–inorganic perovskites: structural versatility for functional materials design. *Chemical reviews* **2016,** *116* (7), 4558-4596.
(15) Xiao, J.-W.; Liu, L.; Zhang, D.; De Marco, N.; Lee, J.-W.; Lin, O.; Chen, Q.; Yang, Y. The Emergence of the Mixed Perovskites and Their Applications as Solar Cells. *Advanced Energy Materials* **2017,** *7* (20), 1700491.
(16) Zhou, Y.; Zhou, Z.; Chen, M.; Zong, Y.; Huang, J.; Pang, S.; Padture, N. P. Doping and alloying for improved perovskite solar cells. *Journal of Materials Chemistry A* **2016,** *4* (45), 17623-17635.
(17) Albero, J.; Asiri, A. M.; García, H. Influence of the composition of hybrid perovskites on their performance in solar cells. *Journal of Materials Chemistry A* **2016,** *4* (12), 4353-4364.
(18) Zhou, H.; Chen, Q.; Li, G.; Luo, S.; Song, T.-b.; Duan, H.-S.; Hong, Z.; You, J.; Liu, Y.; Yang, Y. Interface engineering of highly efficient perovskite solar cells. *Science* **2014,** *345* (6196), 542-546.
(19) Amat, A.; Mosconi, E.; Ronca, E.; Quarti, C.; Umari, P.; Nazeeruddin, M. K.; Grätzel, M.; De Angelis, F. Cation-Induced Band-Gap Tuning in Organohalide Perovskites: Interplay of Spin–Orbit Coupling and Octahedra Tilting. *Nano Letters* **2014,** *14* (6), 3608-3616.
(20) Stoumpos, C. C.; Cao, D. H.; Clark, D. J.; Young, J.; Rondinelli, J. M.; Jang, J. I.; Hupp, J. T.; Kanatzidis, M. G. Ruddlesden–Popper Hybrid Lead Iodide Perovskite 2D Homologous Semiconductors. *Chemistry of Materials* **2016,** *28* (8), 2852-2867.
(21) Ruddlesden, S. N.; Popper, P. The compound Sr3Ti2O7 and its structure. *Acta Crystallographica* **1958,** *11* (1), 54-55.
(22) Yuan, Z.; Shu, Y.; Xin, Y.; Ma, B. Highly luminescent nanoscale quasi-2D layered lead bromide perovskites with tunable emissions. *Chemical Communications* **2016,** *52* (20), 3887-90.
(23) Kamminga, M. E.; Fang, H.-H.; Filip, M. R.; Giustino, F.; Baas, J.; Blake, G. R.; Loi, M. A.; Palstra, T. T. M. Confinement Effects in Low-Dimensional Lead Iodide Perovskite Hybrids. *Chemistry of Materials* **2016,** *28* (13), 4554-4562.
(24) Knight, A. J.; Herz, L. M. Preventing phase segregation in mixed-halide perovskites: a perspective. *Energy & Environmental Science* **2020,** *13* (7), 2024-2046.
(25) Dong, Q.; Fang, Y.; Shao, Y.; Mulligan, P.; Qiu, J.; Cao, L.; Huang, J. Electron-hole diffusion lengths > 175 μm in solution-grown $CH_3NH_3PbI_3$ single crystals. *Science* **2015,** *347* (6225), 967-970.
(26) Noh, J. H.; Im, S. H.; Heo, J. H.; Mandal, T. N.; Seok, S. I. Chemical management for colorful, efficient, and stable inorganic-organic hybrid nanostructured solar cells. *Nano Letters* **2013,** *13* (4), 1764-9.
(27) You, J.; Meng, L.; Song, T.-B.; Guo, T.-F.; Yang, Y. M.; Chang, W.-H.; Hong, Z.; Chen, H.; Zhou, H.; Chen, Q. Improved air stability of perovskite solar cells via solution-processed metal oxide transport layers. *Nature Nanotechnology* **2016,** *11* (1), 75.
(28) Eperon, G. E.; Beck, C. E.; Snaith, H. J. Cation exchange for thin film lead iodide perovskite interconversion. *Materials Horizons* **2016,** *3* (1), 63-71.
(29) Eames, C.; Frost, J. M.; Barnes, P. R.; O'regan, B. C.; Walsh, A.; Islam, M. S. Ionic transport in hybrid lead iodide perovskite solar cells. *Nature communications* **2015,** *6*, 7497.
(30) Eperon, G. E.; Stranks, S. D.; Menelaou, C.; Johnston, M. B.; Herz, L. M.; Snaith, H. J. Formamidinium lead trihalide: a broadly tunable perovskite for efficient planar

heterojunction solar cells. *Energy & Environmental Science* **2014,** *7* (3), 982.

(31) Hoke, E. T.; Slotcavage, D. J.; Dohner, E. R.; Bowring, A. R.; Karunadasa, H. I.; McGehee, M. D. Reversible photo-induced trap formation in mixed-halide hybrid perovskites for photovoltaics. *Chemical Science* **2015,** *6* (1), 613-617.

(32) Sum, T. C.; Mathews, N. Advancements in perovskite solar cells: photophysics behind the photovoltaics. *Energy & Environmental Science* **2014,** *7* (8), 2518-2534.

(33) Yang, L.; Barrows, A. T.; Lidzey, D. G.; Wang, T. Recent progress and challenges of organometal halide perovskite solar cells. *Reports on Progress in Physics* **2016,** *79* (2), 026501.

(34) Talbert, E. M.; Zarick, H. F.; Boulesbaa, A.; Soetan, N.; Puretzky, A. A.; Geohegan, D. B.; Bardhan, R. Bromine substitution improves excited-state dynamics in mesoporous mixed halide perovskite films. *Nanoscale* **2017,** *9* (33), 12005-12013.

(35) Pitchaiya, S.; Natarajan, M.; Santhanam, A.; Asokan, V.; Yuvapragasam, A.; Madurai Ramakrishnan, V.; Palanisamy, S. E.; Sundaram, S.; Velauthapillai, D. A review on the classification of organic/inorganic/carbonaceous hole transporting materials for perovskite solar cell application. *Arabian Journal of Chemistry* **2020,** *13* (1), 2526-2557.

(36) Fu, F.; Feurer, T.; Jäger, T.; Avancini, E.; Bissig, B.; Yoon, S.; Buecheler, S.; Tiwari, A. N. Low-temperature-processed efficient semi-transparent planar perovskite solar cells for bifacial and tandem applications. *Nature Communications* **2015,** *6*, 8932.

(37) Stranks, S. D.; Snaith, H. J. Metal-halide perovskites for photovoltaic and light-emitting devices. *Nature nanotechnology* **2015,** *10* (5), 391.

(38) Mishima, O.; Era, K.; Tanaka, J.; Yamaoka, S. Ultraviolet light-emitting diode of a cubic boron nitride pn junction made at high pressure. *Applied physics letters* **1988,** *53* (11), 962-964.

(39) Miyata, A.; Mitioglu, A.; Plochocka, P.; Portugall, O.; Wang, J. T.-W.; Stranks, S. D.; Snaith, H. J.; Nicholas, R. J. Direct measurement of the exciton binding energy and effective masses for charge carriers in organic–inorganic tri-halide perovskites. *Nature Physics* **2015,** *11* (7), 582-587.

(40) Xing, J.; Yan, F.; Zhao, Y.; Chen, S.; Yu, H.; Zhang, Q.; Zeng, R.; Demir, H. V.; Sun, X.; Huan, A. High-efficiency light-emitting diodes of organometal halide perovskite amorphous nanoparticles. *ACS nano* **2016,** *10* (7), 6623-6630.

(41) Ahmadi, M.; Wu, T.; Hu, B. A Review on Organic-Inorganic Halide Perovskite Photodetectors: Device Engineering and Fundamental Physics. *Advanced Materials* **2017**.

(42) Hu, X.; Zhang, X.; Liang, L.; Bao, J.; Li, S.; Yang, W.; Xie, Y. High-Performance Flexible Broadband Photodetector Based on Organolead Halide Perovskite. *Advanced Functional Materials* **2014,** *24* (46), 7373-7380.

(43) Liu, J.; Xue, Y.; Wang, Z.; Xu, Z. Q.; Zheng, C.; Weber, B.; Song, J.; Wang, Y.; Lu, Y.; Zhang, Y.; Bao, Q. Two-Dimensional $CH_3NH_3PbI_3$ Perovskite: Synthesis and Optoelectronic Application. *ACS Nano* **2016,** *10* (3), 3536-3542.

(44) Liu, J.; Xue, Y.; Wang, Z.; Xu, Z. Q.; Zheng, C.; Weber, B.; Song, J.; Wang, Y.; Lu, Y.; Zhang, Y.; Bao, Q. Two-Dimensional $CH_3NH_3PbI_3$ Perovskite: Synthesis and Optoelectronic Application. *ACS Nano* **2016,** *10* (3), 3536-42.

(45) Zhang, Y.; Lim, C.-K.; Dai, Z.; Yu, G.; Haus, J. W.; Zhang, H.; Prasad, P. N. Photonics and optoelectronics using nano-structured hybrid perovskite media and their optical cavities. *Physics Reports* **2019,** *795*, 1-51.

(46) Zhu, H.; Fu, Y.; Meng, F.; Wu, X.; Gong, Z.; Ding, Q.; Gustafsson, M. V.; Trinh, M. T.; Jin, S.; Zhu, X. Y. Lead halide perovskite nanowire lasers with low lasing

thresholds and high quality factors. *Nature Materials* **2015,** *14* (6), 636-42.
(47) Schünemann, S.; Brittman, S.; Chen, K.; Garnett, E. C.; Tüysüz, H. Halide Perovskite 3D Photonic Crystals for Distributed Feedback Lasers. *ACS Photonics* **2017,** *4* (10), 2522-2528.
(48) Guo, Z.; Wan, Y.; Yang, M.; Snaider, J.; Zhu, K.; Huang, L. Long-range hot-carrier transport in hybrid perovskites visualized by ultrafast microscopy. *Science* **2017,** *356* (6333), 59-62.
(49) Delport, G.; Macpherson, S.; Stranks, S. D. Imaging carrier transport properties in halide perovskites using time-resolved optical microscopy. *arXiv preprint arXiv:1911.10615* **2019**.
(50) Shi, J.; Li, Y.; Li, Y.; Li, D.; Luo, Y.; Wu, H.; Meng, Q. From Ultrafast to Ultraslow: Charge-Carrier Dynamics of Perovskite Solar Cells. *Joule* **2018,** *2* (5), 879-901.
(51) König, D.; Casalenuovo, K.; Takeda, Y.; Conibeer, G.; Guillemoles, J. F.; Patterson, R.; Huang, L. M.; Green, M. A. Hot carrier solar cells: Principles, materials and design. *Physica E: Low-dimensional Systems and Nanostructures* **2010,** *42* (10), 2862-2866.
(52) Wen, X.; Chen, W.; Yang, J.; Ou, Q.; Yang, T.; Zhou, C.; Lin, H.; Wang, Z.; Zhang, Y.; Conibeer, G.; Bao, Q.; Jia, B.; Moss, D. J. Role of Surface Recombination in Halide Perovskite Nanoplatelets. *ACS Applied Materials & Interfaces* **2018,** *10* (37), 31586-31593.
(53) Gao, F.; Zhao, Y.; Zhang, X.; You, J. Recent Progresses on Defect Passivation toward Efficient Perovskite Solar Cells. *Advanced Energy Materials* **2020,** *10* (13), 1902650.
(54) Li, Q.; Yang, Y.; Que, W.; Lian, T. Size- and Morphology-Dependent Auger Recombination in CsPbBr3 Perovskite Two-Dimensional Nanoplatelets and One-Dimensional Nanorods. *Nano Letters* **2019,** *19* (8), 5620-5627.
(55) Yamada, Y.; Nakamura, T.; Endo, M.; Wakamiya, A.; Kanemitsu, Y. Photocarrier Recombination Dynamics in Perovskite $CH_3NH_3PbI_3$ for Solar Cell Applications. *Journal of the American Chemical Society* **2014,** *136* (33), 11610-11613.
(56) Wen, X.; Feng, Y.; Huang, S.; Huang, F.; Cheng, Y.-B.; Green, M.; Ho-Baillie, A. Defect trapping states and charge carrier recombination in organic–inorganic halide perovskites. *Journal of Materials Chemistry C* **2016,** *4* (4), 793-800.
(57) Gan, Z.; Wen, X.; Chen, W.; Zhou, C.; Yang, S.; Cao, G.; Ghiggino, K. P.; Zhang, H.; Jia, B. The Dominant Energy Transport Pathway in Halide Perovskites: Photon Recycling or Carrier Diffusion? *Advanced Energy Materials* **2019**, 1900185.
(58) Cho, J.; DuBose, J. T.; Kamat, P. V. Charge Carrier Recombination Dynamics of Two-Dimensional Lead Halide Perovskites. *The Journal of Physical Chemistry Letters* **2020,** *11* (7), 2570-2576.
(59) Blancon, J. C.; Stier, A. V.; Tsai, H.; Nie, W.; Stoumpos, C. C.; Traoré, B.; Pedesseau, L.; Kepenekian, M.; Katsutani, F.; Noe, G. T.; Kono, J.; Tretiak, S.; Crooker, S. A.; Katan, C.; Kanatzidis, M. G.; Crochet, J. J.; Even, J.; Mohite, A. D. Scaling law for excitons in 2D perovskite quantum wells. *Nature Communications* **2018,** *9* (1), 2254.
(60) Draguta, S.; Sharia, O.; Yoon, S. J.; Brennan, M. C.; Morozov, Y. V.; Manser, J. S.; Kamat, P. V.; Schneider, W. F.; Kuno, M. Rationalizing the light-induced phase separation of mixed halide organic-inorganic perovskites. *Nature Communications* **2017,** *8* (1), 200.
(61) Rehman, W.; Milot, R. L.; Eperon, G. E.; Wehrenfennig, C.; Boland, J. L.; Snaith, H. J.; Johnston, M. B.; Herz, L. M. Charge-Carrier Dynamics and Mobilities in Formamidinium Lead Mixed-Halide Perovskites. *Advanced Materials* **2015,** *27* (48),

7938-44.

(62) Slotcavage, D. J.; Karunadasa, H. I.; McGehee, M. D. Light-Induced Phase Segregation in Halide-Perovskite Absorbers. *ACS Energy Letters* **2016,** *1* (6), 1199-1205.

(63) Barker, A. J.; Sadhanala, A.; Deschler, F.; Gandini, M.; Senanayak, S. P.; Pearce, P. M.; Mosconi, E.; Pearson, A. J.; Wu, Y.; Srimath Kandada, A. R.; Leijtens, T.; De Angelis, F.; Dutton, S. E.; Petrozza, A.; Friend, R. H. Defect-Assisted Photoinduced Halide Segregation in Mixed-Halide Perovskite Thin Films. *ACS Energy Letters* **2017,** *2* (6), 1416-1424.

(64) Yoon, S. J.; Draguta, S.; Manser, J. S.; Sharia, O.; Schneider, W. F.; Kuno, M.; Kamat, P. V. Tracking Iodide and Bromide Ion Segregation in Mixed Halide Lead Perovskites during Photoirradiation. *ACS Energy Letters* **2016,** *1* (1), 290-296.

(65) Tang, X.; van den Berg, M.; Gu, E.; Horneber, A.; Matt, G. J.; Osvet, A.; Meixner, A. J.; Zhang, D.; Brabec, C. J. Local Observation of Phase Segregation in Mixed-Halide Perovskite. *Nano Letters* **2018,** *18* (3), 2172-2178.

(66) Pellet, N.; Teuscher, J.; Maier, J.; Grätzel, M. Transforming Hybrid Organic Inorganic Perovskites by Rapid Halide Exchange. *Chemistry of Materials* **2015,** *27* (6), 2181-2188.

(67) Manser, J. S.; Kamat, P. V. Band filling with free charge carriers in organometal halide perovskites. *Nature Photonics* **2014,** *8* (9), 737-743.

(68) Tian, W.; Zhao, C.; Leng, J.; Cui, R.; Jin, S. Visualizing Carrier Diffusion in Individual Single-Crystal Organolead Halide Perovskite Nanowires and Nanoplates. *Journal of the American Chemical Society* **2015,** *137* (39), 12458-12461.

(69) Stranks, S. D.; Eperon, G. E.; Grancini, G.; Menelaou, C.; Alcocer, M. J.; Leijtens, T.; Herz, L. M.; Petrozza, A.; Snaith, H. J. Electron-hole diffusion lengths exceeding 1 micrometer in an organometal trihalide perovskite absorber. *Science* **2013,** *342* (6156), 341-344.

(70) Tsai, H.; Nie, W.; Blancon, J. C.; Stoumpos, C. C.; Asadpour, R.; Harutyunyan, B.; Neukirch, A. J.; Verduzco, R.; Crochet, J. J.; Tretiak, S.; Pedesseau, L.; Even, J.; Alam, M. A.; Gupta, G.; Lou, J.; Ajayan, P. M.; Bedzyk, M. J.; Kanatzidis, M. G. High-efficiency two-dimensional Ruddlesden-Popper perovskite solar cells. *Nature* **2016,** *536* (7616), 312-6.

(71) Milot, R. L.; Sutton, R. J.; Eperon, G. E.; Haghighirad, A. A.; Martinez Hardigree, J.; Miranda, L.; Snaith, H. J.; Johnston, M. B.; Herz, L. M. Charge-Carrier Dynamics in 2D Hybrid Metal-Halide Perovskites. *Nano Letters* **2016,** *16* (11), 7001-7007.

(72) deQuilettes, D. W.; Vorpahl, S. M.; Stranks, S. D.; Nagaoka, H.; Eperon, G. E.; Ziffer, M. E.; Snaith, H. J.; Ginger, D. S. Solar cells. Impact of microstructure on local carrier lifetime in perovskite solar cells. *Science* **2015,** *348* (6235), 683-6.

(73) de Quilettes, D. W.; Vorpahl, S. M.; Stranks, S. D.; Nagaoka, H.; Eperon, G. E.; Ziffer, M. E.; Snaith, H. J.; Ginger, D. S. Impact of microstructure on local carrier lifetime in perovskite solar cells. *Science* **2015,** *348* (6235), 683-686.

(74) Dou, L.; Lai, M.; Kley, C. S.; Yang, Y.; Bischak, C. G.; Zhang, D.; Eaton, S. W.; Ginsberg, N. S.; Yang, P. Spatially resolved multicolor CsPbX3 nanowire heterojunctions via anion exchange. *Proceedings of the National Academy of Sciences* **2017,** *114* (28), 7216-7221.

(75) Cao, G.; Gan, X.; Lin, H.; Jia, B. An accurate design of graphene oxide ultrathin flat lens based on Rayleigh-Sommerfeld theory. *Opto-Electronic Advances* **2018,** *1* (7), 18001201-18001207.

(76) Zheng, X.; Jia, B.; Lin, H.; Qiu, L.; Li, D.; Gu, M. Highly efficient and ultra-broadband graphene oxide ultrathin lenses with three-dimensional subwavelength

focusing. *Nature Communications* **2015,** *6*, 8433.
(77) Novoselov, K.; Mishchenko, A.; Carvalho, A.; Neto, A. C. 2D materials and van der Waals heterostructures. *Science* **2016,** *353* (6298), aac9439.
(78) Tan, Z.-K.; Moghaddam, R. S.; Lai, M. L.; Docampo, P.; Higler, R.; Deschler, F.; Price, M.; Sadhanala, A.; Pazos, L. M.; Credgington, D. Bright light-emitting diodes based on organometal halide perovskite. *Nature Nanotechnology* **2014,** *9* (9), 687-692.
(79) Zhao, Y.; Qiu, Y.; Gao, H.; Feng, J.; Chen, G.; Jiang, L.; Wu, Y. Layered-Perovskite Nanowires with Long-Range Orientational Order for Ultrasensitive Photodetectors. *Advanced Materials* **2020,** *32* (9), 1905298.
(80) Gao, H.; Feng, J.; Pi, Y.; Zhou, Z.; Zhang, B.; Wu, Y.; Wang, X.; Jiang, X.; Jiang, L. Bandgap Engineering of Single-Crystalline Perovskite Arrays for High-Performance Photodetectors. *Advanced Functional Materials* **2018,** *28* (46), 1804349.
(81) Smith, I. C.; Hoke, E. T.; Solis-Ibarra, D.; McGehee, M. D.; Karunadasa, H. I. A layered hybrid perovskite solar-cell absorber with enhanced moisture stability. *Angewandte Chemie International Edition* **2014,** *53* (42), 11232-5.
(82) Safdari, M.; Svensson, P. H.; Hoang, M. T.; Oh, I.; Kloo, L.; Gardner, J. M. Layered 2D alkyldiammonium lead iodide perovskites: synthesis, characterization, and use in solar cells. *Journal of Materials Chemistry A* **2016,** *4* (40), 15638-15646.
(83) Byun, J.; Cho, H.; Wolf, C.; Jang, M.; Sadhanala, A.; Friend, R. H.; Yang, H.; Lee, T. W. Efficient Visible Quasi-2D Perovskite Light-Emitting Diodes. *Advanced Materials* **2016,** *28* (34), 7515-20.
(84) Zhang, X.; Wu, G.; Yang, S.; Fu, W.; Zhang, Z.; Chen, C.; Liu, W.; Yan, J.; Yang, W.; Chen, H. Vertically Oriented 2D Layered Perovskite Solar Cells with Enhanced Efficiency and Good Stability. *Small* **2017,** *13* (33), 1700611.
(85) Xing, G.; Mathews, N.; Sun, S.; Lim, S. S.; Lam, Y. M.; Gratzel, M.; Mhaisalkar, S.; Sum, T. C. Long-range balanced electron- and hole-transport lengths in organic-inorganic CH3NH3PbI3. *Science* **2013,** *342* (6156), 344-7.
(86) Hutter, E. M.; Eperon, G. E.; Stranks, S. D.; Savenije, T. J. Charge carriers in planar and meso-structured organic–inorganic perovskites: mobilities, lifetimes, and concentrations of trap states. *The Journal of Physical Chemistry Letters* **2015,** *6* (15), 3082-3090.
(87) Guo, Z.; Manser, J. S.; Wan, Y.; Kamat, P. V.; Huang, L. Spatial and temporal imaging of long-range charge transport in perovskite thin films by ultrafast microscopy. *Nature communications* **2015,** *6*, 7471.
(88) Dou, L.; Wong, A. B.; Yu, Y.; Lai, M.; Kornienko, N.; Eaton, S. W.; Fu, A.; Bischak, C. G.; Ma, J.; Ding, T. Atomically thin two-dimensional organic-inorganic hybrid perovskites. *Science* **2015,** *349* (6255), 1518-1521.
(89) Bao, J.; Hadjiev, V. G. Origin of Luminescent Centers and Edge States in Low-Dimensional Lead Halide Perovskites: Controversies, Challenges and Instructive Approaches. *Nano-Micro Letters* **2019,** *11* (1), 26.
(90) Chen, Y.; Sun, Y.; Peng, J.; Tang, J.; Zheng, K.; Liang, Z. 2D Ruddlesden–Popper Perovskites for Optoelectronics. *Advanced Materials* **2018,** *30* (2), 1703487.
(91) Straus, D. B.; Kagan, C. R. Electrons, Excitons, and Phonons in Two-Dimensional Hybrid Perovskites: Connecting Structural, Optical, and Electronic Properties. *The Journal of Physical Chemistry Letters* **2018,** *9* (6), 1434-1447.
(92) Cheng, B.; Li, T.-Y.; Wei, P.-C.; Yin, J.; Ho, K.-T.; Retamal, J. R. D.; Mohammed, O. F.; He, J.-H. Layer-edge device of two-dimensional hybrid perovskites. *Nature Communications* **2018,** *9* (1), 5196.
(93) Cao, D. H.; Stoumpos, C. C.; Farha, O. K.; Hupp, J. T.; Kanatzidis, M. G. 2D Homologous Perovskites as Light-Absorbing Materials for Solar Cell Applications.

Journal of the American Chemical Society **2015,** *137* (24), 7843-7850.
(94) Wenger, B.; Nayak, P. K.; Wen, X.; Kesava, S. V.; Noel, N. K.; Snaith, H. J. Consolidation of the optoelectronic properties of $CH_3NH_3PbBr_3$ perovskite single crystals. *Nature Communications* **2017,** *8* (1), 590.
(95) Leng, K.; Fu, W.; Liu, Y.; Chhowalla, M.; Loh, K. P. From bulk to molecularly thin hybrid perovskites. *Nature Reviews Materials* **2020**.
(96) Feng, J.; Gong, C.; Gao, H.; Wen, W.; Gong, Y.; Jiang, X.; Zhang, B.; Wu, Y.; Wu, Y.; Fu, H. Single-crystalline layered metal-halide perovskite nanowires for ultrasensitive photodetectors. *Nature Electronics* **2018,** *1* (7), 404.
(97) Shi, E.; Deng, S.; Yuan, B.; Gao, Y.; Akriti; Yuan, L.; Davis, C. S.; Zemlyanov, D.; Yu, Y.; Huang, L.; Dou, L. Extrinsic and Dynamic Edge States of Two-Dimensional Lead Halide Perovskites. *ACS Nano* **2019,** *13* (2), 1635-1644.
(98) Chen, W.; Wen, X.; Yang, J.; Latzel, M.; Patterson, R.; Huang, S.; Shrestha, S.; Jia, B.; Moss, D. J.; Christiansen, S.; Conibeer, G. Free charges versus excitons: photoluminescence investigation of InGaN/GaN multiple quantum well nanorods and their planar counterparts. *Nanoscale* **2018,** *10* (11), 5358-5365.
(99) Saidaminov, M. I.; Mohammed, O. F.; Bakr, O. M. Low-dimensional-networked metal halide perovskites: the next big thing. *ACS Energy Letters* **2017,** *2* (4), 889-896.
(100) Slavney, A. H.; Smaha, R. W.; Smith, I. C.; Jaffe, A.; Umeyama, D.; Karunadasa, H. I. Chemical approaches to addressing the instability and toxicity of lead–halide perovskite absorbers. *Inorganic Chemistry* **2016,** *56* (1), 46-55.
(101) Kato, Y.; Ichii, D.; Ohashi, K.; Kunugita, H.; Ema, K.; Tanaka, K.; Takahashi, T.; Kondo, T. Extremely large binding energy of biexcitons in an organic–inorganic quantum-well material (C4H9NH3) 2PbBr4. *Solid State Communications* **2003,** *128* (1), 15-18.
(102) Ramvall, P.; Tanaka, S.; Nomura, S.; Riblet, P.; Aoyagi, Y. Observation of confinement-dependent exciton binding energy of GaN quantum dots. *Applied Physics Letters* **1998,** *73* (8), 1104-1106.
(103) Blancon, J.-C.; Tsai, H.; Nie, W.; Stoumpos, C. C.; Pedesseau, L.; Katan, C.; Kepenekian, M.; Soe, C. M. M.; Appavoo, K.; Sfeir, M. Y. Extremely efficient internal exciton dissociation through edge states in layered 2D perovskites. *Science* **2017**, eaal4211.
(104) Shi, D.; Adinolfi, V.; Comin, R.; Yuan, M.; Alarousu, E.; Buin, A.; Chen, Y.; Hoogland, S.; Rothenberger, A.; Katsiev, K. Low trap-state density and long carrier diffusion in organolead trihalide perovskite single crystals. *Science* **2015,** *347* (6221), 519-522.
(105) Zheng, F.; Wen, X.; Bu, T.; Chen, S.; Yang, J.; Chen, W.; Huang, F.; Cheng, Y.; Jia, B. Slow Response of Carrier Dynamics in Perovskite Interface upon Illumination. *ACS Applied Materials & Interfaces* **2018,** *10* (37), 31452-31461.
(106) Chen, S.; Wen, X.; Yun, J. S.; Huang, S.; Green, M.; Jeon, N. J.; Yang, W. S.; Noh, J. H.; Seo, J.; Seok, S. I.; Ho-Baillie, A. Spatial Distribution of Lead Iodide and Local Passivation on Organo-Lead Halide Perovskite. *ACS Applied Materials & Interfaces* **2017,** *9* (7), 6072-6078.
(107) Sproul, A. B. Dimensionless solution of the equation describing the effect of surface recombination on carrier decay in semiconductors. *Journal of Applied Physics* **1994,** *76* (5), 2851-2854.
(108) Wang, J.; Fu, W.; Jariwala, S.; Sinha, I.; Jen, A. K. Y.; Ginger, D. S. Reducing Surface Recombination Velocities at the Electrical Contacts Will Improve Perovskite Photovoltaics. *ACS Energy Letters* **2019,** *4* (1), 222-227.
(109) Bailie, C. D.; Christoforo, M. G.; Mailoa, J. P.; Bowring, A. R.; Unger, E. L.;

Nguyen, W. H.; Burschka, J.; Pellet, N.; Lee, J. Z.; Grätzel, M. Semi-transparent perovskite solar cells for tandems with silicon and CIGS. *Energy & Environmental Science* **2015,** *8* (3), 956-963.

(110) Deng, S.; Shi, E.; Yuan, L.; Jin, L.; Dou, L.; Huang, L. Long-range exciton transport and slow annihilation in two-dimensional hybrid perovskites. *Nature Communications* **2020,** *11* (1), 664.

(111) Zhou, C.; Cao, G.; Gan, Z.; Ou, Q.; Chen, W.; Bao, Q.; Jia, B.; Wen, X. Spatially modulating the fluorescence color of mixed-halide perovskite nanoplatelets through direct femtosecond laser writing. *ACS Applied Materials & Interfaces* **2019,** *11* (29), 26017-26023.

(112) Zheng, F.; Chen, W.; Bu, T.; Ghiggino, K. P.; Huang, F.; Cheng, Y.; Tapping, P.; Kee, T. W.; Jia, B.; Wen, X. Triggering the Passivation Effect of Potassium Doping in Mixed‐Cation Mixed‐Halide Perovskite by Light Illumination. *Advanced Energy Materials* **2019**, 1901016.

(113) Mikhnenko, O. V.; Azimi, H.; Scharber, M.; Morana, M.; Blom, P. W.; Loi, M. A. Exciton diffusion length in narrow bandgap polymers. *Energy & Environmental Science* **2012,** *5* (5), 6960-6965.

(114) Vörös, Z.; Balili, R.; Snoke, D.; Pfeiffer, L.; West, K. Long-distance diffusion of excitons in double quantum well structures. *Physical Review Letters* **2005,** *94* (22), 226401.

(115) Ivanov, A. Quantum diffusion of dipole-oriented indirect excitons in coupled quantum wells. *Europhysics Letters* **2002,** *59* (4), 586.

(116) Zhu, H.; Trinh, M. T.; Wang, J.; Fu, Y.; Joshi, P. P.; Miyata, K.; Jin, S.; Zhu, X. Y. Organic cations might not be essential to the remarkable properties of band edge carriers in lead halide perovskites. *Advanced Materials* **2017,** *29* (1), 1603072.

(117) Cuevas, A.; Basore, P. A.; Giroult‐Matlakowski, G.; Dubois, C. Surface recombination velocity of highly doped n‐type silicon. *Journal of Applied Physics* **1996,** *80* (6), 3370-3375.

(118) Wei, H.; Fang, Y.; Mulligan, P.; Chuirazzi, W.; Fang, H.-H.; Wang, C.; Ecker, B. R.; Gao, Y.; Loi, M. A.; Cao, L. Sensitive X-ray detectors made of methylammonium lead tribromide perovskite single crystals. *Nature Photonics* **2016,** *10* (5), 333.

(119) Zhou, C.; Chen, W.; Yang, S.; Ou, Q.; Gan, Z.; Bao, Q.; Jia, B.; Wen, X. Determining In-Plane Carrier Diffusion in Two-Dimensional Perovskite Using Local Time-Resolved Photoluminescence. *ACS Applied Materials & Interfaces* **2020,** *12* (23), 26384-26390.

(120) Xu, W.-L.; Niu, M.-S.; Yang, X.-Y.; Yuan, H.-C.; Xiong, C.; Zhu, X.-F.; Hao, X.-T. Aqueous self-assembled perovskite microfibers for sensitive photodetectors. *Organic Electronics* **2017,** *48*, 106-111.

(121) Saliba, M.; Matsui, T.; Domanski, K.; Seo, J.-Y.; Ummadisingu, A.; Zakeeruddin, S. M.; Correa-Baena, J.-P.; Tress, W. R.; Abate, A.; Hagfeldt, A. Incorporation of rubidium cations into perovskite solar cells improves photovoltaic performance. *Science* **2016,** *354* (6309), 206-209.

(122) Noh, J. H.; Im, S. H.; Heo, J. H.; Mandal, T. N.; Seok, S. I. Chemical management for colorful, efficient, and stable inorganic-organic hybrid nanostructured solar cells. *Nano Letters* **2013,** *13* (4), 1764-9.

(123) Boix, P. P.; Agarwala, S.; Koh, T. M.; Mathews, N.; Mhaisalkar, S. G. Perovskite Solar Cells: Beyond Methylammonium Lead Iodide. *The Journal of Physical Chemistry Letters* **2015,** *6* (5), 898-907.

(124) Li, W.; Rothmann, M. U.; Liu, A.; Wang, Z.; Zhang, Y.; Pascoe, A. R.; Lu, J.;

Jiang, L.; Chen, Y.; Huang, F.; Peng, Y.; Bao, Q.; Etheridge, J.; Bach, U.; Cheng, Y.-B. Phase Segregation Enhanced Ion Movement in Efficient Inorganic $CsPbIBr_2$Solar Cells. *Advanced Energy Materials* **2017,** *7* (20), 1700946.

(125) Rehman, W.; Milot, R. L.; Eperon, G. E.; Wehrenfennig, C.; Boland, J. L.; Snaith, H. J.; Johnston, M. B.; Herz, L. M. Charge‐carrier dynamics and mobilities in formamidinium lead mixed‐halide perovskites. *Advanced Materials* **2015,** *27* (48), 7938-7944.

(126) Leijtens, T.; Lauber, B.; Eperon, G. E.; Stranks, S. D.; Snaith, H. J. The importance of perovskite pore filling in organometal mixed halide sensitized TiO2-based solar cells. *The journal of physical chemistry letters* **2014,** *5* (7), 1096-1102.

(127) Tong, G.; Li, H.; Li, G.; Zhang, T.; Li, C.; Yu, L.; Xu, J.; Jiang, Y.; Shi, Y.; Chen, K. Mixed cation perovskite solar cells by stack-sequence chemical vapor deposition with self-passivation and gradient absorption layer. *Nano Energy* **2018,** *48*, 536-542.

(128) Vashishtha, P.; Halpert, J. E. Field-Driven Ion Migration and Color Instability in Red-Emitting Mixed Halide Perovskite Nanocrystal Light-Emitting Diodes. *Chemistry of Materials* **2017,** *29* (14), 5965-5973.

(129) Zhang, T.; Chen, H.; Bai, Y.; Xiao, S.; Zhu, L.; Hu, C.; Xue, Q.; Yang, S. Understanding the relationship between ion migration and the anomalous hysteresis in high-efficiency perovskite solar cells: A fresh perspective from halide substitution. *Nano Energy* **2016,** *26*, 620-630.

(130) Chen, S.; Wen, X.; Sheng, R.; Huang, S.; Deng, X.; Green, M. A.; Ho-Baillie, A. Mobile Ion Induced Slow Carrier Dynamics in Organic-Inorganic Perovskite CH(3)NH(3)PbBr(3). *ACS Applied Materials & Interfaces* **2016,** *8* (8), 5351-7.

(131) Braly, I. L.; Stoddard, R. J.; Rajagopal, A.; Uhl, A. R.; Katahara, J. K.; Jen, A. K.-Y.; Hillhouse, H. W. Current-Induced Phase Segregation in Mixed Halide Hybrid Perovskites and its Impact on Two-Terminal Tandem Solar Cell Design. *ACS Energy Letters* **2017,** *2* (8), 1841-1847.

(132) Ou, Q.; Zhang, Y.; Wang, Z.; Yuwono, J. A.; Wang, R.; Dai, Z.; Li, W.; Zheng, C.; Xu, Z. Q.; Qi, X.; Duhm, S.; Medhekar, N. V.; Zhang, H.; Bao, Q. Strong Depletion in Hybrid Perovskite p-n Junctions Induced by Local Electronic Doping. *Advanced Materials* **2018,** *30* (15), e1705792.

(133) Li, P.; Chen, Y.; Yang, T.; Wang, Z.; Lin, H.; Xu, Y.; Li, L.; Mu, H.; Shivananju, B. N.; Zhang, Y.; Zhang, Q.; Pan, A.; Li, S.; Tang, D.; Jia, B.; Zhang, H.; Bao, Q. Two-Dimensional $CH_3NH_3PbI_3$ Perovskite Nanosheets for Ultrafast Pulsed Fiber Lasers. *ACS Applied Materials & Interfaces* **2017,** *9* (14), 12759-12765.

(134) Jang, D. M.; Park, K.; Kim, D. H.; Park, J.; Shojaei, F.; Kang, H. S.; Ahn, J.-P.; Lee, J. W.; Song, J. K. Reversible halide exchange reaction of organometal trihalide perovskite colloidal nanocrystals for full-range band gap tuning. *Nano Letters* **2015,** *15* (8), 5191-5199.

(135) He, X.; Liu, P.; Wu, S.; Liao, Q.; Yao, J.; Fu, H. Multi-color perovskite nanowire lasers through kinetically controlled solution growth followed by gas-phase halide exchange. *Journal of Materials Chemistry C* **2017,** *5* (48), 12707-12713.

(136) Bischak, C. G.; Sanehira, E. M.; Precht, J. T.; Luther, J. M.; Ginsberg, N. S. Heterogeneous Charge Carrier Dynamics in Organic-Inorganic Hybrid Materials: Nanoscale Lateral and Depth-Dependent Variation of Recombination Rates in Methylammonium Lead Halide Perovskite Thin Films. *Nano Letters* **2015,** *15* (7), 4799-807.

(137) Chen, W.; Wen, X.; Latzel, M.; Heilmann, M.; Yang, J.; Dai, X.; Huang, S.; Shrestha, S.; Patterson, R.; Christiansen, S.; Conibeer, G. Nanoscale Characterization

of Carrier Dynamic and Surface Passivation in InGaN/GaN Multiple Quantum Wells on GaN Nanorods. *ACS Applied Materials & Interfaces* **2016,** *8* (46), 31887-31893.

(138) Zhang, J.; Yang, X.; Deng, H.; Qiao, K.; Farooq, U.; Ishaq, M.; Yi, F.; Liu, H.; Tang, J.; Song, H. Low-dimensional halide perovskites and their advanced optoelectronic applications. *Nano-Micro Letters* **2017,** *9* (3), 36.

(139) Sheng, R.; Ho-Baillie, A.; Huang, S.; Chen, S.; Wen, X.; Hao, X.; Green, M. A. Methylammonium Lead Bromide Perovskite-Based Solar Cells by Vapor-Assisted Deposition. *The Journal of Physical Chemistry C* **2015,** *119* (7), 3545-3549.

(140) Fan, J.; Jia, B.; Gu, M. Perovskite-based low-cost and high-efficiency hybrid halide solar cells. *Photonics Research* **2014,** *2* (5), 111-120.

(141) Gratia, P.; Grancini, G.; Audinot, J. N.; Jeanbourquin, X.; Mosconi, E.; Zimmermann, I.; Dowsett, D.; Lee, Y.; Gratzel, M.; De Angelis, F.; Sivula, K.; Wirtz, T.; Nazeeruddin, M. K. Intrinsic Halide Segregation at Nanometer Scale Determines the High Efficiency of Mixed Cation/Mixed Halide Perovskite Solar Cells. *Journal of the American Chemical Society* **2016,** *138* (49), 15821-15824.

(142) Brivio, F.; Caetano, C.; Walsh, A. Thermodynamic Origin of Photoinstability in the CH3NH3Pb(I1-xBrx)3 Hybrid Halide Perovskite Alloy. *The Journal of Physical Chemistry Letters* **2016,** *7* (6), 1083-7.

(143) Pazos-Outón, L. M.; Szumilo, M.; Lamboll, R.; Richter, J. M.; Crespo-Quesada, M.; Abdi-Jalebi, M.; Beeson, H. J.; Vrućinić, M.; Alsari, M.; Snaith, H. J. Photon recycling in lead iodide perovskite solar cells. *Science* **2016,** *351* (6280), 1430-1433.

(144) Wen, X.; Ho-Baillie, A.; Huang, S.; Sheng, R.; Chen, S.; Ko, H. C.; Green, M. A. Mobile Charge-Induced Fluorescence Intermittency in Methylammonium Lead Bromide Perovskite. *Nano Letters* **2015,** *15* (7), 4644-9.

(145) Park, M.; Neukirch, A. J.; Reyes-Lillo, S. E.; Lai, M.; Ellis, S. R.; Dietze, D.; Neaton, J. B.; Yang, P.; Tretiak, S.; Mathies, R. A. Excited-state vibrational dynamics toward the polaron in methylammonium lead iodide perovskite. *Nature Communications* **2018,** *9* (1), 2525.

(146) Draguta, S.; Sharia, O.; Yoon, S. J.; Brennan, M. C.; Morozov, Y. V.; Manser, J. S.; Kamat, P. V.; Schneider, W. F.; Kuno, M. Rationalizing the light-induced phase separation of mixed halide organic-inorganic perovskites. *Nature Communications* **2017,** *8* (1), 200.

(147) Yang, J.; Wen, X.; Xia, H.; Sheng, R.; Ma, Q.; Kim, J.; Tapping, P.; Harada, T.; Kee, T. W.; Huang, F.; Cheng, Y. B.; Green, M.; Ho-Baillie, A.; Huang, S.; Shrestha, S.; Patterson, R.; Conibeer, G. Acoustic-optical phonon up-conversion and hot-phonon bottleneck in lead-halide perovskites. *Nature Communications* **2017,** *8*, 14120.

(148) Wright, A. D.; Verdi, C.; Milot, R. L.; Eperon, G. E.; Perez-Osorio, M. A.; Snaith, H. J.; Giustino, F.; Johnston, M. B.; Herz, L. M. Electron-phonon coupling in hybrid lead halide perovskites. *Nature Communications* **2016,** *7*, DOI: 10.1038/ncomms11755.

(149) Ball, J. M.; Petrozza, A. Defects in perovskite-halides and their effects in solar cells. *Nature Energy* **2016,** *1* (11), 16149.

(150) Chatterjee, S.; Pal, A. J. Influence of metal substitution on hybrid halide perovskites: towards lead-free perovskite solar cells. *Journal of Materials Chemistry A* **2018,** *6* (9), 3793-3823.

(151) Bischak, C. G.; Hetherington, C. L.; Wu, H.; Aloni, S.; Ogletree, D. F.; Limmer, D. T.; Ginsberg, N. S. Origin of Reversible Photoinduced Phase Separation in Hybrid Perovskites. *Nano Letters* **2017,** *17* (2), 1028-1033.

(152) Chen, S.; Wen, X.; Huang, S.; Huang, F.; Cheng, Y.-B.; Green, M.; Ho-Baillie, A. Light Illumination Induced Photoluminescence Enhancement and Quenching in Lead Halide Perovskite. *Solar RRL* **2017,** *1* (1), 1600001.

(153) Deng, X.; Wen, X.; Lau, C. F. J.; Young, T.; Yun, J.; Green, M. A.; Huang, S.; Ho-Baillie, A. W. Y. Electric field induced reversible and irreversible photoluminescence responses in methylammonium lead iodide perovskite. *Journal of Materials Chemistry C* **2016,** *4* (38), 9060-9068.

(154) Zhou, C.; Ou, Q.; Chen, W.; Gan, Z.; Wang, J.; Bao, Q.; Wen, X.; Jia, B. Illumination‐Induced Halide Segregation in Gradient Bandgap Mixed‐Halide Perovskite Nanoplatelets. *Advanced Optical Materials* **2018,** *6* (24), 1801107.

(155) Wen, X.; Sitt, A.; Yu, P.; Ko, H.-c.; Toh, Y.-R.; Tang, J. Studies of the photostability of CdSe/CdS dot-in-rod nanoparticles. *Journal of Nanoparticle Research* **2012,** *14* (12), 1278.

(156) Saliba, M.; Matsui, T.; Seo, J.-Y.; Domanski, K.; Correa-Baena, J.-P.; Nazeeruddin, M. K.; Zakeeruddin, S. M.; Tress, W.; Abate, A.; Hagfeldt, A. Cesium-containing triple cation perovskite solar cells: improved stability, reproducibility and high efficiency. *Energy & Environmental Science* **2016,** *9* (6), 1989-1997.

(157) Gil-Escrig, L. n.; Miquel-Sempere, A.; Sessolo, M.; Bolink, H. J. Mixed iodide–bromide methylammonium Lead perovskite-based diodes for light emission and photovoltaics. *The Journal of Physical Chemistry Letters* **2015,** *6* (18), 3743-3748.

(158) Sadhanala, A.; Ahmad, S.; Zhao, B.; Giesbrecht, N.; Pearce, P. M.; Deschler, F.; Hoye, R. L.; G del, K. C.; Bein, T.; Docampo, P. Blue-green color tunable solution processable organolead chloride–bromide mixed halide perovskites for optoelectronic applications. *Nano Letters* **2015,** *15* (9), 6095-6101.

(159) Kumawat, N. K.; Dey, A.; Kumar, A.; Gopinathan, S. P.; Narasimhan, K.; Kabra, D. Band Gap Tuning of $CH_3NH_3Pb(Br_{1-x}Cl_x)_3$ Hybrid Perovskite for Blue Electroluminescence. *ACS Applied Materials & Interfaces* **2015,** *7* (24), 13119-13124.

(160) Sadhanala, A.; Deschler, F.; Thomas, T. H.; Dutton, S. E.; Goedel, K. C.; Hanusch, F. C.; Lai, M. L.; Steiner, U.; Bein, T.; Docampo, P. Preparation of single-phase films of $CH_3NH_3Pb\ (I_{1-x}\ Br_x)_3$ with sharp optical band edges. *The Journal of Physical Chemistry Letters* **2014,** *5* (15), 2501-2505.

(161) Song, J.; Li, J.; Li, X.; Xu, L.; Dong, Y.; Zeng, H. Quantum dot light‐emitting diodes based on inorganic perovskite cesium lead halides ($CsPbX_3$). *Advanced Materials* **2015,** *27* (44), 7162-7167.

(162) Lu, J.; Sheng, X.; Tong, G.; Yu, Z.; Sun, X.; Yu, L.; Xu, X.; Wang, J.; Xu, J.; Shi, Y. Ultrafast Solar‐Blind Ultraviolet Detection by Inorganic Perovskite $CsPbX_3$ Quantum Dots Radial Junction Architecture. *Advanced Materials* **2017,** *29* (23), 1700400.

(163) Tang, B.; Dong, H.; Sun, L.; Zheng, W.; Wang, Q.; Sun, F.; Jiang, X.; Pan, A.; Zhang, L. Single-mode lasers based on cesium lead halide perovskite submicron spheres. *ACS Nano* **2017,** *11* (11), 10681-10688.

(164) Wang, Y.; Li, X.; Song, J.; Xiao, L.; Zeng, H.; Sun, H. All‐inorganic colloidal perovskite quantum dots: a new class of lasing materials with favorable characteristics. *Advanced Materials* **2015,** *27* (44), 7101-7108.

(165) Della Gaspera, E.; Peng, Y.; Hou, Q.; Spiccia, L.; Bach, U.; Jasieniak, J. J.; Cheng, Y.-B. Ultra-thin high efficiency semitransparent perovskite solar cells. *Nano Energy* **2015,** *13*, 249-257.

(166) Chen, L.-C.; Wu, J.-R.; Tseng, Z.-L.; Chen, C.-C.; Chang, S.; Huang, J.-K.; Lee, K.-L.; Cheng, H.-M. Annealing Effect on $(FAPbI_3)_{1-x}(MAPbBr_3)_x$ Perovskite Films in Inverted-Type Perovskite Solar Cells. *Materials* **2016,** *9* (9), 747.

(167) Li, W.; Zhang, W.; Van Reenen, S.; Sutton, R. J.; Fan, J.; Haghighirad, A. A.; Johnston, M. B.; Wang, L.; Snaith, H. J. Enhanced UV-light stability of planar

heterojunction perovskite solar cells with caesium bromide interface modification. *Energy & Environmental Science* **2016,** *9* (2), 490-498.

(168) Bu, T.; Li, J.; Zheng, F.; Chen, W.; Wen, X.; Ku, Z.; Peng, Y.; Zhong, J.; Cheng, Y.-B.; Huang, F. Universal passivation strategy to slot-die printed SnO_2 for hysteresis-free efficient flexible perovskite solar module. *Nature Communications* **2018,** *9* (1), 4609.

(169) Tiong, V. T.; Pham, N. D.; Wang, T.; Zhu, T.; Zhao, X.; Zhang, Y.; Shen, Q.; Bell, J.; Hu, L.; Dai, S. Octadecylamine‐Functionalized Single‐Walled Carbon Nanotubes for Facilitating the Formation of a Monolithic Perovskite Layer and Stable Solar Cells. *Advanced Functional Materials* **2018,** *28* (10), 1705545.

(170) Zhang, J.; Daniel, Q.; Zhang, T.; Wen, X.; Xu, B.; Sun, L.; Bach, U.; Cheng, Y.-B. Chemical Dopant Engineering in Hole Transport Layers for Efficient Perovskite Solar Cells: Insight into the Interfacial Recombination. *ACS Nano* **2018,** *12* (10), 10452-10462.

(171) Protesescu, L.; Yakunin, S.; Bodnarchuk, M. I.; Krieg, F.; Caputo, R.; Hendon, C. H.; Yang, R. X.; Walsh, A.; Kovalenko, M. V. Nanocrystals of cesium lead halide perovskites (CsPbX3, X= Cl, Br, and I): novel optoelectronic materials showing bright emission with wide color gamut. *Nano Letters* **2015,** *15* (6), 3692-3696.

(172) Ning, Z.; Gong, X.; Comin, R.; Walters, G.; Fan, F.; Voznyy, O.; Yassitepe, E.; Buin, A.; Hoogland, S.; Sargent, E. H. Quantum-dot-in-perovskite solids. *Nature* **2015,** *523* (7560), 324.

(173) Zhang, D.; Eaton, S. W.; Yu, Y.; Dou, L.; Yang, P. Solution-phase synthesis of cesium lead halide perovskite nanowires. *Journal of the American Chemical Society* **2015,** *137* (29), 9230-9233.

(174) Akkerman, Q. A.; Motti, S. G.; Srimath Kandada, A. R.; Mosconi, E.; D'Innocenzo, V.; Bertoni, G.; Marras, S.; Kamino, B. A.; Miranda, L.; De Angelis, F. Solution synthesis approach to colloidal cesium lead halide perovskite nanoplatelets with monolayer-level thickness control. *Journal of the American Chemical Society* **2016,** *138* (3), 1010-1016.

(175) Chen, B.; Peng, J.; Shen, H.; Duong, T.; Walter, D.; Johnston, S.; Al‐Jassim, M. M.; Weber, K. J.; White, T. P.; Catchpole, K. R.; Macdonald, D.; Nguyen, H. T. Imaging Spatial Variations of Optical Bandgaps in Perovskite Solar Cells. *Advanced Energy Materials* **2018**, 1802790.

(176) Chen, W.; Mao, W.; Bach, U.; Jia, B.; Wen, X. Tracking Dynamic Phase Segregation in Mixed‐Halide Perovskite Single Crystals under Two‐Photon Scanning Laser Illumination. *Small Methods* **2019**, 1900273.

(177) Zhang, F.; Zhong, H.; Chen, C.; Wu, X.-g.; Hu, X.; Huang, H.; Han, J.; Zou, B.; Dong, Y. Brightly luminescent and color-tunable colloidal $CH_3NH_3PbX_3$ (X= Br, I, Cl) quantum dots: potential alternatives for display technology. *ACS Nano* **2015,** *9* (4), 4533-4542.

(178) Xing, G.; Mathews, N.; Lim, S. S.; Yantara, N.; Liu, X.; Sabba, D.; Grätzel, M.; Mhaisalkar, S.; Sum, T. C. Low-temperature solution-processed wavelength-tunable perovskites for lasing. *Nature Materials* **2014,** *13* (5), 476-480.

(179) McMeekin, D. P.; Sadoughi, G.; Rehman, W.; Eperon, G. E.; Saliba, M.; Hörantner, M. T.; Haghighirad, A.; Sakai, N.; Korte, L.; Rech, B. A mixed-cation lead mixed-halide perovskite absorber for tandem solar cells. *Science* **2016,** *351* (6269), 151-155.

(180) Beal, R. E.; Slotcavage, D. J.; Leijtens, T.; Bowring, A. R.; Belisle, R. A.; Nguyen, W. H.; Burkhard, G. F.; Hoke, E. T.; McGehee, M. D. Cesium lead halide perovskites

with improved stability for tandem solar cells. *The Journal of Physical Chemistry Letters* **2016,** *7* (5), 746-751.

(181) Rosales, B. A.; Hanrahan, M. P.; Boote, B. W.; Rossini, A. J.; Smith, E. A.; Vela, J. Lead halide perovskites: Challenges and opportunities in advanced synthesis and spectroscopy. *ACS Energy Letters* **2017,** *2* (4), 906-914.

(182) Zhou, Y.; Wang, F.; Cao, Y.; Wang, J. P.; Fang, H. H.; Loi, M. A.; Zhao, N.; Wong, C. P. Benzylamine - treated wide - bandgap perovskite with high thermal - photostability and photovoltaic performance. *Advanced Energy Materials* **2017,** *7* (22), 1701048.

(183) Green, M. A.; Hishikawa, Y.; Dunlop, E. D.; Levi, D. H.; Hohl-Ebinger, J.; Ho-Baillie, A. W. Solar cell efficiency tables (version 52). *Progress in Photovoltaics: Research and Applications* **2018,** *26* (7), 427-436.

(184) Cheng, Z.; Wang, Z.; Xing, R.; Han, Y.; Lin, J. Patterning and photoluminescent properties of perovskite-type organic/inorganic hybrid luminescent films by soft lithography. *Chemical Physics Letters* **2003,** *376* (3-4), 481-486.

(185) Zhang, Y.; Liu, J.; Wang, Z.; Xue, Y.; Ou, Q.; Polavarapu, L.; Zheng, J.; Qi, X.; Bao, Q. Synthesis, properties, and optical applications of low-dimensional perovskites. *Chemical Communications* **2016,** *52* (94), 13637-13655.

(186) Niu, L.; Liu, X.; Cong, C.; Wu, C.; Wu, D.; Chang, T. R.; Wang, H.; Zeng, Q.; Zhou, J.; Wang, X. Controlled Synthesis of Organic/Inorganic van der Waals Solid for Tunable Light–Matter Interactions. *Advanced Materials* **2015,** *27* (47), 7800-7808.

(187) Feng, J.; Yan, X.; Zhang, Y.; Wang, X.; Wu, Y.; Su, B.; Fu, H.; Jiang, L. "Liquid Knife" to Fabricate Patterning Single-Crystalline Perovskite Microplates toward High-Performance Laser Arrays. *Advanced Materials* **2016,** *28* (19), 3732-3741.

(188) Chou, S. S.; Swartzentruber, B. S.; Janish, M. T.; Meyer, K. C.; Biedermann, L. B.; Okur, S.; Burckel, D. B.; Carter, C. B.; Kaehr, B. Laser direct write synthesis of lead halide perovskites. *The Journal of Physical Chemistry Letters* **2016,** *7* (19), 3736-3741.

(189) Saidaminov, M. I.; Abdelhady, A. L.; Murali, B.; Alarousu, E.; Burlakov, V. M.; Peng, W.; Dursun, I.; Wang, L.; He, Y.; Maculan, G. High-quality bulk hybrid perovskite single crystals within minutes by inverse temperature crystallization. *Nature Communications* **2015,** *6*, 7586.

(190) Jia, B.; Li, J.; Gu, M. Two-photon polymerization for three-dimensional photonic devices in polymers and nanocomposites. *Australian Journal of Chemistry* **2007,** *60* (7), 484-495.

(191) Levchuk, I.; Osvet, A.; Tang, X.; Brandl, M.; Perea, J. D.; Hoegl, F.; Matt, G. J.; Hock, R.; Batentschuk, M.; Brabec, C. J. Brightly luminescent and color-tunable formamidinium lead halide perovskite $FAPbX_3$ (X= Cl, Br, I) colloidal nanocrystals. *Nano Letters* **2017,** *17* (5), 2765-2770.